Particle Production and Correlations in Ultra-Relativistic Nucleus-Nucleus Collisions

THESIS SUBMITTED

TO

THE UNIVERSITY OF JAMMU

FOR THE AWARD OF THE

DEGREE OF DOCTOR OF PHILOSOPHY

IN

PHYSICS

Submitted by:

Sunil Manohar Dogra

Supervised by:

Prof. Anju Bhasin

&

Dr. Subhasis Chattopadhyay

Department of Physics & Electronics
University of Jammu
Jammu Tawi
J&K – 180006

(September 2008)

Dedicated

To

My Parents

CERTIFICATE

I, hereby declare that the work presented in the thesis entitled *"Particle Production and Correlations in Ultra-Relativistic Nucleus-Nucleus Collisions"* is carried out by me and has been done under the supervision of **Prof. Anju Bhasin** and **Dr. Subhasis Chattopadhyay**. No part of this work has been submitted in part or full for the award of a degree in any other University.

Sunil Manohar Dogra

Certified that:

1. the thesis embodies the work of **Mr. Sunil Manohar Dogra** and worthy of consideration for the award of Ph.D degree;
2. the candidate worked under us for the required period under rule;
3. the candidate has put in required attendance in the department during the period of research; and
4. the conduct of the candidate remained satisfactory during the period.

Dr. Subhasis Chattopadhyay
(Supervisor)

Prof. Anju Bhasin
(Supervisor)

Countersigned

Head of the Department

ACKNOWLEDGEMENTS

The writing of this thesis has been one of the most significant academic challenges I have ever had to face. Without the support, patience and guidance of the following people, this study would not have been completed. It is to them that I owe my deepest gratitude.

First and foremost, I want to thank **Prof. Anju Bhasin** and **Dr. Subhasis Chattopadhyay**, my doctoral advisors for inspiring and encouraging me to pursue a career in high energy physics. I shall never forgot their willingness to take a chance with me. Their words of encouragement, guidance and careful reading of all of my writing will never be forgotten. They are the rare advisors that students dream that they will find. Without their support, I could not have done what I was able to do. Their wisdom and knowledge inspired and motivated me, and have made me a better researcher.

My regardful thanks are due to Prof. L.K. Magotra, ALICE/STAR project leader and Prof. V. K. Gupta for their good-wishes. I express my sincere thanks to Er. Anik Gupta and Dr. Sanjeev Singh Sambyal for their valuable help, care and suggestions. I would like to thank Prof. S. K. Badyal, Dr. P. V. K. S. Baba, Dr. R. Gupta, Er. Sanjay Mahajan and Dr. S. K. Nayak.

My thanks are also due to Prof. Naresh Padha, Head, Department of Physics for providing all the necessary facilities during my Ph.D period. I am also thankful to the former HOD, Prof. S. K. Khosa for providing facilities during the early stages my research and am equally thankful to the faculty of Department of Physics. Thanks are due to the technical staff of our high energy physics group for their loving company and affection. I extend my thanks to all the members of teaching and non-teaching staff of the Physics Department, University of Jammu for their kind co-operation.

I would like to express my thanks to Dr. Y. P. Viyogi (Director IOP, Bhubaneswar) for his support. My sincere thanks are due to Dr. T. K. Nayak for his support and

encouragement throughout of my research period. I would like to thank Dr. B. Mohanty for his help and encouragement from whom I have learned many valuable things. I would like to thank Mr. G. S. N Murthy , Mr. R. N. Singaraju, Mr. Sushant Pal, Dr. Zubyar Ahmed and Dr. Premomoy Ghosh. I would also like to thank Prof. D. P. Mahapatra from IOPB and Prof. M. M. Aggarwal from Panjab University, Chandigarh.

I thank all memebrs of STAR collaboration for their dedicated efforts for successful running of the experiment. I would like to thank the spokeperson Prof. Nu Xu and Dr. Timothy J. Hallman for their support and encouragement.

I would also like to thank my seniors in collaboration Dr. Anand Dubey, Dr. Indu Manhas, Dr. Dipak Mishra, Dr. Supriya Das, Dr. Raghunath Sahoo, Dr. Debasish Das for fruitful discussion and spending memorable time with me.

It takes a minute to find a special person, an hour to appreciate them, a day to love them and a lifetime to forget them. A special thank to "di". She has supported me, cheered me on, cheered me up, offered invaluable advice, acted as a mentor and even as a surrogate Grandpa.

My profound appreciation and sincere thanks are due to my colleagues, friends of high energy physics group Mr. Satish Sharma, Mr. Ranbir Singh, Mr. Surjeet Singh, Mr. Hansraj Sharma, Ms. Anju Kumari, Mr. Munish Gupta, Mr. Munish Sharma, Ms. Anita Mahajan, Ms. Seema Gupta, Ms. Manmeet Kour, Mr. Vivek Chalotra, Mr. Chaman Atri and Mr. Neeraj Gupta. They made my experience more enjoyable and their support, understanding and laughter kept me going long enough to complete it.

It has been a nice experience working in collaboration with Ms. Monika Sharma, Mr. Pawan K. Neterkanti, Mr. Ajay Thakur, Mr. Sidhrath, Mr. Mriganka, Mr. Vikas Singhal and Mr. Victor Roy.

If you are lucky, you encouter a really speacial person in your life, someone with the heart bigger than their ability toexpress it. My profound appreciations and sincere

thanks are also due to my friends Ms. Neelam, Mr. Bhuvan Gupta, Mr. Arun Dev Singh Slathia, Mr. Inderjeet Singh and Mr. Amit Mahajan.

Finally, the acknowledgments would not be complete without a heart felt thanks to my parents (my loving Mom and Dad), sister (Shabo), brothers (Banto and Kali) and grandmother (Bibiji) for their continuous support and encouragement throughout my Ph.D period, without which I would have never been able to complete my thesis successfully. Their quiet patience and unwavering love were undeniably the bedrock upon which the past years of my life have been built. When there were difficult times during my Ph.D study, they were always the first one whom I turn to and their heartwarming words kept me going on. I feel to be the luckiest person to have such wonderful parents.

Sunil Manohar Dogra

Synopsis

Title of Thesis : **Particle Production and Correlations in Ultra-Relativistic Nucleus-Nucleus Collisions**

The principal purpose of the studies on ultra-relativistic heavy ion physics is to understand the strong interaction, one of the four fundamental forces of nature. Quantum Chromodynamics (QCD) describes the strong interaction between the quarks and gluons that dictates the structure of hadrons and nuclei. Above suitable temperature (or density), a phase transition should occur to a state where the fundamental particles, quarks and gluons, can move freely. This deconfined phase is known as a **Quark-Gluon Plasma**(QGP).

Several of the primary features of our universe are not trivially derived from the standard model of particles. Instead they result from the complex structure of vacuum. The vacuum as described by QCD consists of gluonic and $q\bar{q}$ condensates which couple to hadrons in such a way so as to produce masses near one GeV even though current quark masses are only few MeV. The structure is also responsible for confinement of chromo-electromagnetic fields which restrict all matter into coherent color singlets at a scale grater than 10^{-15} meters. When temperatures exceed value near 170 MeV, the symmetries of underlying Standard Model are expected to be restored as vacuum condensates melt. At these temperatures matter should behave as plasma of nearly massless quarks and gluons (QGP), a state existing in first few microseconds of the "Big Bang".

Experiments at the **AGS**(Brookhaven) and **SPS** (CERN) have shown that such a state does occur. The first experimental indication to quark hadron phase transition at relativistic heavy ion collision experiments has come at CERN. These results provide extremely relevant information about the (predicted) formation of a deconfined state of matter in high-energy heavy ion collisions. However, considerable homework remains

to be done in view of converting "compelling evidence" into "conclusive evidence" that quark matter phase has indeed been formed. Thus the main emphasis of experiments at **RHIC**-BNL and **LHC**-CERN in future will necessarily shift to an accurate determination of properties of the quark matter. The efforts at BNL for RHIC (Relativistic Heavy Hon Collider) where Au beams at $\sqrt{s_{NN}}$ = 200 GeV are collided and also to the building of CERN Large Hadron Collider (LHC) where Pb beams will be collided at $\sqrt{s_{NN}}$ = 5.5 TeV are put in the same direction.By colliding heavy ions at extreme energies, mesoscopic regions of sufficient energy are created with conditions favorable of creating this novel state of matter. With the unique ability to collide beams of ions from protons to Au to Pb and with the large centre of mass energies one can address a number of these fundamental questions. In this region the systems formed are well above the QGP phase boundary and in the central rapidity range, are essentially baryon free i.e. similar to that of the early Universe.

There are four major heavy ion experiments at RHIC involving 1000 scientists and 80 institutions. STAR (Solenoidal Tracker at RHIC) and PHENIX (Pioneering High Energy Nuclear Interaction Experiment) are two large experiments that measure hadrons in a large phase space. PHOBOS and BRAHMS (Broad Range Hadron Magnetic Spectrometer) are smaller experiments, but have unique capabilities. RHIC data with significant precession have provided an opportunity for higher resolution measurements of the detailed properties of the new forms of matter. The main motivation behind the present work is QCD prediction of phase transition in hadronic matter at sufficiently high energy densities i.e. the work is primarily directed to study the existence and the nature of the transition from hadronic phase to QGP phase, through various predicted signatures for the phase transition in heavy ion collisions.

Main emphasis of the present work is to study the production of photons in high energy heavy ion collisions i.e the work is primarily directed to study the nature of phase

transition through photon production which is one of the various predicted signatures of the phase transition from Hadronic phase to QGP phase in heavy Ion collisions. These signatures are expected to provide information about the formation of a deconfined state of matter in high-energy heavy ion collisions. Central ultra-relativistic collisions at RHIC are expected to produce about 10^4 particles per collision, and thus present one with the remarkable opportunity to analyze, on an event-by-event basis, fluctuations in physical observables such particle multiplicities, transverse momenta, correlations and ratios. From these global observables (e.g multiplicity of photons, charged particles and transverse energy), one understands the dynamics of particle production and evolution of the system. Photons are produced at all stages of the system created in heavy ion collisions. They have large mean free paths and are therefore a carriers of information about the history of the collision. The multiplicity measurement of photons on an event by event basis can be used to extract information on various aspects of the reaction mechanism in the heavy ion collisions.

Present work is based on STAR experiment preformed at RHIC, BNL Brookhaven where beams of Au-ions are collided at the $\sqrt{s_{_{NN}}}$ = 200 GeV. The STAR detector has a capability to measure, simultaneously, a very wide number of global variables and specific QGP signals, many on an event by event basis. Several important measurements e.g Jet quenching, production of large elliptic flow are made at RHIC. Present work lays emphasis on another very important aspect of the collisions through studies of correlation and fluctuations. The STAR detector at RHIC explored a new energy region where the centre of mass energy per nucleon will be 10 times higher than that at CERN SPS. A brief summary of present work is as follows:

(a) **Multiplicity and Pseudo Rapidity Distributions of Photons :**

In the present thesis I have studied the centrality-dependent measurement of photon multiplicity using the Photon Multiplicity Detector (PMD) and pseudorapidity distri-

butions. The photons are measured in the pseudorapidity region $-3.7 \leq \eta \leq -2.3$. The scaling of particle production with the number of participating nucleons and the number of binary collisions is studied. The photon production in the measured pseudorapidity range has been found to be independent of energy and system size showing a limiting fragmentation behavior.

(b) **Fluctuations and Correlations :**

The study of correlations and fluctuations in the relativistic nuclear collisions addresses fundamental aspects of the quantum chromodynamics (QCD) and therefore the properties of strongly-interacting matter at extreme density and temperature. Fluctuations have contributions of different nature. Besides the statistical fluctuations due to a finite number of particles in case of heavy ion collisions, there are also fluctuations due to finite range of the impact parameter used for particular centrality i.e volume fluctuation. Both these fluctuations are trivial and add to the dynamical fluctuations which carry the real information about the properties of the system. Event-by-Event fluctuations in multiplicities of neutral pion relative to charged pions would be a characteristic signal of chiral symmetry restoration in heavy-ion collisions. If, during expansion and cooling, domains of chiral condensates gets "*disoriented*" (DCC),it might result in the anomalous fluctuations in $\pi^0/\pi^{\pm}$ ratios.

The chapters of the thesis are planned as:

Chapter 1 presents the brief history and background of Heavy Ion Collisions. A general overview of the signatures and their results from the SPS experiments are also discussed. The present problem and its importance is also discussed in this chapter

Chapter II briefly introduces various detectors at RHIC employed to study the heavy Ion collisions. The main emphasis in this chapter is laid on the discussion on the various sub detectors in the STAR experiment.

Chapter III describes in details the Photon Multiplicity Detector(PMD). Besides

it also includes the analysis method for the particle multiplicity distributions with the emphasis on the data clean up procedures and the gain calibration methods and the reconstruction of the photons.

Chapter IV gives the multiplicity and pseudorapidity distributions of the photons . It includes the scaling of particle production and the study of centrality, energy and system size dependence

In **Chapter V**, results on dynamical fluctuation measuremnts are discussed. The dynamical fluctuations measured between the multiplicities of the photons and the charged particles at forward pseudorapidities for Au+Au and Cu+Cu collisions at $\sqrt{s_{NN}}$ =200 GeV are presented. HIJING calculations indicates that about 93% of photons are inclusive π^0 decays. Correlation between photons and charged particle multiplicities provide signal of the formation of Disoriented Chiral Condensate (DCC). Photons and charged particles are measured with the photon multiplicity detector and the forward time projection chamber respectively at STAR experiment. Two different quantities are used to study the fluctuations, one ($\nu_{dynamics}$) measures the deviation from Poissonian behavior of the correlated particle production and the other measures the width of the distribution of N_γ/N_{charge}. Finite fluctuations with little p_T dependence for different systems have been observed suggesting no significant presence of DCC within given sensitivity.

Chapter VI discusses methods of studying fluctuations in heavy ion collsions experiments. One of the challenge is to eliminate volume fluctuations due to finite centrality bin. A method is suggested in order to eliminate volume fluctuations.

Chapter VII Conclusion and Disscussion. We discuss the implication of these results in the field of high energy heavy ion collision experiments.

Contents

List of Figures

List of Tables

Chapter 1

Introduction

1.1 A new state of matter: the Quark-Gluon Plasma (QGP)

According to the Quantun Chromodynamics (QCD) [1, 2], a theory of strong interactions, at extreme temperature and/or pressure, the nuclei are expected to break into a new form of matter, the Quark Gluon Plasma(QGP) [3, 4, 5, 6]. Like its name suggests, QGP is a "soup", or plasma, of deconfined quarks and gluons. This state of matter is believed to have existed approximately 10 microseconds after the Big Bang that created our universe. Recreating this primordial state of mater under laboratory conditions and studying its properties should help to explain the origins of protons, neutron and other elementary particles and to learn how they can combine to create the diverse form of matter which we see today. The only known way to produce this new state of matter is to smash two heavy nuclei into each other at very high energies.

The study of relativistic heavy-ion collisions thus provides a unique opportunity to search for the predicted state of matter known as −−the Quark Gluon Plasma (QGP), an extremly short-lived state of matter with lifetime some 10^{-23} sec. Physicists have

been trying to determine the existence of QGP by looking at the particles that shower out from the collisions. A number of experimental signatures of the transition to the QGP [7, 8] phase have been proposed. They are being studied in several experiments at Alternating Gradient Synchrotron (AGS) [9], Relativistic Heavy Ion Collider (RHIC) at the Brookhaven National Laboratory (BNL) [10] and at Super Proton Synchrotron (SPS) at CERN [11].

Over the past 15 years, the heavy ion programmes with fixed target experiments at AGS (BNL) and SPS (CERN) accelerators and more recently with colliding beam experiments at Relativistic Heavy Ion collider (RHIC) in BNL have allowed to establish experimental evidence of the phase trasistion. While the experiments at SPS have shown that there is a limit to confined matter, the task of the RHIC program is to address the next question and investigate the properties of deconfined quark-gluon matter. The collected data from the experiments gives compelling evidence that a new state of mater has been created [12, 13].

1.2 Phenomenology of Hot and Dense Matter

The QCD matter at finite temperature, similar to other bulk materials, is expected to have a complex phase structure. The deconfined plasma is expected to exhibit unique features due to the non-Abelian nature of the strong interaction, while also showing features of conventional plasmas such as screening and collective excitations. The collision of heavy nuclei at ultra- relativistic energies presents the opportunity of studying this phase structure in controlled laboratory experiments. Experimental observables available at collider energies give insight to the degree of equilibration of the medium, to the dynamical processes that lead to dense QCD matter, and to the initial state from which this matter emerges.

1.2.1 The QCD Phase Diagram

QCD matter refers to a phase of matter whose degrees of freedom include quarks and gluons. This phase occur at extremely high temperatures and densities where hadronic matter is supposed to undergo a phase transition to a new state where quarks and gluons are no longer 'hidden' (or, more technically, confined) into nucleons. By analogy with classical plasma this phase is called Quark Gluon Plasma (QGP) - however, at a variance with classical plasma, the QCD plasma is an extremely complicated phase with possible remaining interactions among the constituents, whose properties are under active scrutiny. The scrutiny of this new state of matter- equation of state (EoS), order of the phase transition, transport properties, etc - promises to shed light on the basic aspects of strong interaction such as nature of confinement, the mechanism of mass generation (Chiral symmetry breaking, structure of QCD vacuum) and hadronization which still evades through theoretical description due to their highly non-perturbative nature.

Under such extreme conditions, the familiar structure of matter, with quarks arranged into nucleons and nucleons bound into nuclei and surrounded by electrons, is completely disrupted, and the quarks roam freely. At ordinary temperatures or densities the nuclear force confines the quarks into composite particles (hadrons) of size around 1 fm (corresponding to the QCD energy scale $\lambda_{QCD} \sim 200$ MeV) and its effects are not noticeable at longer distances. However, when the temperature reaches the QCD energy scale (T of order 10^{12} ^oK) or the density rises to the point where the average inter-quark separation is less than 1 fm (quark chemical potential $\mu \approx 400$ MeV), the hadrons are melted into their constituent quarks, and the strong interaction becomes the dominant feature of the physics. Such phases constitute quark matter or QCD matter.

The phase diagram of quark matter is not well known, either experimentally or theoretically. A commonly conjectured form of the phase diagram is shown in the Figure

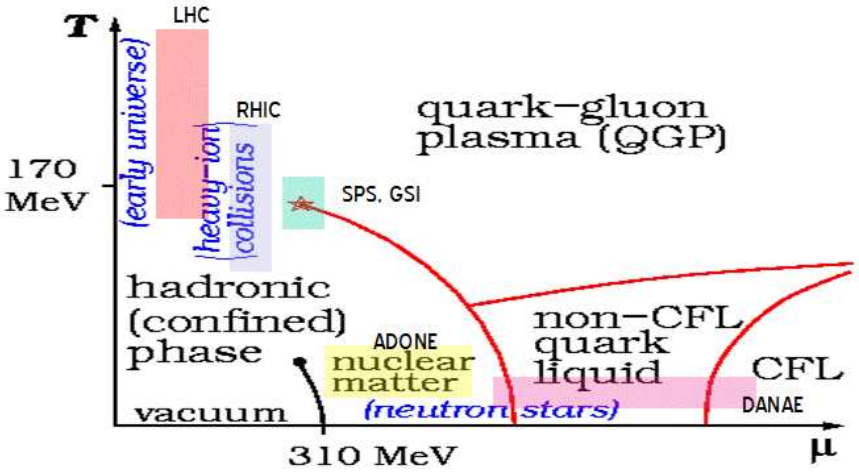

Figure 1.1: *A schematic representation of the phase diagram of strongly interacting matter in the plane of temperature (T) and baryon chemical potential (μ_B) showing hadronic gas, quark-gluon plasma regions. The solid curve through the data points represents the chemical freeze-out of hadronic matter.*

1.1. It is applicable to matter in a compact star, where the only relevant thermodynamic quantities are the quark chemical potential μ and temperature T. If we increase the quark density (i.e. increase μ) keeping the temperature low, we move into a phase of compressed nuclear matter. Eventually, at an unknown critical value of μ, there is a transition to quark matter. At ultra-high densities we expect to find the color-flavor-locked (CFL) phase of color-superconducting quark matter. At intermediate densities we expect some other phases (labeled "non-CFL quark liquid" in the Figure 1.1) whose nature is presently unknown.

At the bottom left corner of the phase diagram, in the vacuum, we have $\mu = T = 0$. If we heat up the system without introducing any preference for quarks over anti-quarks, this corresponds to moving vertically upwards along the T axis. At first, quarks are still confined and we create a gas of hadrons (pions, mostly). Then around T=170 MeV there is a crossover to the quark gluon plasma: thermal fluctuations break up the pions,

and we find a gas of quarks, anti-quarks, and gluons, as well as lighter particles such as photons, electrons, positrons, etc. Following this path corresponds to the state of the universe shortly after the big bang (where there was a very tiny preference for quarks over anti-quarks).

The line that rises up along the nuclear/quark matter transition and then bends back towards the T axis, with its end marked by a star, is the conjectured boundary between confined and unconfined phases. Until recently, it was also believed to be a boundary between phases where chiral symmetry is broken (low temperature and density) and phases where it is unbroken (high temperature and density). It is now known that the color-flavor-locked (CFL) phase exhibits chiral symmetry breaking, and the other quark matter phases may also break chiral symmetry, so it is not clear whether this is really a chiral transition line. The line ends at the "critical point", marked by a star in this Figure 1.1, which is a special temperature and density at which striking physical phenomena (analogous to critical opalescence) are expected

This "$deconfinement$" phase transition from hadronic matter to quark-gluon matter takes place at a temperature of about 170 MeV (at net baryon density zero) which is 130 thousand times hotter than the interior of the sun. Such conditions did exist in the early universe, a few microseconds after the big bang and can be created in heavy ion collisions at ultra-relativistic energies as provided by the accelerators SPS (CERN), RHIC (Brookhaven) and the future LHC (CERN). In highly compressed cold nuclear matter - as it may exist in the interior of neutron stars - the baryons also lose their identity and dissolve into quarks and gluons. The critical density at which this transition occurs, however, is not known. The same is true for the entire high-density area of the phase diagram. At very high densities and low temperatures, beyond the deconfinement transition, a new phase is expected: the quarks are correlated and form a color superconductor. At the "critical point" the deconfinement/chiral phase transition

is predicted to change its character. The new GSI facility, FAIR(Facility for Anti-proton and Ion Research) permits the exploration of the "terra incognita" of the QCD phase diagram in the region of high baryon densities. This research program is complementary to the investigations performed at the RHIC facility at Brookhaven, USA, and at the SPS and in the future, the LHC facility (ALICE Experiment) at CERN.

1.2.2 Lattice QCD Results

The existence of a QGP can be theoretically inferred through QCD calculations on a lattice [14]. Lattice QCD is a method of calculating equilibrium properties of strongly interacting systems directly from QCD Lagrangian by numerical evaluation of the path integral. These calculations predict a phase transition from the confined hadronic matter (such as protons and neutrons) to a deconfined state in which hadrons are dissolved into quarks and gluons (or partons) at a temperature $T_C \sim 170$MeV which corresponds to an energy density 0.7 GeV/fm^3, nearly an order of magnitude larger than cold nuclear matter. Figure 1.2 shows the results of recent calculation of ϵ/T^4 for 2- and 3- flavors of QCD with light quarks and for 2 light plus 1 heavior (Strange) quark(indicated by stars) [15]. The latter case is likely to be the closest to the physically realized quark mass spectrum. In Figure 1.2 the black arrows indicate the temperatures reached in the initial stages of heavy-ion reactions at SPS, RHIC and at LHC constructed at the CERN laboratory). The colored arrow indicates the Stefan-Boltzmann limit for an ideal gas. The transition can be understood in terms of the number of degrees of freedom n_{dof} [16]. The number of flavors and masses of the quarks constitute the main uncertainties in determination of critical temperature (T_C) and critical energy density. Above T_C , the gluon (8(color) 2(spin) for a total of 16) and quark (2-3(light flavors) 2(quark-anti-quark) 3(colors) 2(spin) for a total of 24-36) degrees of freedom are activated. In the quark-gluon plasma, there are then about 40-50 internal degrees of freedom in the

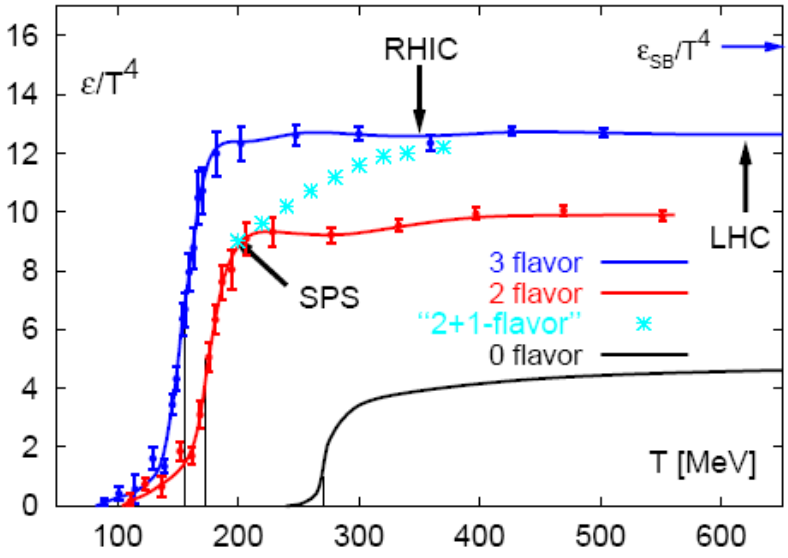

Figure 1.2: *The energy density in QCD with 2 and 3 light quarks and also the calculation for the case where the strange quark mass is fixed to* T_C.

temperature range (1 - 3) T_C, while at low temperature, the pion gas has 3 $(+,-,0)$. Since the energy density is roughly proportional to the number of degrees of freedom $\epsilon \approx n_{dof}\frac{\pi^2}{30}T^4$, one understands this rapid change in the energy density in a narrow temperature window as a change in the number of degrees of freedom between confined and deconfined matter. The critical temperature is estimated to be $T_C = 175 \pm 15$ MeV and critical density $\epsilon_C \approx (\epsilon + 2)T_C^4 \sim (0.3 - 1.3)GeV/fm^3$. Most of the uncertainty on ϵ_C arises from 10% uncertainity on T_C. Nucleus-Nucleus collisions are a process to heat and/or compress atomic nuclei. The variation of the collision energy and the system size allows us to control the degree to which this happens.

1.3 Exploring Fundamental Properties of QCD

By exploring the phase diagram, one probes the strong interaction and its underlying theory, Quantum Chromo Dynamics (QCD). In particular, fundamental properties of QCD such as the confinement and the broken chiral symmetry, which is related to the origin of hadron masses, can be explored in heavy-ion collisions. A quantitative understanding of these two phenomena is still lacking and hence possess a challenge for future research. The experimental approach to these problems is to search for the modifications of hadron properties in a dense and hot nuclear medium and for deconfined matter consisting of quarks and gluons by Nucleus-Nucleus Collisions.

1.3.1 Space - Time Diagram of Heavy-Ion Collisions

High-energy heavy-ion collisions can be used to produce a phase transition from the hadronic matter to the quark-gluon plasma. In relativistic collisions, nuclei are contracted in the beam directions like pancakes due to the Lorentz boost. Because of the Lorentz contraction, the nucleon-nucleon collisions in a nucleus-nucleus collisions occur at about the same time and at nearly the same spatial proximity. The space-time evolution of central collision at very high energies is shown schematically in the Figure 1.3, assuming the first phase transition, where the "space" corresponds to the extent of the longitudinal source size. The space-time evolution is summarized as different stages below:

Just after the collision, the hard scattering processes on the parton level may occur with smaller probability by perturbative QCD cross-sections. In addition, soft nucleon-nucleon collisions between the highly Lorentz contracted nuclei redistributes a fraction of the original beam energy into other degrees of freedom. This is the initial stage of collisions labeled as pre-equilibrium in Figure 1.3.

After a short time, taken to be of the order of 1 fm/c ('formation time') partons

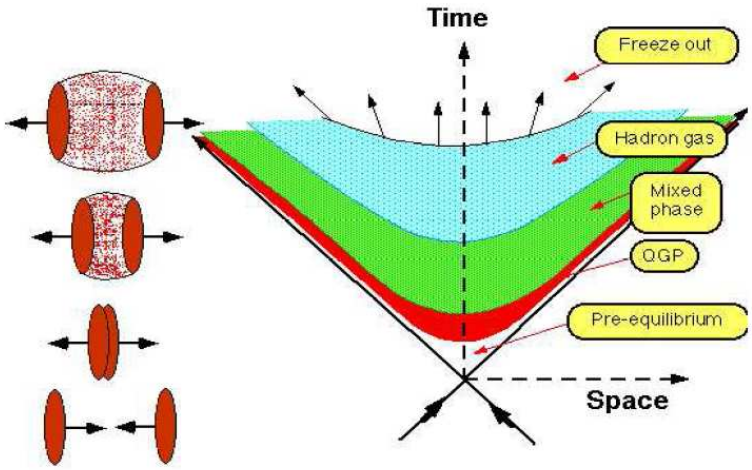

Figure 1.3: *A collision between two heavy nuclei takes place at (z,t) = (0,0) where z is the space coordinate along the beam axis and t is the time coordinate. The figure shows the evolution of the system with QGP formation.*

materialize out of the highly excited QCD field. Thermal equilibrium is approached by parton-parton or string-string interactions. Calculations of the mean free path of the quarks in QCD matter give a value of λ = 0.5 fm at energy density = 2 GeV/fm^3 [17, 18]. This indicates that the equilibrium may reach in the collisions of heavy nuclei, where the transverse radii and the initial dimensions are clearly larger than λ.

However, the system expands rapidly, mainly along the longitudinal dimensions, and therefore lowers its temperature and reaches the critical transition temperature T_C after proper time τ = 3-5 fm. The matter now spends long time in the mixed phase($\tau >$ 10 fm), in particular if the phase transition occurs via first order [19]. It has to arrange the many degrees of freedom (partons) of the QGP into smaller number available in the hadron phase, with large release of latent heat. In the last and hadronic phase($\tau >$10 fm), the still interacting systems keeps expanding possibly in an ordered motion ($''flow''$). It may expand to a very large expanding dimensions ($volumeV > 10^4 - 10^5 fm^3$) until

freeze out, when interactions cease and particles stream freely away to be detected in the experiments.

1.4 Signatures of QGP

If a Quark Gluon plasma is created in a collision of two large nuclei, it eventually has to hadronize. The detectors in our experiments can only measure the hadronic debris from this collision. A direct observation of the signals of QGP formation is not possible unlike the plasma of ordinary atomic matter due to the fundamental properties of the physical QCD vacuum. There has been a long discussion over past 25 years what the possible signatures of a phase transition from a QGP might be. Some of the signals which are sensitive to the transient QGP state are listed below.

1.4.1 Collective Flow

The existence of shock waves and the possibility that nuclear matter exhibits non-random collective motion in relativistic heavy-ion collisions was suggested more than twenty years ago in connection with hydrodynamics calculation of nuclear collisions [20]. Experimentally, the first evidence of the occurrence of side ward flow was obtained 15 years latter in the Plastic Ball experiment at the Bevalac in Berkley [21]. Collective flow of nuclear matter probes the dynamics of heavy-ion reactions and can provide information about the equation of state of nuclear-matter. At the very first stage of an ultra-relativistic nucleus-nucleus collision new particles are produced in individual nucleon-nucleon collisions. In the transverse plane, all particles from a single NN collision are initially located at the same position. The subsequent thermalization and transverse radial expansion of the system create strong position-momentum correlations and lead to characteristic rapidity, transverse momentum, and azimuthal correlations among the produced particles. The possible formation of a quark-gluon plasma could affect how the initial anisotropy in

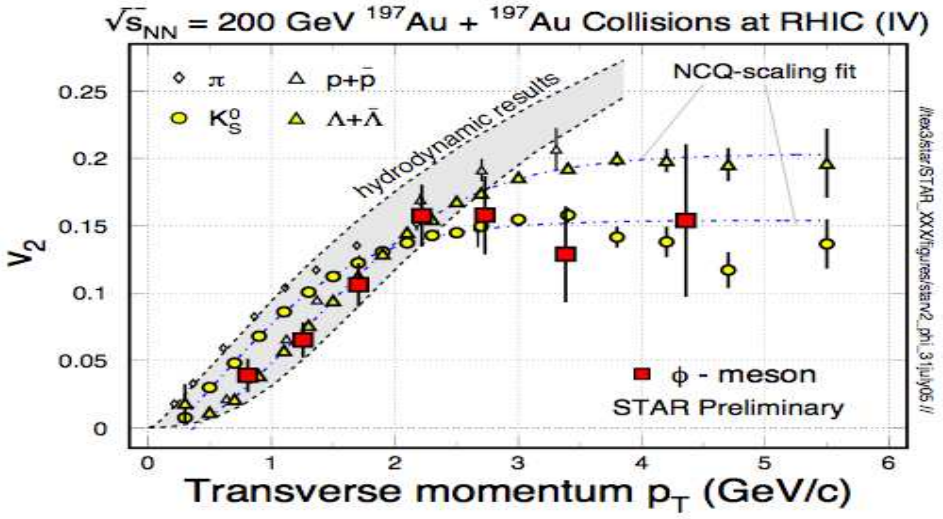

Figure 1.4: *Elliptic flow coefficient v_2 for Au + Au collisions at $\sqrt{s_{NN}}$ =200 GeV collisions for identified particle species. The elliptic flow is a measure of the anisotropic pressure-driven expansion in off-center. The dotted lines show the number of constituent quarks (NCQ) scaling fit and the band is hydrodynamics calculations.*

coordinate is transferred into momentum space in the final space. The important feature of collective flow is that it develops over the entire history of the nuclear collision. It is therefore, a hadronic observable which is sensitive to the initial conditions of the hot and dense matter produced in relativistic nuclear collisions. In the case that the nuclear matter undergoes a transition from hadron gas phase to quark-gluon plasma(QGP) phase, it is expected that the equation of state (EoS) will exhibit a corresponding softening due to the increase in the number of degrees of freedom. A QGP phase would result in decreased pressure gradients, and hence decreased collective flow. This, the detailed study of the incident energy dependence collective flow might provide the evidence of QGP formation.

Three different types of transverse flow are distinguished, radial, directed, and elliptic flow. Isotropic expansion in the transverse direction is called radial flow, which is

studied by means of inclusive transverse momentum spectra and can be measured in the central events and does not depend on the determination of the reaction plane defined by the beam axis and the line of joining two centers of colliding nuclei. Anisotropic expansion in non-central events is described by the directed and elliptic flow components. The azimuthal distribution of particle in momentum space can be expanded in the form of Fourier series:

$$E\frac{d^3N}{d^3p} = \frac{d^3N}{p_T dp_T dy d\phi'} = \frac{1}{2\pi}\frac{d^2N}{p_T dp_T dy}[v_0 + 2v_1 cos(\phi') + 2v_2 cos(2\phi') + ...] \quad (1.1)$$

It is convenient to characterize directed flow by v_1, the amplitude of the first harmonic in the Fourier decomposition of the particle azimuthal distribution which is studied by means of inclusive transverse momentum spectra. The second harmonic coefficient represents the elliptic flow. First results for v_2 measurement of charged hadron from RHIC as function of p_T for different particle species and different collision centralities are discussed in [22, 23]. Figure 1.4 shows the comparisons of the differential elliptic flow coefficient for different particle species at $\sqrt{s_{NN}}$ =200 GeV $Au + Au$ collisions at RHIC [22, 23]. The data is fitted with the NCQ scaling fit along with the hydrodynamics results.

1.4.2 Remnants of Hardonization: Strangeness Enhancement

The strangeness content in a QGP is believed to be enhanced from that of normal hadronic matter [24]. The strangeness enhancement arises from a higher temperature in the quark-gluon plasma and from its lower effective light quark masses because of the restoration of chiral symmetry. In case of QGP there is a high concentration of up and down quarks. The quarks are fermions and the creation of $u\bar{u}$ and $d\bar{d}$ pairs might be blocked due to the Pauli principle. Then the creation of $s\bar{s}$ pairs would be favored in spite of their larger mass. The enhancement might however be explained in a purely

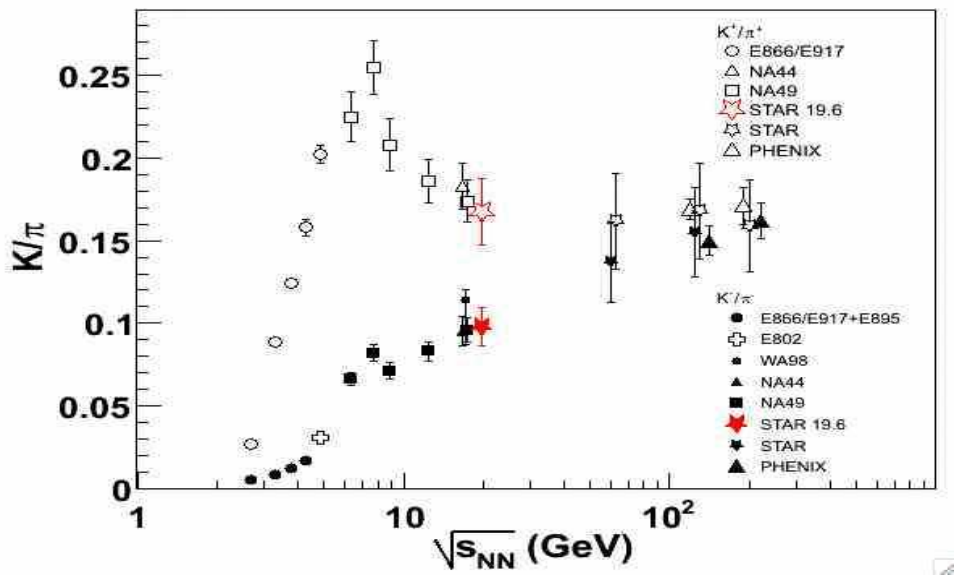

Figure 1.5: *The energy dependence of K^+/π^+ and K^-/π^- ratios at mid-rapidity. The solid and open stars are data from STAR experiment at RHIC for Au+Au collisions.*

hadronic scenario, where the abundance of strange quarks gradually grows in a chain of rescattering processes. This complication can be solved by studying particles not likely to be produced by hadronic rescattering, such as $\bar{\Lambda}$ (consisting of $\bar{u}\bar{d}\bar{s}$) and the multistrange baryons [25].

Strangeness enhancement has been studied at the AGS [26], SPS [27] and RHIC [28] energies. An enhancement of the ratio of kaon to pion production has been measured both in AGS and SPS and is often used to quantify the strangeness enhancement. STAR has currently measured the K/π ratio at mid rapidity [29]. Figure 1.5 shows the K/π ratio at mid rapidity versus collision energy in $p+p$ and $A+A$ collisions. There is a rapid increase in K^+/K^- ratio from AGS to SPS energy. Then the ratio gets saturated and practically remains constant from $\sqrt{s_{NN}}$ =10 GeV to 130 GeV. The ratios are large in A+A collisions compared to $p+p$ collisions at similar energies, which shows the strangeness enhancement known as 'horn'. Sudden jump in K^+/π^+ ratio and subsequent reduction has been explained to be due to the phase transition around $\sqrt{s_{NN}}$= 7GeV.

1.4.3 Quarkonia Suppression: J/Ψ Suppression

In 1986 Matsui and Satz predicted [30] that the suppression of heavy quarkonia-meson could provide one of the signatures of deconfinement in the QCD at high temperatures. The J/Ψ particle is a bound state of a charm and an anti-charm quark ($c\bar{c}$). At high densities, the Debye screening in quark-gluon plasma reduces the range of the attractive force between heavy quarks and anit-quarks, and above some critical density screening prevents the formation of bound state and thus the production of J/Ψ will be suppressed. The occurrence of J/Ψ suppression has been suggested as a signature for the formation of quark-gluon plasma [31]. The experimental observation by NA50 Collaboration [32] of an anomalous J/Ψ suppression in $Pb + Pb$ collisions has led to the suggestion that this anomalous suppression arises from the production of the quark-gluon plasma[33]. The production of J/Ψ is suppressed not only by the quark gluon plasma but also by the collisions of the J/Ψ(or its precursor) with nucleons and produced particles. Such nuclear absorption leads to well known smoothly increasing suppression determined by comparing J/Ψ production in proton-proton collisions with that in proton-nucleus interactions.

The J/Ψ anomalous suppression has been reported by the NA50 collaboration for the $Pb + Pb$ collisions at SPS which has given evidence for the QGP formation [34]. Figure 1.6 shows the ratio $B_{\mu\mu}\sigma(J/\psi)/\sigma(DY)$ as function of E_T for $Pb + Pb$ data taken in different years by NA50 Experiment at SPS. From the curve we see that the J/Ψ production follows the normal absorption pattern for peripheral collisions but there is deviation for central collisions suggesting that the J/Ψ suppression mechanism is other than the normal suppression.

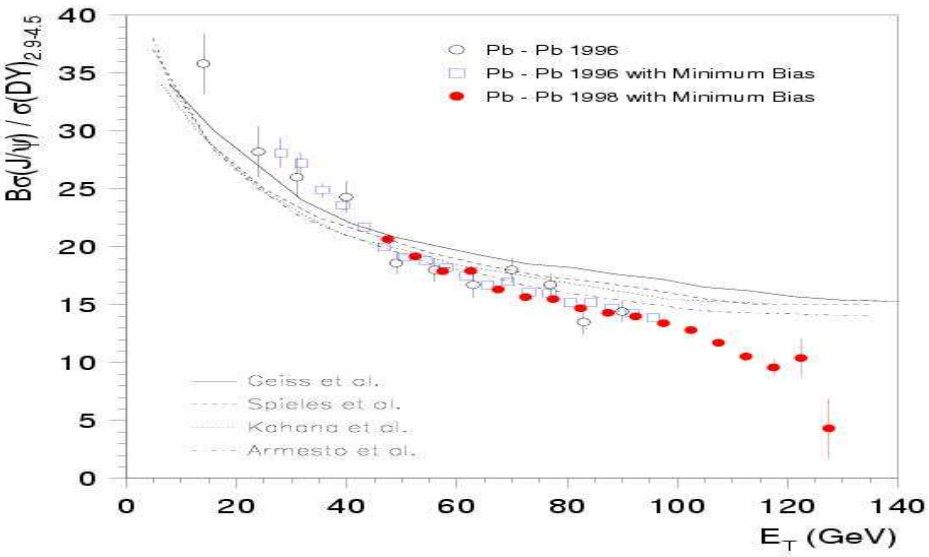

Figure 1.6: $B_{\mu\mu}\sigma(J/\psi)/\sigma(DY)$ *as function of* E_T

1.4.4 Radiation of the Plasma: Direct Photons and Thermal Dileptons

As the quark-gluon plasma expands, its energy density and temperature decrease. During the time when the matter is in the quark-gluon plasma phase, it will emit particles. Directly produced photons from quark-gluon plasma are of special interest [35], since they only interact electromagnetically, they have a mean free path much larger than the size of the reaction volume. Also, there are no final state interactions, as with hadrons, which means that the photons provide a direct probe of the initial stages of the collision. The direct photons are generally divided into prompt photons and thermal photons. The prompt photons are produced in initial hard parton scatterings, while thermal photons are produced in the possible QGP phase and in the hadron gas phase by the annihilation of quark, anti-quark pairs($q\bar{q} \rightarrow \bar{\gamma}$) and the Compton scattering of quarks and anti-quarks with gluons ($gq \rightarrow \gamma q$, $q\bar{q} \rightarrow \gamma\bar{q}$). An increase in the emission of thermal photons is therefore expected from a QGP. Low production rate and huge background

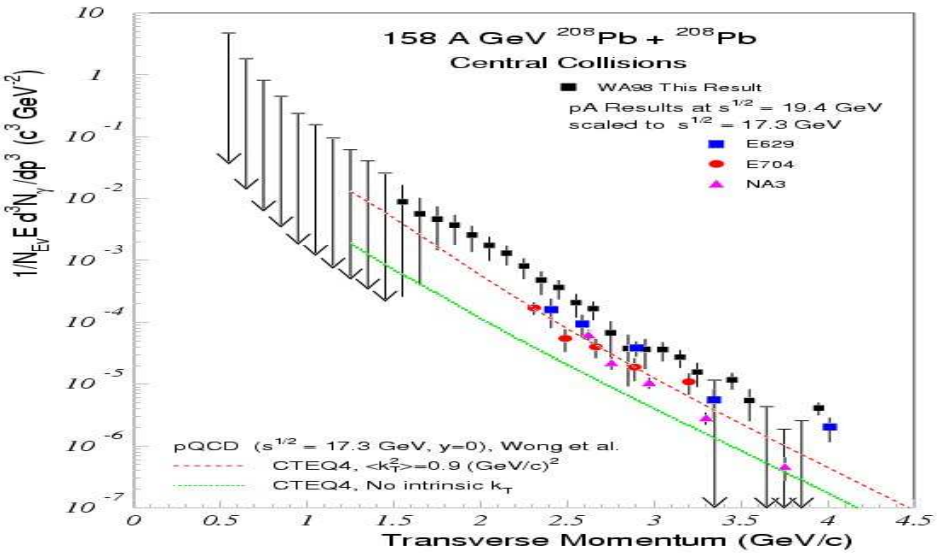

Figure 1.7: *The invariant direct photon multiplicity for central 158 AGeV* $Pb^{208} + Pb^{208}$ *collisions.*

from decays, e.g. $\pi^0 \rightarrow \gamma\gamma$ and $\eta \rightarrow \gamma\gamma$, make the isolation of the prompt and thermal components challenging. Photon measurements obtained after the subtraction of the photons from meson decays are conventionally called measurements of 'direct photons'. The WA98 experiment at CERN has reported the observation of direct photon signals in $Pb+Pb$ collisions at the SPS [36]. Figure 1.7 shows the invariant direct-photon yields as a function of transverse momentum (p_T) in $Pb+Pb$ collisions at $\sqrt{s_{NN}} = 17.2$ GeV and also the data from $p+p$ and $p+C$ collisions from other experiments and the results of a pQCD have been compared. The data suggest there is an enhancement in the photon yields in central collisions compared to pA collisions [37].

In analogy, to the formation of real photon via a quark -anti-quark annihilation, a virtual photon may be created in the same fashion which subsequently decays into a l^+l^- pair (a dilepton pair). Also bremsstrahlung of quarks, scattering off gluons can convert into dileptons. Dileptons can carry information on the thermodynamic state of the medium at the moment of production in the very same manner as the direct photons

- since the dileptons interact electromagnetically they can also leave the hot and dense reaction zone basically undistorted. However, dilepton pairs from vector meson decays are difficult to measure due to the small branching ratios and the large background contributions mainly from the pion annihilation, resonance decays, $\pi - \rho$ interactions at low dilepton masses and Drell-Yan process at high masses. Looking for dilepton as a signature for QGP has proved to be difficult experimental observables, but there is continued effort to improve the sensitivity of the measurements.

1.4.5 Jet Quenching: Energy Loss of Fast Partons in QGP

In high energy proton-proton collisions, the hard scattering of quarks and gluons early in the collision leads to the production of jets, narrow streams of fast-moving particles that allow physicists to detect and understand the scattering of partons. In nuclear collisions at RHIC, jets instead serve as a penetrating probe of the extremely dense nuclear matter formed in the collision. Comparing characteristics of jets in nuclear collisions to jets in $p + p$ collisions has uncovered special properties of dense nuclear matter at RHIC.As was first pointed out by Brojken [38] in 1983, the attenuation of QCD hard jets in ultra-relativistic nuclear collisions is sensitive to the energy loss, dE/dx, of high energy parton traversing the dense excited matter produced in these reactions. The propagation of partons through a hot and dense medium modifies their transverse momentum due to induced radiative energy loss, a phenomenon called jet quenching [39, 40] and enhanced acoplanarity and energy imbalance of the two back-to-back jets due to multiple scattering. This can be studied by measuring the p_T distribution of hadrons coming from high-p_T jets. In fact, when a hard collision producing two jets occurs near the edge of the nuclear overlap region, jet quenching might lead to complete absorption of one of the jets, while the other escapes. This signature can be found by studying the number of correlated jets at different angular separations.

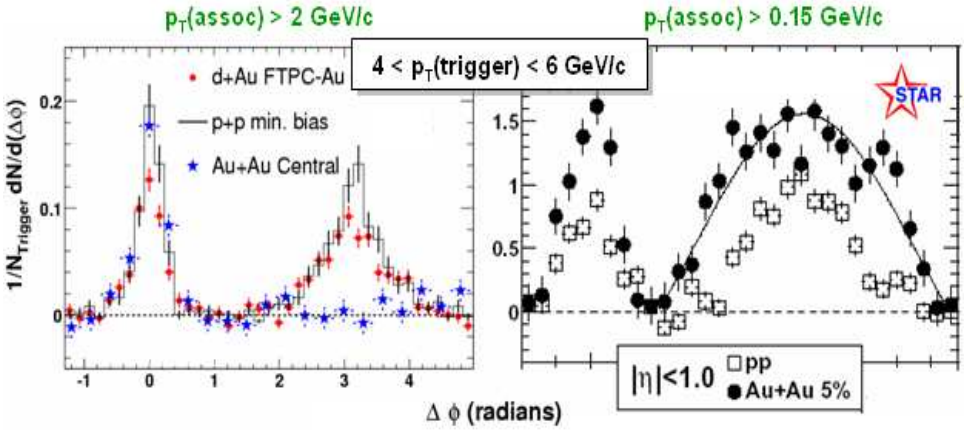

Figure 1.8: *Left : Azimuthal distribution of particle with* $p_T(associated) > 2GeV/c$ *with respect to a trigger particle with* $4 < p_T(Trigger) < 6GeV/c$*for* $p+p$ *collisions (solid line), central Au+Au and d+Au collisions and Right : Azimuthal distribution of particle with* $p_T(associated) > 0.15\ GeV/c$ *and trigger particle with* $4 < p_T(Trigger) < 6GeV/c$ *for minimum bias* $p+p$ *and Au+Au* 5% *central collisions in*

In 2003, STAR's observations that back-to-back jets measured with azimuthal correlations of high-energy particles showed a strong suppression[41] of one of the jets in head-on $Au+Au$ collisions, while the same studies in $p+p$ and $deuteron+Au$ collisions showed no such suppression [42]. The suppression of the "away-side jet" in $Au+Au$ led to the idea that hard scatterings which take place near the surface of the collisions allow one jet to escape but cause the other jet to lose significant energy in the dense matter. In contrast, a subsequent study of azimuthal correlations of lower-energy particles using the same data showed an increase of away-side particle production [43]. The two observations are shown in Figure 1.8. These observations are consistent with the notion of parton energy loss ("jet quenching") in which a quark's or gluon's energy is transferred to slower quarks and gluons, either through radiation or collisions.

1.4.6 Event-by-Event Fluctuations

Phase transitions are normally associated with large fluctuations. The QGP phase transition may yield non-statistical fluctuations in e.g. particle multiplicities, ratios and transverse momenta [44]. These fluctuations might be detectable in final state observables, some of which can be studied on an event-by-event basis. The requirement of high statistics per event for such analysis is met at RHIC and LHC energies, where a high multiplicity of particles is produced.

Event-by-event analysis of high-energy nuclear collisions searches for nonstatistical or 'dynamical' fluctuations and other significant departures from conventional hadronic physics which may result from color deconfinement and/or chiral symmetry restoration associated with a phase transition. Sufficiently high energy densities may result in increased color correlation lengths. Nonperturbative QCD effects resulting from cross coupling of nonlocal color fields (string fusion) may in turn result in significant baryon, flavor and momentum-space fluctuations. Color fluctuations in the early stages of the parton cascade may also result in significant dynamical variation in produced hadron spectra. Chiral symmetry restoration and nonequilibrium evolution of the collision system may produce phase-space domains in which the neutral-to-charged ratio of low- $p_{_T}$ pions deviates significantly from its nominal value of 1/3 [45, 46].

Fluctuations of net-charge has been studied extensively. The idea of event-by-event, net charge fluctuations as a QGP signature is not directly related to the phase transition. The main issue is the distribution of electric charge in a QGP (where the quarks carry $\pm 1/3$ or $\pm 2/3$ unit charges), compared to the distribution in ordinary hadronic matter.

The event-by-event fluctuations are new methods to understand the multiparticle production in nuclear collisions. An example that the baryon-number strangeness correlations can be utilized to address the correlations among the quark flavors, and the charge fluctuations are sensitive to the fractional charges of the quarks and thus serve

as a signature of quark gluon plasma. The measure of momentum fluctuations, on the other hand should give us an idea about the heat capacity of the system. Furthermore, if the system is created close to a second order phase transition point, the associated long range fluctuations should be observable in event-by-event observables.

1.5 Summary of RHIC Results

The quest for the search and study of QGP started in early eighties with the acceleration on Au beam at 1 GeV at Bevalac. The early success of the experiments in terms of bringing out the collective nature of the matter produced prompted the scientists at BNL and CERN to make concrete programs for the future accelerator developments for heavy ions. The next milestone came with the accelerations of Au beam at 11.7 GeV at AGS at BNL and Pb beam at 158 GeV at CERN-SPS. First hints of the formation of new state of matter has been obtained from the SPS data in terms of global observables, event-by-event fluctuations, direct photons, di-leptons and most importantly, the J/ψ suppression and strangeness enhancements [47]. For seven years now, the Relativistic Heavy Ion Collider (RHIC) at Brookhaven National Laboratory has been providing experimenters with colliding beams of heavy nuclei at ultra-relativistic energies as high as 100 GeV per nucleon. Early results from the RHIC experiments reveal new nuclear phenomena at temperatures and densities well into the range where quarks and gluons–rather than nucleons and mesons–are expected to define the relevant degrees of freedom. The first measurements of head-on collisions at RHIC energies, with nuclei as heavy as gold, have already taken us a major step toward the long-sought quark-gluon plasma.

Among the first experimental results from RHIC was the clear indication for the creation of a new state of thermalized matter at unprecedent energies densities [48] (more than 100 times larger than that of cold atomic nuclei) which appears to exhibit almost perfect fluid dynamically collective behavior, and strong indications that this

thermalized matter originated from a high energy density state of gluons with possibly universal properties. Among this evidence four fundamental new discoveries stand out:

1. Enormous collective motion of the medium is observed in spectacular fashion through the so-called elliptic flow [49] in agreement with near-zero viscosity hydrodynamics behavior(characterized as "Perfect Fluid" behavior), pointing to rapid thermalizaton and strong coupling of the matter.

2. Jet quenching, is observed via the suppression of particle production at high transverse momenta and the dramatic modification of jet correlations in central $Au+Au$ collisions, pointing towards dramatic energy loss of partons traversing matter of very high color charge density. A suppression by a factor 5, relative to the extrapolation based on independent nucleon-nucleon collisions was observed in central $Au + Au$ collisions for the momenta up to $p_{_T} \sim 10$ GeV [50]. This, together with the disappearance of jet-like correlations between particles produced in opposite azimuthal directions [51] confirms the role of strong final state interactions of the produced hard particles with surrounding matter, and favors the interpretation in terms of "Jet quenching".

3. Large, anomalous enhancement of baryon and anti-baryon production rates at intermediate transverse momentum relative to mesons, together with scaling of hadron production yields and their collective motion with the number of valence quarks, suggests that hadrons are formed by quark coalescence after the flow occurs.

4. Hints of gluon saturation: the particles produced in the $d + Au$ collisions at forward rapidity i;e in the fragmentation region of deutron [52]. There one does not expect the final state interactions to play a major role. The suppression of particle production [53] may constitute evidence for the initial state effects caused perhaps

by the phenomenon of gluon saturation [54].

In addition, RHIC experiments confirmed with higher accuracy and better systematics important features of ultra-relativistic heavy-ion collisions that were previously discovered at lower energies. These include:

1. Hadron abundance ratios [55] that are characterized by a chemical equilibrium distribution with "chemical freeze-out" temperature $T_{chem} \sim$ 160-170 MeV a value that is observed to be independent of collision system and collision centrality and agrees with the value for the quark-hadron phase transition temperature predicted by Lattice QCD.

2. A strong transverse momentum dependence of the Hanbury Brown - Twiss (HBT) radius parameters extracted from two-particle momentum correlations between pairs of identical particles, consistent with predictions from models which incorporate fast collective expansion of the collision fireball at hadronic freeze-out [56].

3. The observation in non-central collisions of an angular variation of these HBT radii with the azimuthal emission angle relative to the reaction plane that is qualitatively consistent with hydrodynamic models for the time-evolution of the spatial eccentricity of the collision fireball in such collisions.

1.6 Plan of Present Work

In the present thesis, studies are made on the production of photon and charged particles at forward rapidities in $Au + Au$ and $Cu + Cu$ collisions at $\sqrt{s_{NN}} = 200$ GeV. Multiplicity and the pseudorapidity distributions of photons are studied for $Au + Au$ and $Cu + cu$ collisions using the Photon Multiplicity Detector (PMD) at forward rapidity. Fluctuations and Correlations are studied between photon and charged particles

to understand the formation of exotic matter under extreme conditions of density and temperature. The present thesis is organized as follows:

A brief introduction of the normal nuclear matter at extreme condition of temperature and density is given in Chapter 1. In Chapter 2, a brief description of the STAR experiment and the detectors which have been used for presented analysis is given. In Chapter 3 the Photon Multiplicity Detector which we have used for the measurements of the photon multiplicities in the forward rapidity and also the correlation between the N_γ and other detector is described. The results in terms of the multiplicity and pseudo-rapidity distribution of photons, scaling properties of particle production with number of participating nucleons and the limiting behaviors of photon are presented in Chapter 4. The correlations and fluctuations between photon and charged particles using new method $\nu_{dynamics}$ is presented in Chapter 5. In Chapter 6, the volume fluctuations and a method to eliminate these fluctuations is discussed. Conclusions and the implications of the results are discussed in Chapter 7.

Bibliography

[1] D. J. Grosss and F. Wilczek, Phys. Rev. Lett. 30 1343 (1973).

[2] M. Politzer, Phys. Rev. Lett. 30 1346 (1973).

[3] R. Rapp Jour. of Phys. G 30 951 (2004).

[4] J. P. Blaizot, Nucl. Phys. A 661, 3c (1999).

[5] M. Stenhanov, K. Rajagopal, E. Shuryak, Phys. Rev. D, 60, 114028 (1999).

[6] J. P. Blaizot and E. Laneu, Phys. Rept. 359 355 (2002).

[7] J. W. Harris B. Muller, Ann. Rev. Nucl. Part. Sci. 46 71 (1996).

[8] S. A. Bass, M. Gyulassy, H.Stocker and W. Greiner, J. Phys. G, vol. 25 57 (1999).

[9] J.C. Depken and P. Lo Presti. AGS Experiments Informal Report BNL 34518 (1997).

[10] Hunting the Quark Gluon Plasma BNL-73847 Formal Report (2005).

[11] Quark Matter Talk by P.Seyboth http://qm2008.bnl.gov/Program/4Feb/seyboth.pdf

[12] U. heinz and M. Jacobs, nucl-th/0002042.

[13] Proceedings of the RIKEN BNL Research Center Workshop on "New Discoveries at RHIC", Formal report BNL-72391-2004.

[14] F. Karsch and E. Laermann, Preprint hep-lat/0305025.

[15] F. Karsch et. al., Phys. Lett. B 478 447 (2000).

[16] L. D. McLerren and T. Toimela, Phys. Rev. D 31 545 (1985).

[17] P. Danielewicz, G. Odyniec, Phys. Lett. 157B, 147 (1985).

[18] A. Hosoya and K. Kajantje, Nucl. Phys. B250 666 (1985).

[19] F. Halzen and H. C Liu, Phys. Rev. D25 1842(1992

[20] W. Sheid, H. Muller and W. Greiner. Phys. Rev. Lett. 32 741 (1974).

[21] H. A. Gustafsson et al., Mod. Phys. Lett, A3 1323 (1988).

[22] C. Adler et al., STAR Coll. Phys. Rev. Lett. 90 032301 (2003).

[23] J. Adams et al., STAR Coll. Phys. Rev. Lett. 92 052302 (2004).

[24] J. Rafelski, B. Muller Phys. Rev. Lett. 48 1066(1982).

[25] B. I. Abelev et. at., Phys. Rev. C 75 064901 (2007).

[26] A.M. Rossi et al., Nucl. Phys. B84 (1975) 269; H. Fesefeldt et al., Nucl. Phys. B147 (1979) 317; V. Blobel et al., Nucl. Phys. B69 (1974) 454.

[27] F. Antinori et al J. Phys. G: Nucl. Part. Phys. 28 1607 (2002)

[28] C. Adler et. al., STAR Coll. Phys. Rev. Lett. 89 092301 (2002).

[29] C. Adler et al., STAR Coll. Phys. Lett. B 595 143 (2004).

[30] T. Matsui and H. Satz Physics Letter B178 416 (1986).

[31] C. Y.Wong Nucl. Phys. A 610 434c (1996).

[32] M. Gonin et al., Nucl. Phys. A 610, 404c (1996).

[33] M. Wysocki, J.Phys.G 31 S291 (2005).

[34] M. C. Abreu et. al., Phys. Lett. B 477 28 (2000).

[35] D. K. Srivastava, B. Sinha, M. Gyulassy and X. N. Wang, Phys. Lett. B 276, 185, (1992).

[36] M. M. Aggarwal et. al., Phys. Rev. Lett. 85 3595 (2000).

[37] M. M. Aggarwal et. al., Nucl.Phys.A698:135-142,(2002).

[38] J. D. Brojken Phys. Rev. D 27 140 (1983).

[39] D. H. Perkins, Introduction to High Energy Physics, Cambridge University Press (2000);

[40] M. Gyulassy, I. Vitev, X.N. Wang, B.W. Zhang, Jet quenching and radiative energy loss in dense nuclear matter, in: R.C. Hwa, X.N. Wang (Eds.), Quark Gluon Plasma 3, World Scientific, Singapore,2003.

[41] J. Adams et. al., STAR Coll. Phys. Rev. Lett. 91 072304 (2003).

[42] J. Adams et. al., STAR Coll. Phys. Rev. Lett. 93 252301 (2004).

[43] J. Adams et. al., STAR Coll. Phys. Rev. Lett. 95 152301 (2005).

[44] Gordon Baym and Henning Heiselberg,Phys. Lett. B 469 7 (1999).

[45] M. M. Aggarwal et al, WA98 Coll. Phys. Rev. C 67 044901 (2003).

[46] B.Mohanty and J. Serreau, Phys. Rept. 414 263 (2003).

[47] C. Lourenco, hep-ex/0105053

[48] K. Adcox, et al., PHENIX Coll. Phys. Rev. Lett. 87 052301 (2001).

[49] S. Adler, et al., PHENIX Coll. Phys. Rev. Lett. 91 172301 (2003).

[50] J. Adams, et al., STAR Coll. Phys. Rev. Lett. 91 172302 (2002).

[51] C. Adler, et al., STAR Coll. Phys. Rev. Lett. 90 082302 (2003).

[52] I. Arsene, et al., BRAHMS Coll. Phys. Rev. Lett. 91 072305 (2003).

[53] K. Adcox, et al., PHENIX Coll. Phys. Rev. Lett. 88 022301 (2002)

[54] E. Iancu, R. Venugopalan, The color glass condensate and high-energy scattering in QCD,in: R.C. Hwa, X.N. Wang (Eds.), Quark Gluon Plasma 3, World Scientific, Singapore, 2003.

[55] I.G. Bearden, et al., BRAHMS Coll. Phys. Rev. Lett. 90 102301 (2003).

[56] C. Adler, et al., STAR Coll. Phys. Rev. Lett. 87 082301 (2001).

Chapter 2

STAR Experiment at RHIC

2.1 Relativistic Heavy Ion Collider (RHIC)

The Relativistic Heavy Ion Collider (RHIC) [1] at Brookhaven National Laboratory (BNL) is the first hadron accelerator which consists of two independent rings for colliding two beams of both same and different species of ions ranging from protons(p) to gold(Au) at energies ranging from $\sqrt{s_{_{NN}}}$ =19 GeV to $\sqrt{s_{_{NN}}}$ = 200 GeV for $Au + Au$ and $\sqrt{s_{_{NN}}}$= 500 GeV for $p + p$ collisions. The RHIC can give the luminosities upto $2 \times 10^{26} cm^{-2}/s^{-1}$ for $Au + Au$ and $2 \times 10^{32} cm^{-2}/s^{-1}$ for $p + p$ collisions. Upto 112 particle bunches per ring can be injected, in which case the time interval between bunch crossings is 10 ns. Also RHIC is designed to support an impressive polarized proton-proton spin program designed to determine the gluon contribution in the proton spin. Collision of asymmetric species *i.e*, different species in the two beams (i.e, $d+Au$) is also possible. This diversity allows the study of the colliding systems as a function of both energy and system size. The subsystems of RHIC are Tandem Van de Graff facility, a proton linear accelerator(LINAC), the Booster synchrotron, the Alternating Gradient Synchrotron(AGS) and the RHIC synchrotron rings. Each RHIC storage ring is 3.83 Km in circumference and is designed with six interaction points at which beam collisions

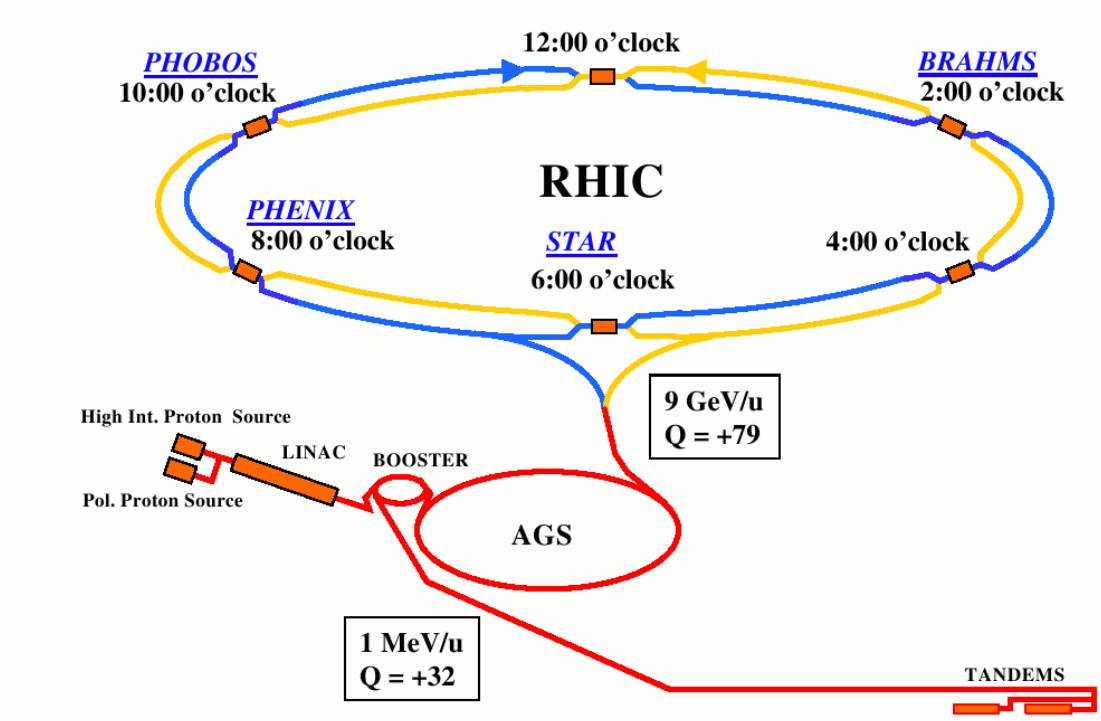

Figure 2.1: *A schematic diagram of RHIC at BNL showing two (Blue and Yellow) 3.8Km ring with four experiments STAR, PHENIX, PHOBOS and BRAHMS.*

are possible. Each collision point corresponding to particular experiments (STAR [2], BRAHMS [3], PHOBOS [4] and PHENIX [5]) is shown in schematic diagram of RHIC with its components in the Figure 2.1.

The First physics run took place in 2000, with $Au+Au$ at $\sqrt{s_{_{NN}}} = 130$ GeV followed by $Au+Au$ collisions at $\sqrt{s_{_{NN}}}$= 200, 62.4, 19.6 GeV, $Cu+Cu$ collisions at $\sqrt{s_{_{NN}}}$= 200, 62.4, 19.6 GeV, $d+Au$ collisions at $\sqrt{s_{_{NN}}} = 200$ GeV and polarized $p+p$ collisions at $\sqrt{s_{_{NN}}} = 200$ GeV. The analysis presented in this thesis is based on the data acquired during the run IV and V. The specifications of those are discussed in the following chapters.

2.2 RHIC Experiments

There were four major experiments at RHIC. The smaller experiments BRAHMS (Broad Range Hadron Magnetic Spectrometers) and PHOBOS, are located at the 2 and 10 o'clock positions respectively. The BRAHMS experiment is designed to measure identified charged hadrons $\pi^{\pm}$, $p^{\pm}$, $k^{\pm}$ over a wide range of rapidity ($0 < |\eta| < 4$) and transverse momentum ($0.2 \leq p_T \leq 3$) GeV/c to study the reaction mechanism and the properties of the highly excited nuclear matter formed in relativistic heavy ion reactions at RHIC. The PHOBOS consists of many silicon detectors surrounding the interaction region. PHOBOS consists of four subsystems: a multiplicity Array, a Vertex detector, a two-arm Magnetic Spectrometer including time-of-flight wall and several trigger detectors which also determine the centrality of collisions. It focuses on detailed study of the centrality dependence of charged hadron multiplicities, spectra and particle ratio in heavy-ion collisions.

The other two large experiments, PHENIX (Poineering High Energy Nuclear Interaction Experiment) and STAR (Solenoidal Tracker at RHIC), are located at the 6 and 8 o'clock positions respectively. The PHENIX Experiment consists of a collection of detectors, each of which perform a specific role in the measurement of the results of a heavy ion collisions. The detectors are grouped into two central arms, which are capable of measuring a variety of particles including pions, protons, kaons, deuterons, photons, and electrons, and two forward muon arms which focus on the measurement of muon particles. There are also additional event characterization detectors that provide additional information about a collision, and a set of three huge magnets that bend the trajectories of the charged particles. The STAR (Solenoidal Tracker At RHIC) detector is designed to investigate the behavior of the strongly interacting matter at high energy density and to look for the signature of the quark-gluon plasma (QGP) formation via the detection of hadronic as well as electromagnetic observables. The details to the STAR

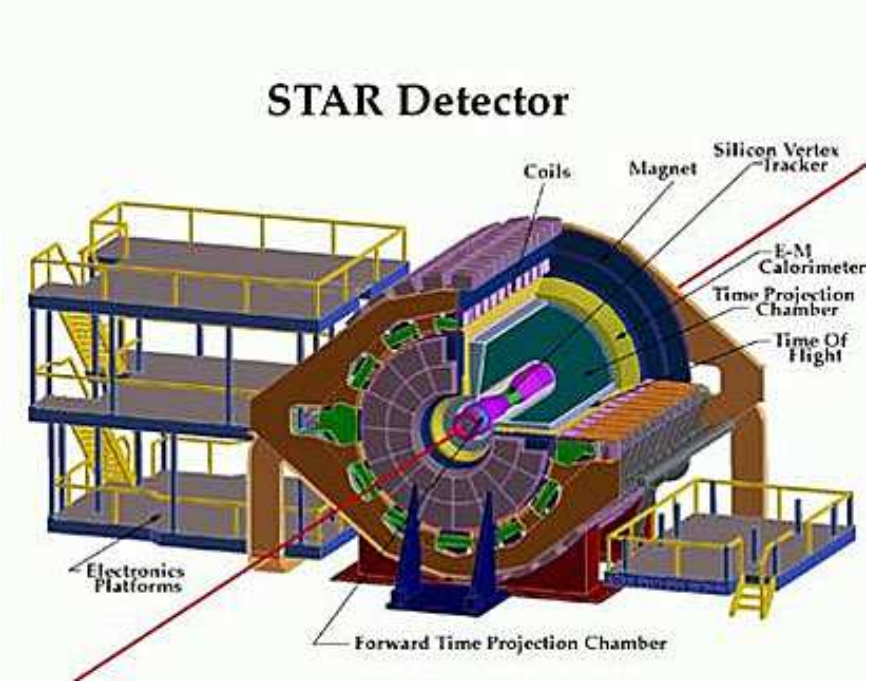

Figure 2.2: *A Perspective view of STAR detector, with a cutway for viewing the inner detector systems at RHIC. The beam axis is illustrated by the red line.*

experiment is given in the next section. The four experiments were designed with some overlap and some complementarity in the physics processes they could measure.

2.3 STAR Experiment

The Solenoidal Tracker at RHIC (STAR) is an experiment which specializes in tracking thousands of particles produced by each ion collision at RHIC. The layout of the STAR experiment is shown in the Figure 2.2. STAR consists of several types of detectors, each specializing in detecting and characterizing certain types of particles. These detectors work together with an advanced data acquisition and subsequent physics analysis that allows final statements to be made about the collision.

A room temperature solenoidal magnet [6] with a maximum magnetic field of 0.5T

provides a uniform magnetic field for charged particle momentum analysis. Charged particle tracking close to the interaction region is accomplished by a Silicon Vertex Tracker (SVT) [7] and a Silicon Strip Detector (SSD) [8]. The silicon detectors cover a pseudo-rapidity range $\mid \eta \mid \leq 1$ with complete azimuthal symmetry ($\Delta\phi = 2\pi$). Silicon tracking close to the interaction allows precision localization of the primary interaction vertex and identification of secondary vertices from weak decays, for example of Λ, Ξ, and Ωs. A large volume Time Projection Chamber [9] (TPC) for charged particle tracking and particle identification is located at a radial distance from 50 to 200 cm from the beam axis. The TPC is 4 meters long and it covers a pseudo-rapidity range $\mid \eta \mid \leq 1.8$ for tracking with complete azimuthal symmetry ($\Delta\phi = 2\pi$). The particle identifications using ionization energy loss are achieved within TPC, with a combined energy loss resolution (dE/dx) of 7% (σ). The momentum resolution of the TPC reach a value of δp/p = 0.02. The δp/p resolution improves as the number of hit points along the track increases and as the momentum of the particle decreases, as expected.

To extend the tracking to the forward region, a radial-drift TPC (FTPC) [10] is installed covering $2.5 < \mid \eta \mid < 4$, also with complete azimuthal coverage (2π) and symmetry. To extend the particle identification in STAR over larger momenta for identified single-particle spectra at mid rapidity, Time-Of-Flight (TOF) detector is installed covering the $-1 < \mid \eta \mid < 0$, and $\Delta\phi = \pi/30$. For the Time-Of-Flight system, the pseudo-Vertex Position Detector(pVPD) was installed as the start-timing detector which is 5.4m away from TPC center and covers $4.43 < \mid \eta \mid < 4.94$ with the azimuthal coverage 19%.

The Electro-Magnetic Calorimeter (EMC) [11] covers $-1 < \eta < -2$ with full azimuthal angle. This system will allow measurement of the transverse energy of events, and trigger on and measure high transverse momentum photons, electrons, and electromagnetically decaying hadrons. The EMC's include shower-maximum detectors to distinguish high momentum single photons from photon pairs resulting from π^0 and η

meson decays. The EMC's also provide prompt charged particle signals essential to discriminate against pileup tracks in the TPC, arising from other beam crossings falling within the 40μsec drift time of the TPC, which are anticipated to be prevalent at RHIC pp collision luminosities ($\approx 10^{32} cm^{-2} s^{-1}$).

The fast detectors that provide input to the trigger system are a central trigger barrel (CTB) [12] at $\mid \eta \mid < 1$ and zero-degree calorimeters (ZDC) [13] located in the forward direction at $\theta < 2$ mrad. The CTB surrounds the outer cylinder of the TPC, and triggers on the flux of charged-particles in the midrapidity region. The ZDCs are used for determining the energy in neutral particles remaining in the forward directions. Each experiment at RHIC has a complement of ZDC's for triggering and cross-calibrating the centrality trigger between experiments. A minimum bias trigger is obtained by selecting events with a pulse height larger than that of one neutron in each of the forward ZDC's, which corresponds to 95% of the geometrical cross section.

Details about all STAR - subdetectors can be found in [14], where comprehensive discussions have been made on RHIC experiments. In this chapter, we discuss details of few subdetectors which we have used in the work presented here either as trigger detectors or as main detectors. We discuss here details of the Time Projection Chamber (TPC),the Forward Time Projection Chamber (FTPC), the trigger detectors (CTB, EMCs, and ZDC) and the Photon Multiplicity Detector (PMD) in details.

2.3.1 The STAR Time Projection Chamber

The TPC is the main tracking detector in STAR and one of the important detectors used in the reconstruction of the events used in the analysis presented in this thesis. It records the tracks of particles, measures their momenta and identifies the particles by measuring their ionization loss (dE/dx), providing complete tracking for charged particles within ± 1.8 units of pseudorapidity through the full azimuthal angle ($\Delta\phi = 2\pi$) and over the

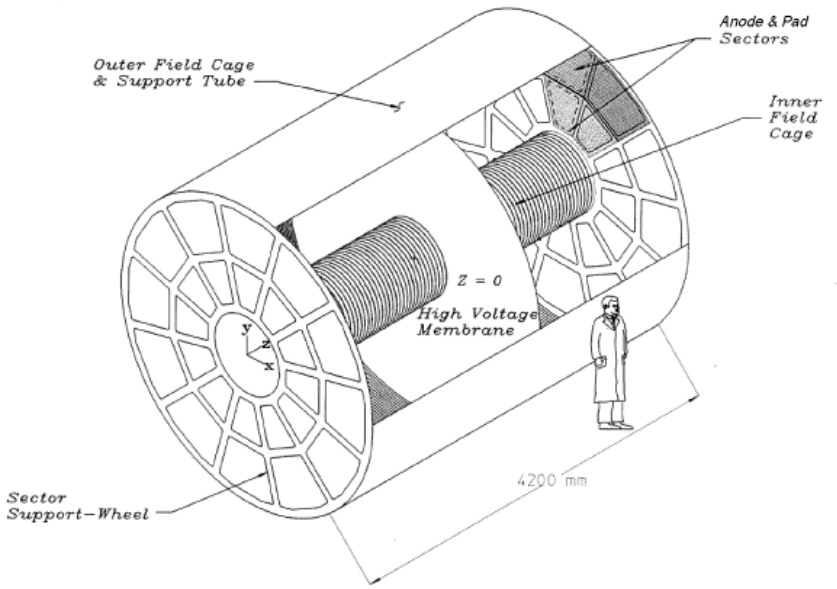

Figure 2.3: *The general view of STAR TPC showing the inner and outer field cages, the central membrane and the 12 sectors of each end cap*

full range of multiplicities up to $\sim 4.10^3$ particles per event. Particles are identified over a momentum range from 100 MeV/c to around 1 GeV/c and momenta are measured over a range of 100 MeV/c to 30 GeV/c.

A TPC detector is a large 3 dimensional gas filled vessel in a well defined electric field. When a charge particle traverses the gas, it creates ionization pairs, that the electric field prevents from recombining, and the electrons drift quickly towards the readout chambers located at the ends of the TPC. The drift field is chosen such that it is not strong enough to create secondary electron-ion pairs.

The STAR TPC surrounds the beam-beam interaction region and its drift volume is limited by 2 concentric field cage cylinders, of radii 50 cm and 200 cm, and the end caps as shown in Figure 2.3. It is 4.2 m long. It is filled with P10 gas (10 % methane and 90% argon) at 2 mbar above the atmospheric pressure [15]. The main property of this gas is a fast drift velocity which peaks at a low electric field. There is a central

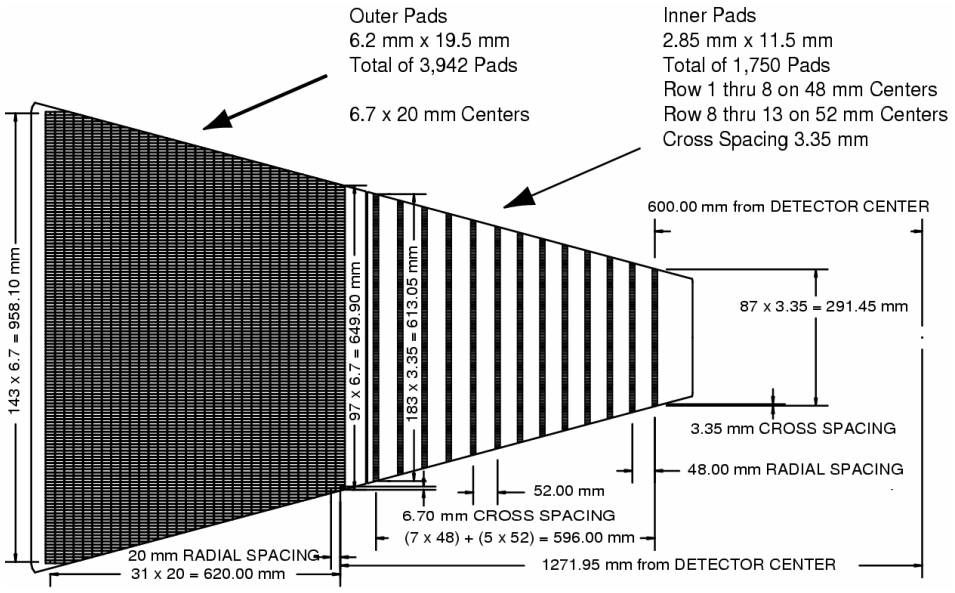

Figure 2.4: *The anode pad plane with full sector. The inner and outer sub-sectors are shown in the right and left respectively.*

membrane held at 28 kV that, together with the equipotential rings along the inner and the outer field cage, creates a uniform drift field of 135 V/cm from the central membrane to the ground end caps where the readout chambers are located.

The readout systems is based on Multi Wire proportional Chambers (MWPC) with readout pads [16]. The readout pads are arranged in 12 sectors around the endcaps which can be seen in Figure 2.4. There are 45 padrows, radially located between the inner and outer radii, in each sector. Each sector is divided in inner (13 padrows) and outer(32 padrows) subsectors. The outer subsectors have continuous pad coverage to optimize the dE/dx measurements. The inner subsectors are in the region of highest track density and are optimized for good two-hit resolution, using smaller pads.

The readout chamber is separated from the drift region by gating grid. The gating grid is a plane of wires that electronically separates the amplification region from the drift region. It is usually close to prevent ions created in the amplification region from

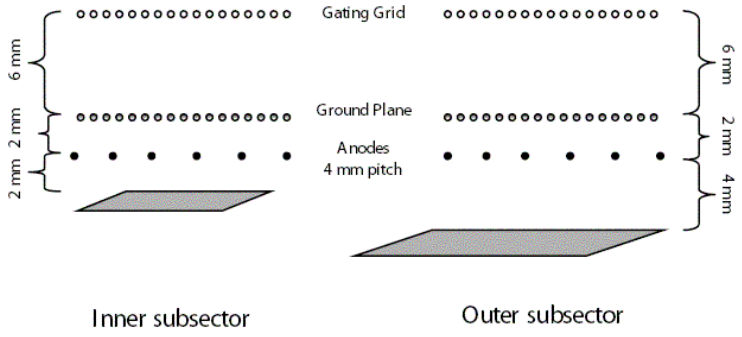

Figure 2.5: *The readout chamber region of the STAR TPC. The gating grid and ground plane wires are on a 1 mm pitch, while the anode wires are spaced every 4 mm.*

getting back into the drift region. When an event is to be recorded, the gating grid wires are set to voltages that allow electrons to pass through. The readout chamber consist of two wire planes: a ground plane and anode wires , located above the pad plane as shown in Figure 2.5. The ground plane shields the TPC drift region from the strong fields around the anode wires. As electrons drift pass the gating grid and the ground plane, they accelerate towards the anode wire where they initiate an avalanche, leaving a cloud of positively charged ions remaining around the wires. The pad image this charge, that goes to the electronics. The size and shape of the ion cloud depends on the number of primary ions, drift distance, diffusion and gas gain.

2.3.1.1 Particle Identification (PID) of TPC by dE/dx

Energy lost in the TPC gas is a valuable tool for identifying particles species. It works especially well for low momentum particles but as the particle energy rises, the energy loss becomes less mass-dependent and it is hard to separate particles with velocities $v > 0.7c$ [17]. For a particle with charge z (in units of e) and speed $\beta = v/c$ passing

through a medium with density, the mean energy loss it suffers can be described by the Bethe-Bloch formula:

$$\frac{dE}{dx} = 4\pi N_0 r_e^2 m_e c^2 z^2 \frac{Z}{A\beta^2}[ln\frac{\sqrt{2m_e\gamma^2\beta^2 E_M}}{I} - \frac{\beta^2}{2} - \frac{\delta}{2}]$$

where N_0 is Avogadro's number, m_e is the electron mass, $r_e(= e^2/m_e)$ is the classical electron radius, c is the speed of light, Z is the atomic number of the absorber, A is the atomic weight of the absorber, $\gamma = 1/\sqrt{1-\beta^2}$, I is the mean excitation energy, and $E_M(= 2m_e c^2\beta^2/1-\beta^2)$ is the maximum transferable energy in a single collision [18, 19]. From the above equation, we can see that different charged particles (electron, muon, pion, kaon, proton or deuteron) with the same momentum p passing through the TPC gas can result in different energy loss. The Figure 2.6 shows the energy loss for particles in the TPC as a function of the particle momentum, which includes both primary and secondary particles. We can see that charged pions and kaons can be identified upto about transverse momentum 0.75 GeV/c and protons and anti-protons can be identified to 1.1GeV/c. An online display of the particles produced in the central $Au+Au$ collisions at $\sqrt{s_{_{NN}}} = 200$ GeV is shown in the Figure 2.7.

In order to quantitatively describe the particle identification, we define the variable $N_{\sigma\pi}$ (in the case of charged pion identification) as

$$N_{\sigma\pi} = \left[\frac{dE}{dx}_{meas} - \frac{dE}{dx}\right] / \left[\frac{0.55}{\sqrt{N}}\frac{dE}{dx_{meas}}\right] \tag{2.2}$$

in which N is the number of hits for a track in the TPC, $\frac{dE}{dx}_{meas}$ is the measured energy loss of a track and $\frac{dE}{dx}$is the mean energy loss for charged pions. In order to identify charged kaons, protons and anti-protons, we have similar definition of $N_{\sigma K}$ and $N_{\sigma p}$. Thus we can cut on the variables $N_{\sigma\pi}$, $N_{\sigma K}$ and $N_{\sigma p}$ to select different particles species. A specific part of the particle identification is the topological identification of neutral particles, such as K^0_S and Λ. These neutral particles can be reconstructed by identifying

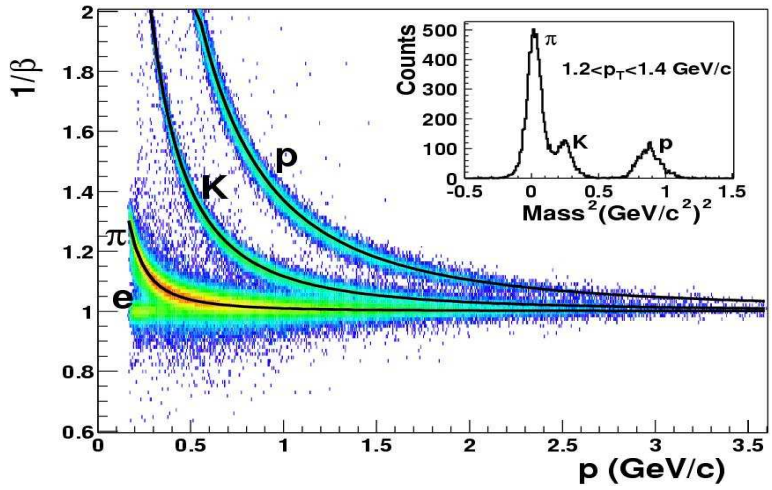

Figure 2.6: *The energy loss distribution of primary and secondary particles in STAR TPC as functions of momentum (p). Separations between pions and kaons, protons and mesons are achieved up to* $p \sim 1.6$ *and* ~ 3.0 *Gev/c, respectively. The insert plot shows* $m^2 = p^2(1/\beta^2 - 1)$ *for* $1.2 < p_{_T} < 1.4$ *Gev/c.*

the secondary vertex, commonly called V_0 vertex of the charge daughter decay modes, $K^0_S \rightarrow \pi^+\pi^-$ and $\Lambda \rightarrow p\pi^-$ [21].

2.3.2 Forward Time Projection Chamber

Two cylindrical Forward Time Projection Chambers (FTPC) [8] were constructed to extend the phase space coverage of the STAR experiment to the region $2.5 < |\eta| < 4.0$ on both sides of STAR and measure momenta and production rates of positively and negatively charged particles. The increased acceptance improves the general event charge characterization in STAR and allows the study of asymmetric collision system like $p+A$ collisions. For optimal use of the available space and in order to cope with the high track density of central $Au+Au$ collisions at RHIC, a novel design was developed using radial drift in a low diffusion gas. From prototype measurements a 2-track resolution of 1 - 2 mm is expected. Argon and Carbon dioxide in ratio 50% : 50% mixture was selected

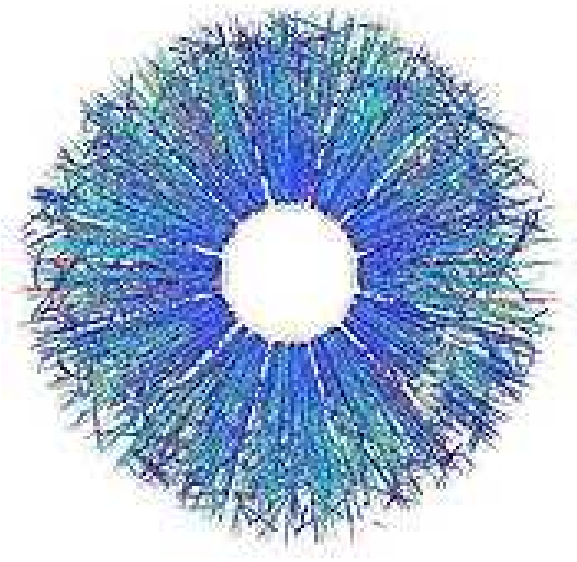

Figure 2.7: *An online display of Au+Au central event in the STAR experiment at RHIC energy. All 12 sectors from one end of the TPC are shown.*

which is non-flammable, shows no or little ageing effect in comparison to hydrocarbons as is chemically less aggressive than the mixture of gas with DME. Final design of the both FTPCs is shown in the Figure 2.8.

FTPC is a cylindrical structure, 75 cm in diameter and 120 cm long, with a radial drift field and readout chambers located in 5 rings on the outer cylindrical surface. Each ring has two padrows and is subdivided azimuthally into 6 readout chambers. The radial drift configuration was chosen to improve the two-track separation in the region close to the beam pipe where the particle density is highest. The field cage is formed by the inner HV-electrode, a thin metalized plastic tube, and the outer cylinder wall at ground potential. The field region at both ends is closed by a planar structure of concentric rings, made of thin aluminum pipes. The front end electronics (FEE), which amplifies, shapes, and digitizes the signals, is mounted on the back of the readout chambers. Each particle trajectory is sampled up to 10 times. The ionization electrons are drifted to the

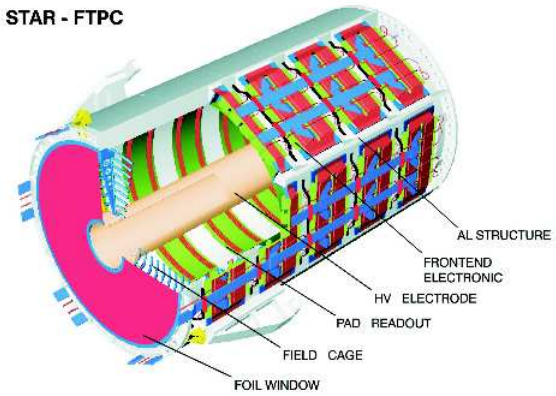

Figure 2.8: *Schematic diagram of an FTPCs for the STAR experiment. The field cage with potential rings at the endcaps, the padrows on the outer surface of the gas volume and the front end electronics are shown.*

anode sense wires and induced signals on the adjacent cathode surface are read out by 9600 pads (each 1.6×20 mm^2). The above design has some unusual and new features for a TPC as listed below:

- The electrons drift in a radial electrical field perpendicular to the solenoidal magnetic field.
- Curved readout chambers are used to keep the radial field as ideal as possible.
- A two-track separation of 1-2 mm is expected, which is an order of magnitude better than in all previously built TPCs with pad readout.

2.3.2.1 Reconstruction of FTPC Tracks

The first step in the reconstruction of tracks is to calculate the track points (cluster finding) from the charge distribution measured by the readout electronics. In a second

step (track finding), these track points are grouped to tracks. Using the magnetic field map, upto ten position measurements per track are then used to fit the momentum.

2.3.2.2 Cluster Finding

The reconstruction of track points is done by the FTPC cluster finding program [21]. It is optimized to deal with high track densities while minimizing the use of computing time. The program reads in the electronic signal data from the data acquisition system, looks for areas of nonzero charge (cluster), deconvolutes clusters and fits the point coordinates. The transformation from pad position and drift time into Cartesian coordinates includes the correction of distortions introduced by the magnetic field.

2.3.2.3 Track Reconstruction

The second step in the analysis of FTPC data is the reconstruction of the particle tracks and their momenta. The FTPC track reconstruction code is based on an algorithm developed for fast online reconstruction [22]. It is a conventional track-following algorithm optimized for minimum use of computing power. In this code all position calculations are done in a transformed coordinate system in which points appear on a straight line if they form a helix in Cartesian coordinates. This processing step is known as conformal mapping [23]. It saves calculation time in the track fitting, because all fits can be done by linear regression. After the track finding step the code determines a primary vertex position by extrapolating and intersecting all the reconstructed tracks. Finally the particle momenta are fitted using the magnetic field map and the vertex position. Figure 2.9 shows a reconstructed event in FTPC for a central $Au + Au$ collision at $\sqrt{s_{NN}} = 200$ GeV.

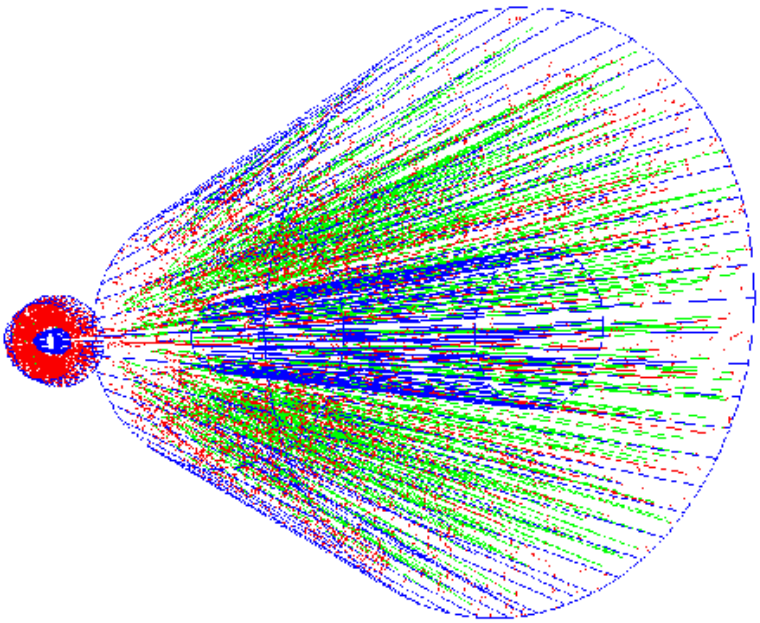

Figure 2.9: *Reconstructed tracks in both the Forward Time Projection Chambers (FTPCs) from Au+Au collisions at* $\sqrt{s_{NN}}$ *= 200 GeV.*

2.3.3 Trigger Detectors

The Solenoidal Tracker at RHIC (STAR) is designed to detect charged and neutral particles produced in relativistic heavy ion collisions. The majority of the STAR data is provided by relatively slow detectors: TPC, SVT, FTPC, PMD. The trigger system must look at every RHIC crossing and decide whether or not to accept that event and initiate recording the data. The elements of the trigger system are two zero-degree calorimeters (ZDC), two beam-beam counters (BBC), the multi-wire proportional chamber (MWPC), the central trigger barrel (CTB), barrel electromagnetic calorimeter (BEMC) and the endcap electromagnetic calorimeter (EEMC). These are shown in Figure 2.10.

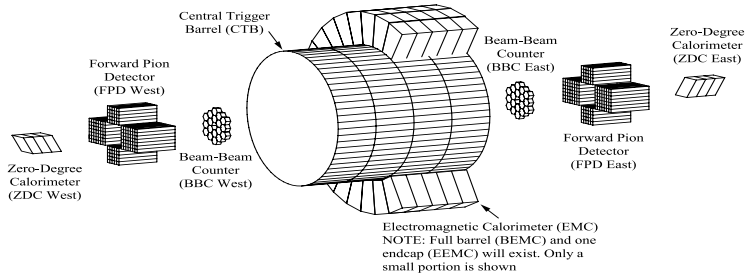

Figure 2.10: *Schematic diagram for Trigger detectors showing the two ZDCs, two BBCs, two FPDs, CTB and Electromagnetic Calorimeters in STAR experiment.*

2.3.3.1 Zero Degree Calorimeter

The Zero Degree Calorimeter is used to monitor RHIC luminosities and to provide the minimum bias trigger in the $d + Au$, $Cu + Cu$ and $Au + Au$ collisions. The purpose of this detector is to measure the total multiplicity of the neutrons emitted from the nuclear fragments after collisions. The ZDC is a sampling calorimeter placed on both sides of each experimental hall along the beam pipe(rings) at distance of 18 m from the interaction points behind the beam splitting DX dipoles between the two beam pipes. ZDC consists of alternating layers of tungsten absorbers and Cherenkov fibers with a total length of about 0.7 m as shown in Figure 2.11. Transversely the space between two beam pipes allows the calorimeter width of about 11 cm which covers 2.5m radian around the forward direction. The ZDC timing resolution is $\sim$ 100 psec depending on the electronics setup, empirical slewing corrections. Since ZDC can measure time in 2 ZDC's, on either side of the IR, we can derive 2 quantities from them- the vertex position

and the event time.

2.3.3.2 Central Trigger Barrel

The main purpose of the Central Trigger Barrels (CTB) is to measure charged particle multiplicity over $-1 < \eta < 1$. It consists of 240 scintillator slats arranged in four cylindrical bands each covering half unit of pseudorapidity. The CTB slats are located on the outer shell of the 4m diameter of TPC. The two slats are kept in aluminum trays and each slat has one radiator, one light guide and one Photo Multiplier tube (PMT). Figure 2.12 shows a segment with two slats. The PMT signals generated by the slats are sent to digitizer boards each having 16 inputs. From each digitizer, the signals are sent to an integrator, an 8-bit ADC and then to a discriminator. The output of the discriminators over the barrel is then used in the trigger logic.

2.3.3.3 Beam Beam Counter

Due to low multiplicity in the $p + p$ collisions, one can not use CTB and ZDC detectors as trigger detectors since there are no neutrons in the colliding beams. An additional trigger detector, the Beam Beam Counter (BBC) is implemented for $p + p$ collisions. There are two BBC detectors on the outside of the east and west pole tips of the STAR magnet located at 3.5 meters away from the interaction point and covers pseudorapidity $3.3 < |\eta| < 5.0$. Each BBC consists of two rings of hexagonal scintillator tiles, the outer ring composed of large tiles and the inner ring composed of small tiles as shown in the Figure 2.13. The BBC detects minimum bias interactions for $p+p$ and $nucleus+nucleus$ collisions. The timing difference between its two counters locates the primary vertex position.

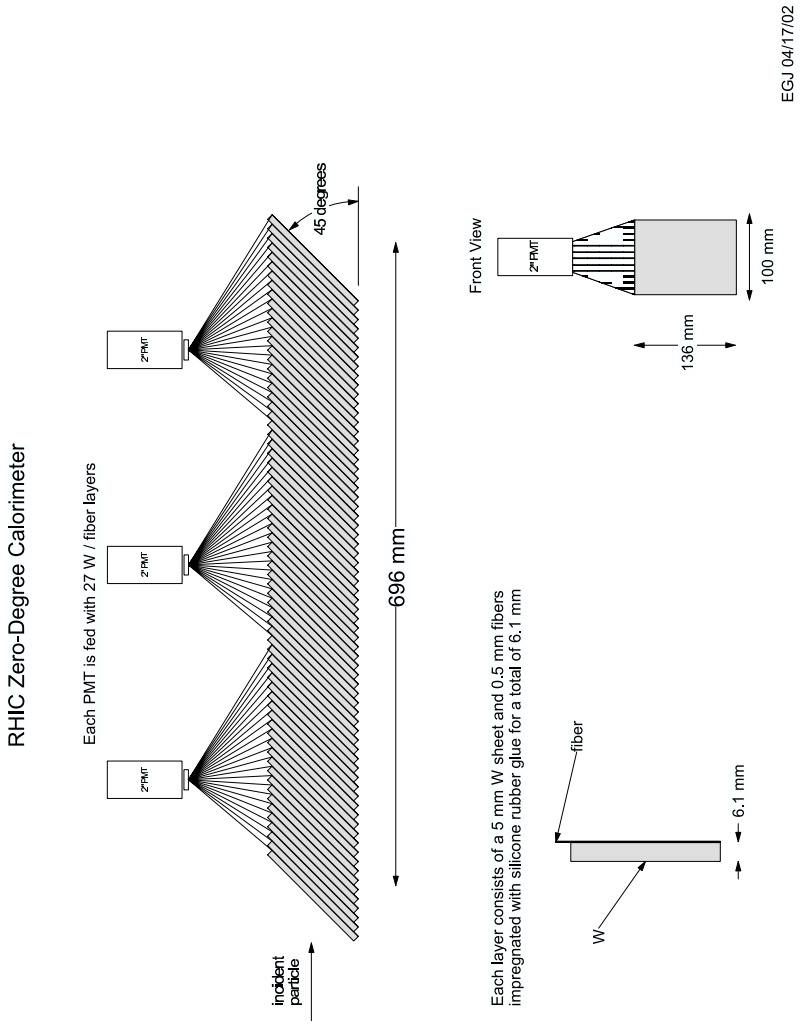

Figure 2.11: *Diagram of Zero Degree Calorimeter layout in STAR experiment.*

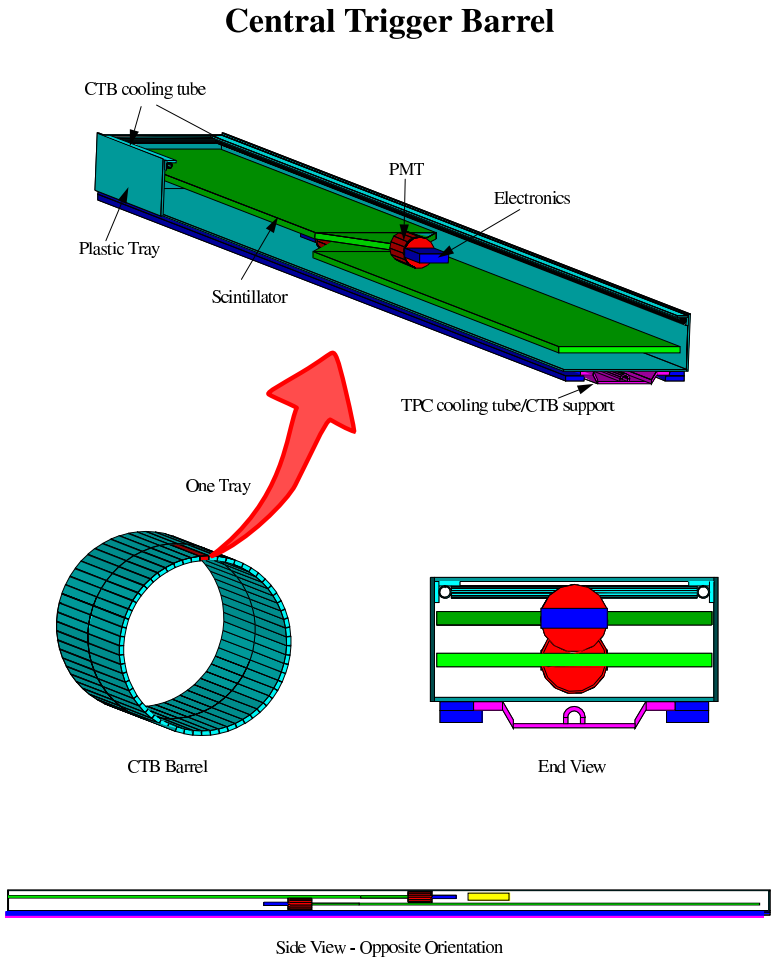

Figure 2.12: *Layout of Central Trigger Barrel with the details of tray and slat.*

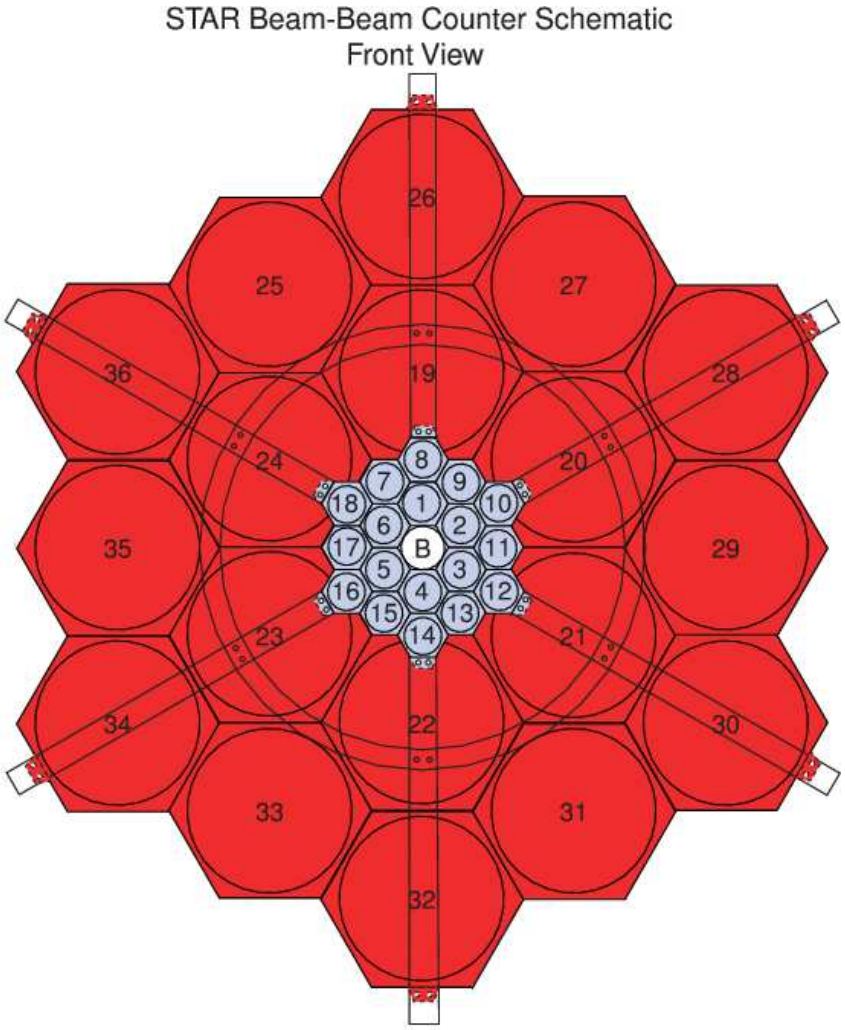

Figure 2.13: *Layout of the Beam Beam Counter (BBC) showing two rings of scintillator tiles: outer and inner.*

2.3.3.4 Barrel and Endcap Electromagnetic Calorimeter

Barrel Electromagnetic Calorimeter (BEMC)

STAR utilizes the BEMC to trigger on and study rarer , high-p_T processes (jets, leading hadrons, direct photons, heavy quarks) and provide large acceptance for photons, electrons, π^0 and η mesons in systems spanning polarized p+p through Au+Au collisions. The STAR BEMC is a sampling calorimeter and consists of layers of lead scintillator stack and shower maximum detector at approximately 5 radiation lengths from the front plane. There are 20 layers of 5mm thick lead, 19 layers of 5mm thick scintillator and 2 layers of 6mm thick scintillator, the later are also read out separately in the preshower part of the calorimeter. BEMC covers pseudorapidity$\pm$ 1 , full azimuthal coverage which matches the TPC acceptance.. The detector is segmented into 120 modules, each covering 6 degrees in ϕ(0.1 radian, 26 cm wide) and 1.0 unit is pseudorapidity. The active depth is 23.5 cm or 21 radiation lengths(X_0) and about 6.6 cm in structural plates of which 1.9 cm lies in front of the detector. Each modules is further divided into 40 towers, 2 in ϕ and 20 in η with each tower being 0.05 in $\Delta\phi$ by 0.05 in $\Delta\eta$. The calorimeter thus is physically segmented into of 4800 towers.

Shower Maximum Detector

A Shower Maximum Detector (SMD) is multi wire proportional counter - strip read-out detector using gas amplification. It is located at $\approx$ 5.6 radiation lengths depth in the calorimeter modules at $\eta = 0$. The SMD is used to provide the better spatial resolution essential for π^0 and η meson reconstruction, direct photon and electron identification. Independent cathode planes with strips along η and ϕ directions allow the reconstruction of a two dimensional image of a shower. Each η strip covers 0.0064 $\times$ 0.05 in $\delta\eta \times \delta\phi$, the ϕ strips are 0.1 $\times$ 0.0064 in $\delta\eta \times \delta\phi$,. There are total of 36000 strips in the full detector.

BEMC Electronics

The BEMC electronics included trigger, readout of phototubes and SMD, high voltage system for phototubes, low voltage power supply, calibration controls and interfaces to STAR trigger, DAQ and slow control. Front End electronics including signal processing, digitization, buffering, formation of trigger primitives and the first level readout is located in custom EMC crates located on outside of the STAR magnet. SMD Front End electronics including preamplifiers and switched capacitor arrays reside on EMC modules inside the STAR magnet.

Endcap Electromagnetic Calorimeter (EEMC)

In addition to the BEMC, there is another calorimeter detector *viz* the Endcap Electromagnetic Calorimeter (EEMC) in STAR experiment. It sits on the west poletip of the STAR detector and provides full azimuthal coverage for high-p_T photons, electrons and electromagnetically decaying mesons over the pseudorapidity range $1.086 \leq \eta \leq 2.00$. It includes a scintillating-strip shower-maximum detector to provide π^0/γ discrimination and preshower and postshower layers to aid in distinguishing between electrons and charged hadrons. The triggering capabilities and coverage it offers are crucial for much of the spin physics program in polarized proton-proton collisions.

The EEMC is an annular detector with full annulus divided into two halves. A standard layer of the calorimeter consists of Pb/stainless steel laminate followed by a 4-mm thick plastic scintillator (Kuraray SCSN-81). Each radiator sheet comprises 4.57-mm thick calcium-loaded Pb sheets laminated on each face with 0.5 mm stainless steel, for a total of ≈ 0.85 radiation lengths. The four specially configured layers provide preshower, postshower and SMD functions.

The tower segmentation is produced using megatile construction and each megatile spans either 6° or 12° in azimuthal angle (ϕ) with machined isolation grooves separating each into 12 or 24 trapezoidal tiles, respectively. Each 30° sector of a calorimeter layer

contains two 12° megatiles, aligned flush against the tie-rods on each side, and a 6° "keystone" megatile. A scintillator strip SMD with high position resolution is located at a depth of about five radiation lengths deep within the EEMC. The SMD is designed to provide the fine granularity to distinguish the transverse shower profiles characteristics of single photons *vs.* the close lying photon from π^0 and η^0. The light from the towers and the scintillator strip SMD are carried through optical fibres to photomultiplier tubes which are mounted on the rear of the poletip. The EEMC trigger electronics and tower readout are similar to the BEMC. STAR Level 0 trigger can compare individual tower ADC values and multi-tower sums to various thresholds and correlated information from other detectors for triggering direct photon and $W^{\pm}$.

2.3.4 Silicon Vertex Tracker (SVT))

The Silicon Vertex Tracker (SVT) is the innermost subsystem of the STAR detector at RHIC. The SVT is based on a novel silicon drift technology which allows excellent hit position resolution in close proximity to the primary vertex, thus improving STAR's vertex and tracking resolution. The SVT also provides an independent measurement of dE/dx which enhances charged particle identification, especially in the low momentum region. The SVT consists of 216 Silicon Drift Detectors (SDD) of dimensions 6.3 X 6.3 cm containing 13 million pixels multiplexed onto just 1300 readout channels which covers the pseudorapidity range of $-1 < \eta < 1$ with full azimuthal coverage. The total active length of SVT is 44.1 cm. The SDDs are arranged in three concentric barrels at distance of 7, 11 and 15 cm around the interaction point. There are 24 SVT readout electronics RDO boxes mounted, 12 on each side of STAR. The RDO system is split into three functional blocks:

(i) a monitoring power, trigger and slow control interface block (PTB),

(ii) an analog -to- digital converter and the data storage block(AMB) and

(iii) a fiber optic transfer block(FOB).

Each RDO box has 54 analog inputs. Data acquisition is performed at 8/3 of the RHIC strobe frequency (25MHz). The readout electronics is able to process and send digitized data to DAQ at 100 events/second.

2.3.5 Silicon Strip Detector (SSD)

The Silicon Strip Detector (SSD) is an upgrade of the current STAR experiment setup, adding a fourth layer to the Silicon Vertex Tracker (SVT) to make inner tracking system located inside the Time Projection Chamber (TPC). This additional fourth layer provides two dimensional hit position and energy loss measurements for charged particles, improving the extrapolation of TPC tracks through SVT hits. It consists of double sided silicon sensors over a surface of around one square meter.To match the high track densities reached at RHIC with $Au+Au$ collisions at $\sqrt{s_{NN}} = 200$ GeV the granularities of the strips is such that the total number of channels reaches 491520. The SSD is placed at a distance of 230 mm from the beam axis, covering a pseudorapidity range of $|\eta| \leq 1.2$ which leads to a total silicon surface close to 1 m^2. The design of the SSD is based on two clam shells, each containing 10 carbon fiber ladders. Each ladder supports 16 wafers using double-sided silicon strip technology (768 strips per side) and connected to the front-end electronics (6 ALICE 128C chips per side) by means of the Tape Automated Bonded (TAB) technology [24]. The ladders are tilted with respect to their long axis, allowing the overlap of the detectors in the transverse plane for better hermiticity and alignment performances. A bus cable transports the analog signals along the ladder to two 10 bits ADC boards installed at both ends. After digitization, the signals are sent to Readout Boards which are linked to the DAQ system through Giga-link optics fibers. The whole system is remotely controlled to monitor powers and temperature but also to calibrate and tune the front-end electronics. The cooling system is based on an

air-flow through the ladder which is embedded in a mylar sheet. The total radiation length has been estimated to be around 1

2.3.6 Photon Multiplicity Detector

The Preshower Photon Multiplicity Detector (PMD) [25] in the STAR experiment is a gas detector that is employed to study the photon production at forward rapidities, Isospin Fluctuations and Collective flow of photons in heavy ion collisions. It consists of a preshower and a charge particle veto (CPV) planes. The detector covers the pseudo-rapidity region $-3.7 \leq \eta \leq -2.3$ with full azimuthal acceptance and is mounted on the east side of the Wide Angle Hall (WAH) of STAR experiment at a distance of 540 cm from the interaction point. The details of Photon Multiplicity Detector will be discussed in the chapter 3.

Bibliography

[1] H. Hahn et al., Nucl. Instrum. Meth. A499, 245 (2003).

[2] F. Videback, et. al., Nucl. Phys. A566, 299c (19994).

[3] B. Wyslouch, et. al., Nucl. Phys. A556, 305c (1994).

[4] J. C.Gregory et al., Nucl. Phys. A556, 287c (19994).

[5] J. W.Harris, et. al., Nucl. Phys. A556, 277c (1994).

[6] F. Bergsma etal, Nucl. Instrum. Meth. A499 633 (2003).

[7] R. Bellwied et al., Nucl. Instrum. Meth. A499, 640 (2003).

[8] L. Arnold, et al., Nucl.Instrum.Meth. A499 652 (2003).

[9] M. Anderson, et al., Nucl.Instrum.Meth. A499 659 (2003).

[10] K. H.Ackermann et al., Nucl.Instrum.Meth. A499 713 (2003).

[11] M. Beddo et al., Nucl. Instrum. Method. A499 725 (2003)

[12] F. S.Bieser et al., Nucl. Instrum. Meth. A 499, 766 (2003).

[13] C. Adler et al., Nucl.Instrum.Meth. A470 488 (2001).

[14] K. H. Ackermann et al., Nucl. Instrum. Method. A 499, 624(2003).

[15] L. Kochenda et al., Nucl. Instrum. Meth. A499, 703 (2003).

[16] M. Anderson et al., Nucl. Instrum. Meth. A499, 679 (2003).

[17] M. Anderson et al., Nucl. Instrum. Meth. A 499, 659 (2003).

[18] H. Zhang, Ph.D.thesis, yale University, (2003).

[19] H. J.Crawford et al., Nucl. Instrum. Meth. A499, 766 (2003).

[20] H. Hümmler, Doctorate Thesis, Technical University, München, Germany, (2000).

[21] P. Yepes, A fast track pattern recognition, Nucl. Instr. Meth. A 380 582 (1996).

[22] M. Oldenburg, Doctorate Thesis, Technical University, München, Germany,

[23] S. Bouvier, A packaging technology used for silicon strip detector to front end electronics interconnection, Proceedings of the 4^{th} workshop on electronics for LHC experiments, Rome, Sept. (1998).

[24] M. M. Aggarwal et al., Nucl.Instrum.Meth. A499 751 (2003).

[25] The STAR Collaboration, The STAR Conceptual Design Report, PUB-5347 (1992),

Chapter 3

Photon Multiplicity Detector

3.1 Introduction

A preshower Photon Multiplicity Detector (PMD) [1] was installed on the east side of the wide angle hall in 2002 in STAR experiment. This detector was designed to measure photon multiplicity in the forward region where high particle density precludes the use of a calorimeter. Figure 3.1 shows the position of PMD relative to other detectors within the STAR setup. The inclusion of the PMD enhances the phase space coverage of STAR with photons considerably, in pseudorapidity $-3.7 \leq \eta \leq -2.3$ with full azimuthal acceptance and in p_T down to about 25 MeV/c [2].

3.2 Principle of Photon Multiplicity Detector

Photon Multiplicity Detector is a preshower detector and measures the multiplicity and spatial distribution of photons on an event by event basis. The basic principle of the measurement of photon multiplicity using the PMD is similar to those of preshower detectors used in WA93 and WA98 experiments at CERN SPS [3,4]. It consists of highly segmented sensitive detector placed behind a lead converter of suitable thickness.

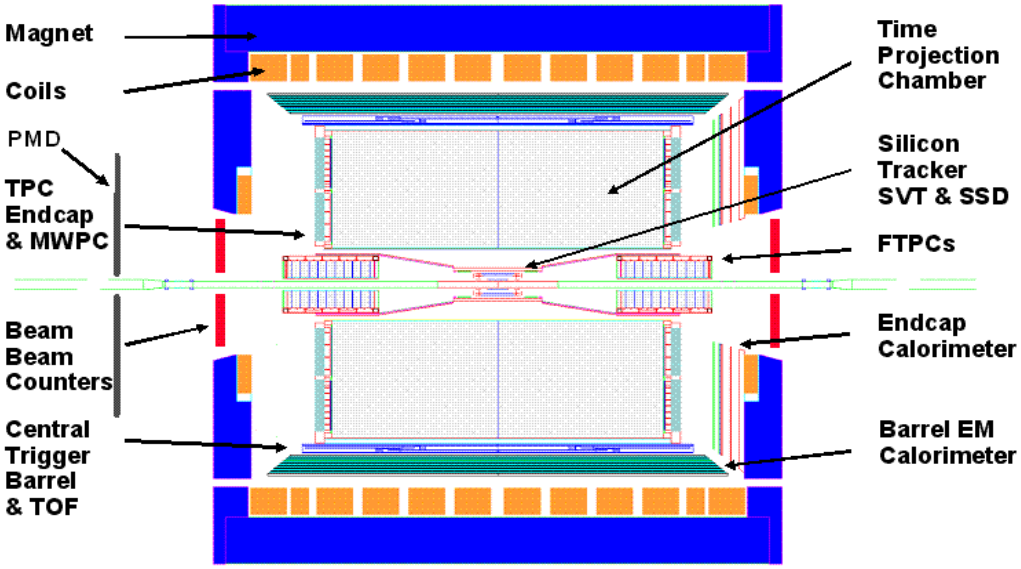

Figure 3.1: *The cross-sectional view of STAR detector showing the position of PMD in the STAR setup relative to other detectors.*

A photon produces an electromagnetic shower on passing through the lead converter. These shower particles produce signals in several cells of the sensitive volume of the detector. Charged hadrons usually affect only one cell and produce a signal resembling those of Minimum Ionizing Particles (MIPs). The thickness of the converter is optimized such that the conversion probability of photons is high and transverse shower spread is small to minimize shower overlap in a high multiplicity environment. In order to have better hadron rejection capability, another plane of the sensitive detector of identical dimension and granularity as of the preshower part is placed before the lead plate, which acts as a veto for charged particles as shown in the Figure 3.2.

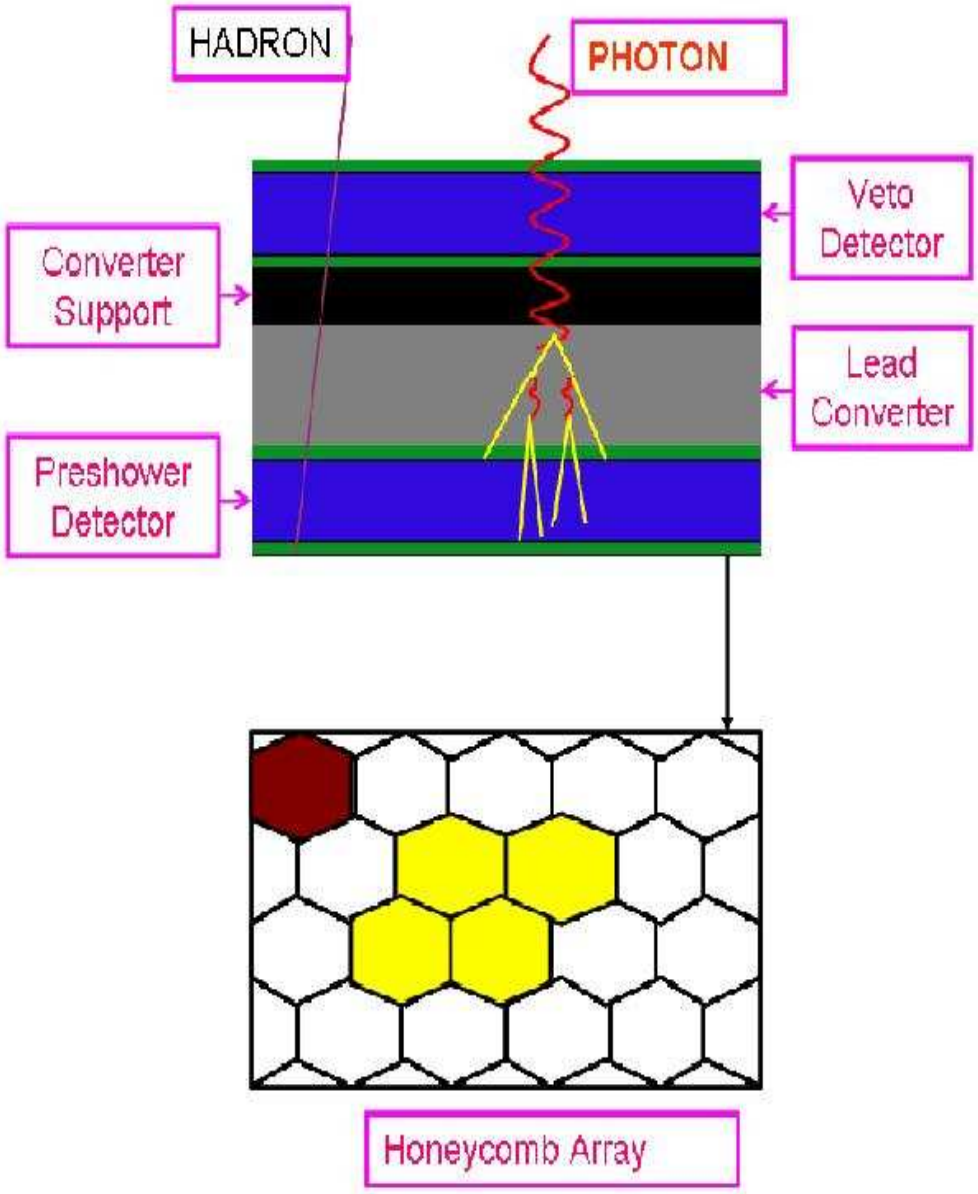

Figure 3.2: *Schematic diagram of photon multiplicity detector and its principle showing the hadrons which gives signal mostly on single cell while photons after interacting with lead converter produce shower and give signal on large number of cells.*

3.3 Description of Photon Multiplicity Detector

The detector is based on a proportional counter design using $Ar + CO_2$ gas mixture. This gas mixture is preferred because of its insensitivity to neutrons. To handle the high particle density in the forward region, the detector technology has been chosen with the following considerations that:

1. Multi-hit probability on each cell should be less.
2. MIP should be contained in one cell.
3. Low energy δ-electrons should be prevented from traveling to nearby cells and causing cross-talk among adjacent cells.

The requirement of granularity and isolation of cells makes the segmentation of the detector gas volume with suitable material effective for reducing δ-electrons from crossing one cell to other. We have used honeycomb cellular geometry with anode wire readout. The copper honeycomb body forms the common cathode and is kept at a large negative potential. It also supports the printed circuit boards (PCBs) which are used for signal collection and for extension of the cathode required for proper field shaping [5].

The detector consists of an array of hexagonal cells as shown schematically in the Figure 3.3 along with a longitudinal section illustrating the extended cathode for the field shaping, which ensures uniform charged particle detection efficiency throughout the cell [6]. A unit cell, the building block of the honeycomb is fabricated using 0.2 mm thick ETP grade copper sheets which are solder-coated on one side. The 24×24 honeycomb cells forms a unit module. The components of unit module are shown in the Figure 3.4. It consists of a custom-built copper honeycomb sandwiched between two printed circuit boards (PCBs) which hold the anode wire and provide extension to cathode. The top PCB, containing the electronics boards, has solder-islands at the center of each cell with a 0.5 mm diameter gold-plated tungsten wire through-hole. Signal tracks from the 64

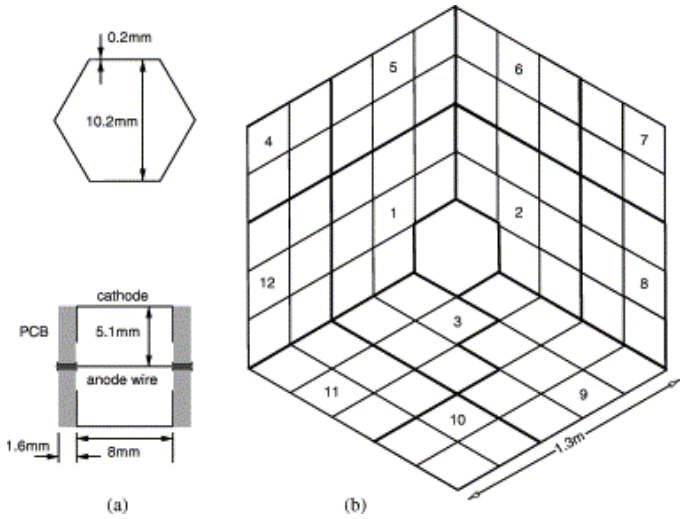

Figure 3.3: *Schematic of Unit cell with cross-section showing the dimensions and the cathode extension and (b) layout of the STAR PMD. Thick lines indicate supermodule boundaries. There are 12 supermodules each in the preshower plane and the veto plane. Divisions within a supermodule denote unit modules.*

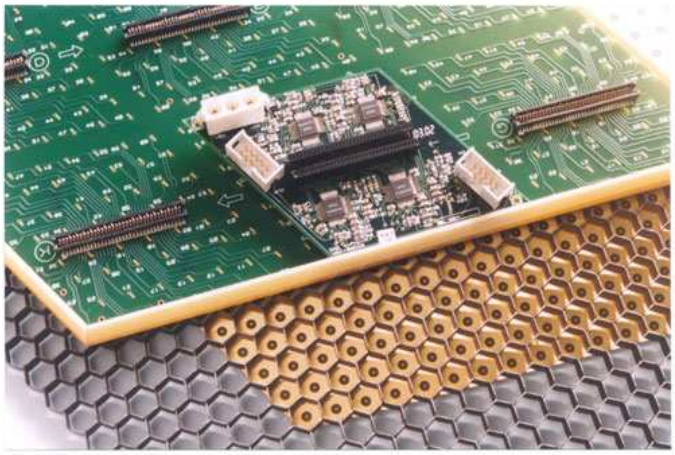

Figure 3.4: *Components of a unit module: copper honeycomb, placed between two PCBs. The top PCB is seen with connectors and a FEE board. The cathode extension on the inside of the bottom PCB and the island separating the anode wire with the cathode is visible through the honeycomb. The photograph was taken with unassembled components.*

cells are brought to 70-pin connector. The gold plated tungsten wire of 20 micrometer diameter is inserted through the holes on the PCBs using a needle and a tensioning jig after applying tension of $\sim$ 30% of the elastic limit.

A set of unit modules are enclosed in a gas-tight chamber called supermodules (SMs). Supermodules are gas-tight chambers made of 3mm thick FR4 grade glass epoxy sheet as the base plates and a 7 mm thick and 25 mm high aluminum boundary walls. The boundary walls are made of custom extruded aluminum channels with a hollow cross-section to facilitate gas flow into the modules. For the application of high voltage (HV) to supermodules, an aluminum enclosure containing a SHV connector, a HV limiting resistor and decoupling capacitor is fixed at one corner of each supermodule. The number of unit modules in a supermodule varies from 4 to 9. The STAR PMD consists of 12 supermodules on each plane arranged in the form of a hexagon as shown in the Figure 3.3. This geometry ensures full azimuthal coverage with minimum number of supermodules.

3.3.1 Support Structure for PMD

The drawing of the support structure is shown in Figure 3.5. It has two parts: (a) the support plates and (b) the suspension movement mechanism. A 5 mm thick flat stainless steel plate is used to support the lead converter plates and supermodules in each half of the PMD. It has tapped holes for screws corresponding to hole positions in the lead plates and in the supermodules. The lead converter plates are sandwiched between two layers of gas detectors. The two halves of the detector are supported on the girders and hang freely in a vertical position. The support structure allows both x- and z-movements of the detector. Each half of the detector can be separated for access by a smooth independent movement controlled by limit switches. The hanging elements have free swinging pivots, fine adjustments for horizontal motion, and plane position adjustments for alignment of the detector. The services of the two halves are

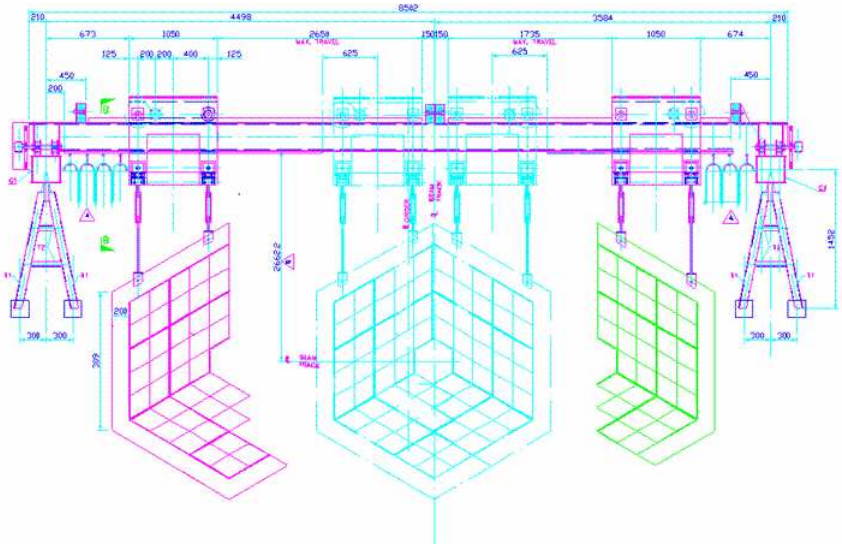

Figure 3.5: *PMD support mechanism. The inner hexagonal part shows the two halves joined during data taking operation. The two halves, when separated for servicing, look as shown on the right and left.*

also independent. When fully open, the two halves provide sufficient clearance for the poletip support of the STAR magnet to move in. The edges of the support plate are also used for mounting the gas feed manifolds, distribution boxes for low voltages supplies and general support for distribution of cables onto the detector.

3.4 Front End Electronics and PMD Readout

The front-end electronics for processing the PMD signals is based on the use of 16-channel GASSIPLEX chips developed at CERN [7] which provide analog multiplexed signals and readout using the custom built ADC board (C-RAMS). One C-RAMS can handle a maximum of 2000 multiplexed signals. Considering the symmetry requirements of the detector hardware, the readout of the entire PMD has been divided into 48 chains. Each chain has 1728 channels and can cover three unit modules.

Each readout chain is driven by: (i) a translator board, (ii) 27 FEE boards each consisting of four GASSIPLEX chips, and (iii) a buffer amplifier board.

(i) Translator Board: It converts NIM levels of all control signals into the level required for the operation of GASSIPLEX chips. Operating voltage for these chips is 2.75V and hence all the NIM signals are to be translated to 0-2.75V levels.

(ii)FEE board: The cells in the unit modules are arranged in clusters consisting of 8×8 cells connected to a 70-pin connector. This cluster of 64 cells is read out by a FEE board having four GASSIPLEX chips. For geometrical considerations the FEE board is also made in rhombus shape. When all the boards are placed on the detector, they almost fully cover the detector area. This arrangement helps to reduce the material and also provides a ground shield for the detector.

(iii) Buffer amplifier board: The buffer amplifier is used for the transmission of a train of analog multiplexed signals to the readout module via a low impedance cable.

3.4.1 PMD Readout, Pre-Trigger and Timing Diagram of PMD

The timing diagram of the generation of pre-trigger and handling of the GASSIPLEX signals is shown in the Figure 3.6. After the RHIC collision has occurred, it is expected that PMD will get pre-trigger after 500 ns and also get the level zero trigger(L0) after after 1.1 micro-sec [8]. A BUSY signal is sent when PMD DAQ gets the pre-trigger. After 814 ns Track/Hold (T/H) is sent to the FEEs. If L0 does not arrive within the predefined time, a clear (CLR) signal is sent to clear the T/H and BUSY signals after 4.5 micro sec as the recovery time of FEEs is 4.5 micro sec. If L0 arrives within pre-defined time then T/H and BUSY signals are sent. For this, one needs to check whether pre-trigger already exits or not. If it exists, then the trigger is sent to the sequencer which in turn generates the CLOCK(CLK), T/H, CLEAR(CLR), BUSY and CONV signals. The clock has to be FAN IN/OUT and sent to several chains of FEE boards. The CONV

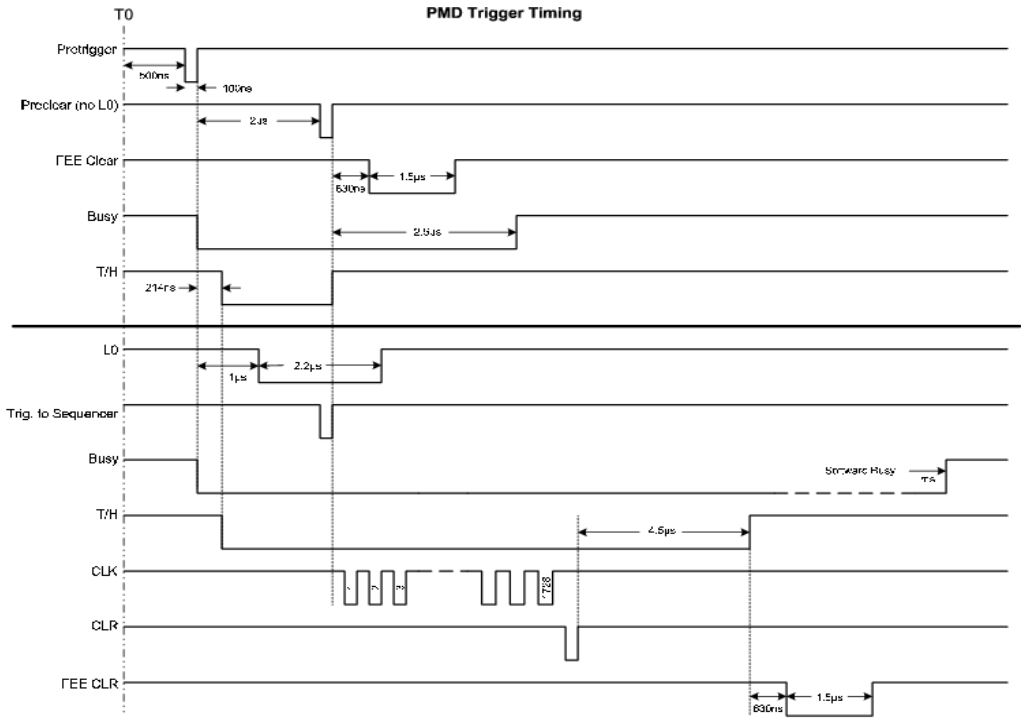

Figure 3.6: *PMD Timing diagram*

signals are passed on, through a delay module, to the C-RAMS. The C-RAMS converts the data and sends a ready signal to the sequencer after which the readout starts. After the readout, a FEE CLR appears when the software BUSY is withdrawn. On the other hand, if pre-trigger does not exists by the time L0 arrive, then both T/H and BUSY are cleared.

3.5 Analysis Method for Photon Multiplicity Detector Data

The STAR experiment at Relativistic Heavy Ion Collider (RHIC) at Brookhaven National Laboratory has unique capability of precise measurement of photon and charged particle multiplicities at forward rapidity using PMD and FTPC. Event-by-event mea-

surements of photon and charged particle multiplicities can be used to study multiplicity fluctuations [9]. For the present analysis we have used data from $Au + Au$ and $Cu + Cu$ collisions at $\sqrt{s_{NN}}$ = 200 GeV. For the $Au + Au$ and $Cu + Cu$ collisions we have used 2 Million and 500 thousand events respectively. The data set used for both cases are collected using minimum-bias trigger conditions. Minimum-bias trigger events were selected based on the thresholds used on multiplicity and energy from Central Trigger Barrel (CTB) and Zero Degree Calorimeter (ZDC). The analysis of each detector is a part of the full chain used to analyze entire STAR data stream. Broadly, the analysis steps consists of reading the data from acquired data file, applying the detector specific mapping and calibration and then the detector-specific reconstruction e.g, cluster finding, track findings etc.. The analysis of the PMD data involves the following steps:

1. Selection of runs and events for best quality data;
2. Clean up of PMD data;
3. Cell-to-cell gain calibration;
4. Reconstruction of Photon Candidates.

3.5.1 Run Number and Event Selection

For the present analysis, several criteria were used to select events. The conditions used are:

1. Number of readout chains working are largest;
2. All the supermodules were at operating voltage of -1400 V;
3. Run conditions were stable throughout the period;
4. Events with collision vertex less than ±30 cm from the center of TPC along the beam axis;

5. Centrality Selection:

The centrality of the collision is defined by the impact parameter b, smaller the b the more central is the collision. However, we cannot measure the impact parameter directly in the experiments. So, other observables like the uncorrected charged particle multiplicity is used for the centrality selection. The uncorrected charged particles are the primary tracks reconstructed in the pseudorapidity region $\mid \eta \mid < 0.5$. The Figures 3.7 and 3.8 shows the minimum bias distribution of the uncorrected charged particle for various centrality classes for $Au + Au$ and $Cu + Cu$ collisions at midrapidity. Tables 3.1 and 3.2 gives the uncorrected charged particle multiplicity (N_{ch}^{TPC}) from TPC, the number of participating nucleons (N_{part}) and the number of binary collisions (N_{coll}) calculated from the Monte-Carlo Glauber calculations [10] for $Au + Au$ and $Cu + Cu$ collisions.

3.5.2 Clean up of Data

We need to clean the data for the hot channel and noise for low ADC hits. Based on the knowledge that the firing frequency of the hot channels are abnormally large in comparison to normal channels in chain for similar multiplicities. A method based on the hit frequency was used to identify these hot channels. The clean up procedure is a three step process.

1. From large number of events of same centrality selection, we find the hit frequency of each channel hit in all the chains.

2. We find the mean and RMS of this distribution. A channel is called bad if it lies beyond the 5× RMS away from mean of the distribution.

3. After removing these bad channels, mean of the distribution is recalculated and we allow the channels for each chain to pass through the filter again with a cut of $> 6\times$RMS.

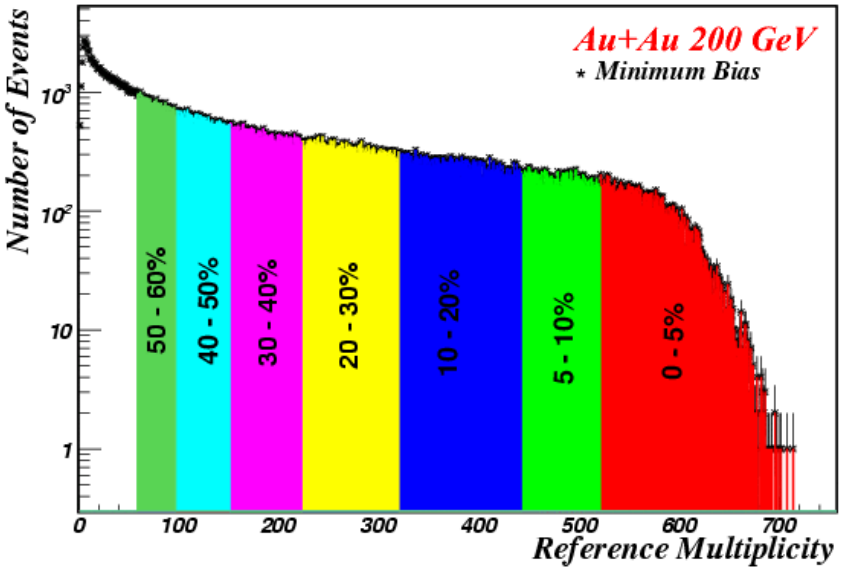

Figure 3.7: *Reference multiplicity for Au+Au at* $\sqrt{s_{NN}}$ *=200 GeV measured as the uncorrected charged particle multiplicities in TPC pseudorapidity* $|\eta| < 0.5$ *region.*

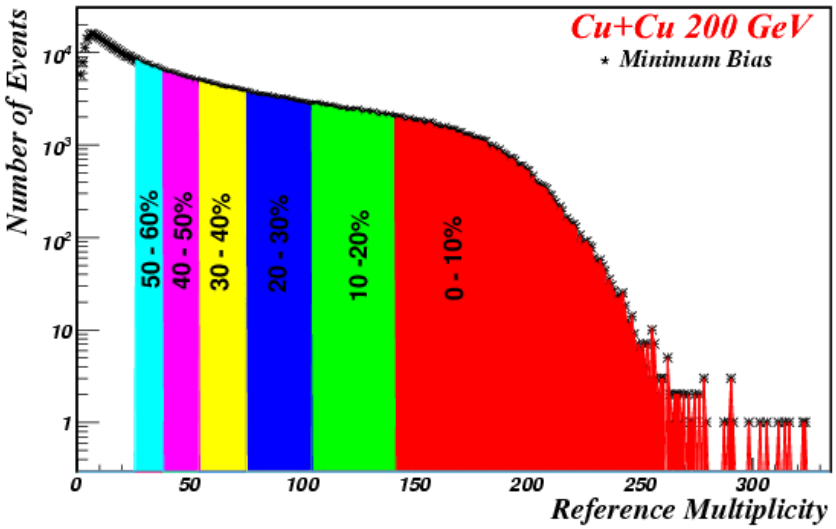

Figure 3.8: *Reference multiplicity for Cu+Cu at* $\sqrt{s_{NN}}$ *=200 GeV measured as the uncorrected charged particle multiplicities in TPC pseudorapidity* $|\eta| < 0.5$ *region.*

Centrality	% of cross section	N_{ch}^{TPC}	$\langle N_{part} \rangle$	$\langle N_{coll} \rangle$
1	$0-5\%$	520	$352.4^{-4.0}_{+3.4}$	$1051.3^{-71.1}_{+71.5}$
2	$5-10\%$	441	$299.3^{-6.7}_{+6.6}$	$827.9^{-66.7}_{+63.9}$
3	$10-20\%$	319	$234.6^{-9.3}_{+8.3}$	$591.3^{-59.9}_{+51.9}$
4	$20-30\%$	222	$166.7^{-10.6}_{+9.0}$	$368.6^{-50.6}_{+41.1}$
5	$30-40\%$	150	$115.5^{-11.2}_{+8.7}$	$220.2^{-38.3}_{+30.0}$
6	$40-50\%$	96	$76.6^{-10.4}_{+8.5}$	$123.4^{-27.3}_{+22.7}$
7	$50-60\%$	57	$47.8^{-9.5}_{+7.6}$	$63.9^{-18.9}_{+14.1}$

Table 3.1: *The calculated values for centrality selection for Au+Au collisions at $\sqrt{s_{NN}}$ = 200 GeV and $\langle N_{part} \rangle$ and $\langle N_{coll} \rangle$ for seven centrality classes. The centrality bins are based on the uncorrected charged particle multiplicities in TPC pseudorapidity $\mid \eta \mid \leq$ 0.5 region. The number of participants and number of binary collisions are calculated from Monte-Carlo Glauber Model Calculations.*

Centrality	% of cross section	N_{ch}^{TPC}	$\langle N_{part} \rangle$	$\langle N_{coll} \rangle$
1	$0-10\%$	139	$99.00^{-1.22}_{+1.47}$	$188.75^{-13.4}_{+15.4}$
2	$10-20\%$	98	$74.55^{-1.04}_{+1.26}$	$123.63^{-8.28}_{+9.40}$
3	$20-30\%$	67	$53.67^{-0.68}_{+0.99}$	$77.64^{-4.72}_{+5.44}$
4	$30-40\%$	46	$37.75^{-0.54}_{+0.66}$	$47.66^{-2.66}_{+2.84}$
5	$40-50\%$	30	$26.24^{-0.35}_{+0.54}$	$29.15^{-5.63}_{+1.64}$
6	$50-60\%$	19	$17.23^{-0.20}_{+0.41}$	$16.82^{-0.69}_{+0.86}$

Table 3.2: *The calculated values for centrality selection for Cu+Cu collisions at $\sqrt{s_{NN}}$ = 200 GeV and $\langle N_{part} \rangle$ and $\langle N_{coll} \rangle$ for six centrality classes. The centrality bins are based on the uncorrected charged particle multiplicities in TPC pseudorapidity $\mid \eta \mid \leq$ 0.5 region. The number of participants and number of binary collisions are calculated from Monte-Carlo Glauber Model Calculations.*

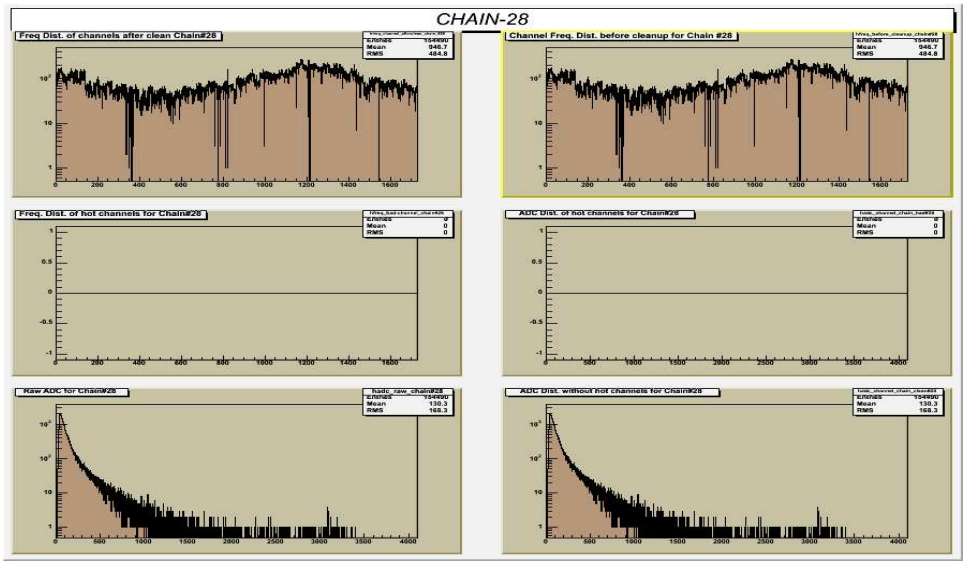

Figure 3.9: *From Top First row : Frequency of Channel hit in chain no. 28 before and after clean up. Second row is for the channels needs to be removed. and the* 3^{rd} *row is the ADC chain spectra for chain no. 28 before and after cleanup.*

Figure 3.9 shows the ADC spectra for a clean chain and the frequency of the hit channel before and after the clean up.

3.5.3 Cell-to-Cell Gain Calibration

Each cell of PMD is a proportional counter and a variation in the gain of each cell by $10 - 30\%$ is expected throughout the dectector for various reasons including mechanical construction, fluctuations in the primary ionization and secondary multiplication, response of front end electronics etc. Variation in gain is also observed in the SM to SM as each super module is a separate gas tight enclosure with separate high voltage applied to it. The aim of the calibration is to calculate the relative gain of each cell and get the uniform response of the overall detector. The gain is determined by the response of the minimum ionizing particle (MIP) of each cell. Since the MIP gives signal only on one cell, so we search for the isolated cells in each supermodule and calibration is

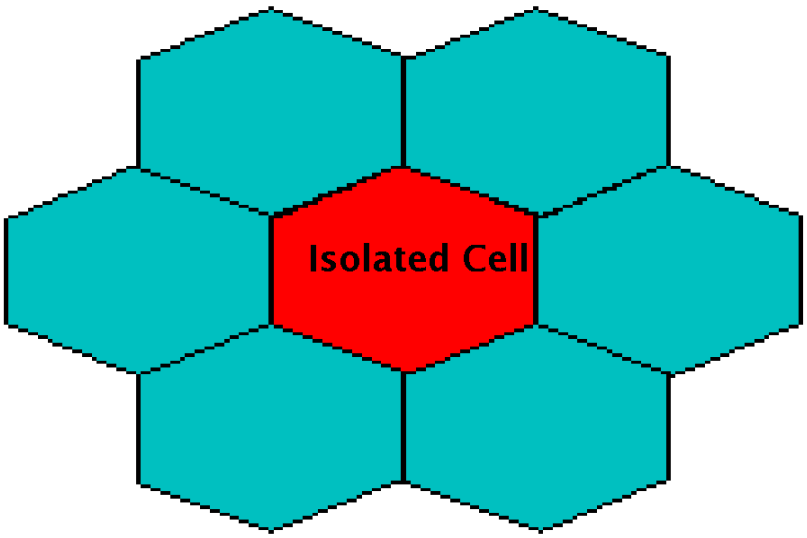

Figure 3.10: *Schematic diagram of an isolated cell shown in (red color) with six neighbouring cells with zero ADC*

done SM-wise. A cell is called isolated if that has a non zero ADC value but all of its six neighbors have zero signal. The search for isolated cell is performed over all events. Figure 3.10 shows the schematic diagram of one isolated cell which has six neighbours with zero ADC.

The ADC spectra of isolated cell is shown in the Figure 3.11 fitted with Landau function. The mean value after fitting ADC spectra of isolated cell up to 500 channels with the Landau function is taken as the MIP response for particular cell. Table 3.3 shows the average MIP values for different SMs. These MIPs are later used as a discrimination threshold for hadrons and photons. For calibration, mean of all isolated cell ADC (global mean) distributions for each cell in chain is obtained. Then the ratio of the global mean to the mean of each isolated cell ADC distribution, called the calibration factor, is obtained. Overall gain calibration is obtained in two steps:

(a) Uniformity in all cells in chain.

(b) Chain to Chain variation in SM.

S.No.	Supermodule No.	MIP in Cu+Cu Collisions	MIP in Au+Au Collisions
1	0	94.88	110.31
2	1	27.91	135.57
2	2	55.66	0.0
4	3	58.79	72.13
5	4	75.78	73.4
6	5	30.69	128.38
7	6	98.48	111.17
8	7	105.4	96.8
9	8	83.34	82.65
10	9	58.91	60.46
11	10	194.4	88.67
12	11	127.6	140.52

Table 3.3: *Table showing the MIP value for each supermodule on PMD for Au+Au and Cu+Cu collisions at* $\sqrt{s_{NN}}$ *=200 GeV.*

The different panels of Figure 3.12 shows the gain factors of each SM, Most Probable Value (MPV), Mean, content of isolated cell, content Vs. mean, and mean Vs MPV. It is found that mean and MPV are well correlated and the content Vs. mean spectra shows the stability of mean which does not depend on statistics. Each cell, for all events, is then calibrated by this factor to have a uniform response throughout the SM.

3.5.4 Reconstruction of Photons

After the calibration of the data as discussed in the previous section, we need to collect cells to find clusters. Photons deposit energy in a large number of cells on preshower plane after interaction with lead converter. One needs to add the signals obtained from the associated cells of cluster to obtain photon like clusters. Two steps are involved in

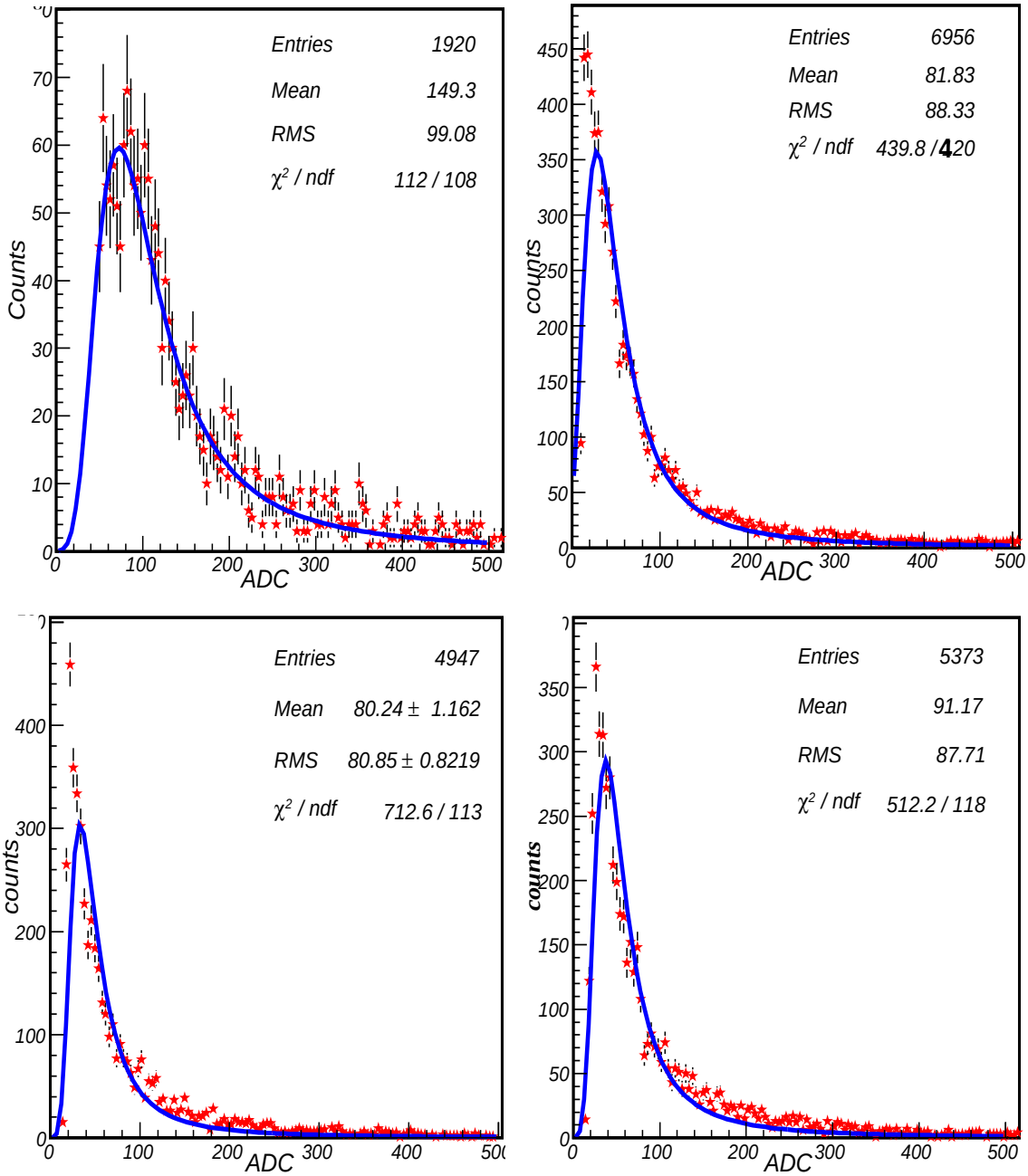

Figure 3.11: *ADC spectra of isolated cells in different SM's.*

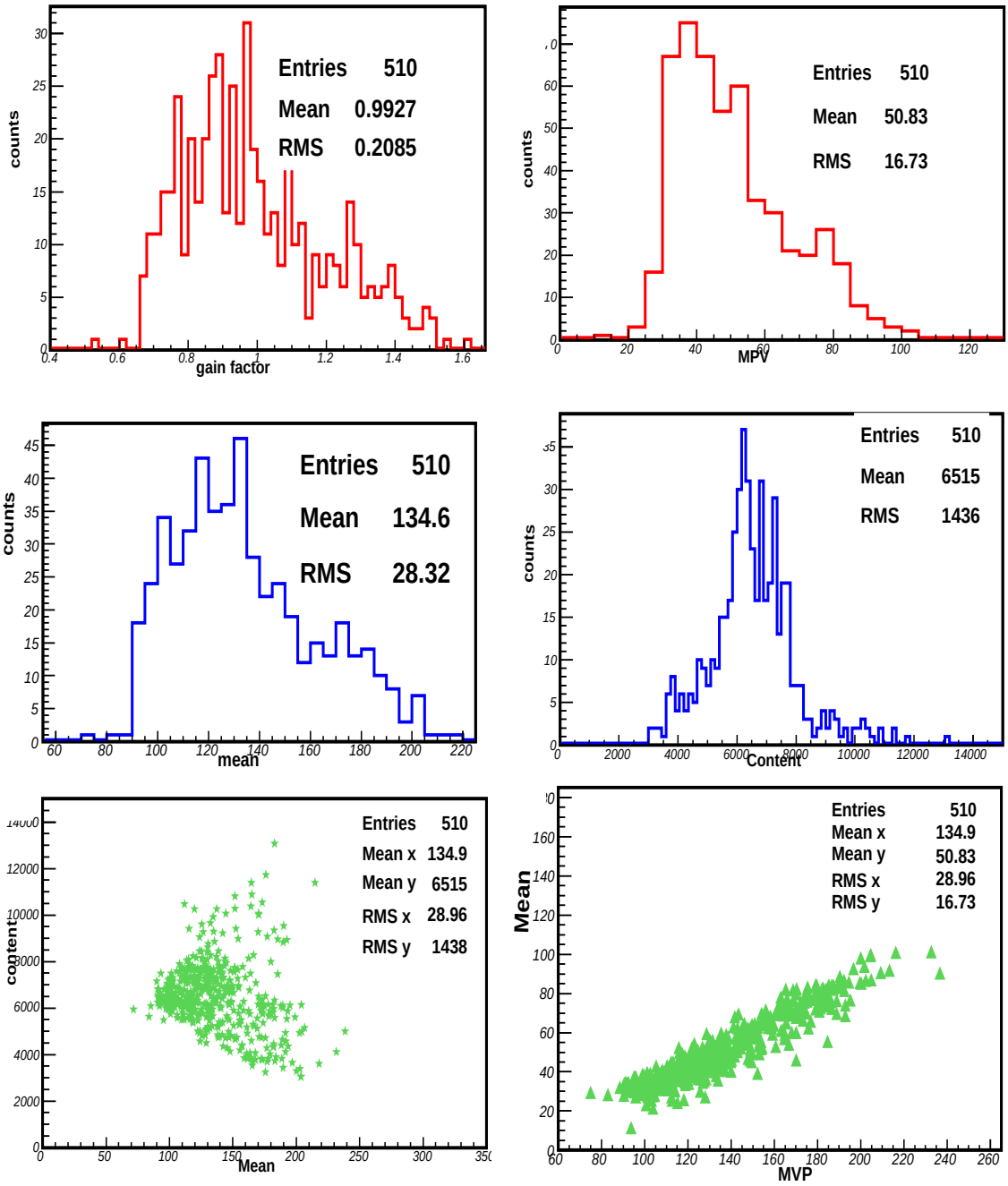

Figure 3.12: Gain factors, MPV, Mean, Content, Content Vs. Mean, Mean Vs. MPV for a SM-chain combination.

finding clusters:

(a) Crude Clustering;

(b) Breaking Superclusters into smaller clusters.

Crude Clustering

In heavy ion collisions, multiplicity is very high and simple procedure of clustering will result in overlapping clusters. In such case one constructs the superclusters which are contiguous cells with nonzero ADC values. The energy deposited in each cell is arranged in the descending order. The superclusters are formed by taking the cell having the largest energy deposition and collecting all cells contiguous to it. This process is repeated with decreasing order of energy till all cells are exhausted. Thus the data in each SM is broken into several superclusters separated with the cells having zero energy deposition

Breaking Superclusters into Smaller Clusters

In large multiplicity events the clusters produced by each particle may overlap, thus giving rise to large superclusters. If the cluster consists of one cell, the center of the cell is identified as the center of cluster and the strength of the cluster is the energy deposited in the cell. For two cell clusters, the center of the cluster is defined as the center of gravity of two cells and the strength is defined as the sum of the energy deposited in two cells. For superclusters having more than two cells one needs to break the supercluster. Each supercluster with more than two cells may have more than one maxima. To split the supercluster, the next nearest neighbour (which is at distance of $\sqrt{3}$ cell units) must have an energy deposition greater than 25% to be considered as cluster center in addition to the third nearest (which is at a distance of 2 cell units) must have an energy deposition greater than 10 % of the peak energy deposition value.

After calculating the possible center of clusters and assuming that each cluster has Gaussian shape, a minimization procedure is adopted to find the position and strength

of the clusters. A cell belongs to the cluster nearest to it. If two or more clusters are at about same distance from the cell, it is shared between these clusters. The fraction of the cell going to each cluster is proportional to the strength of that cluster. The fraction of ADC of a cell contributing to a cluster is proportional to the strength of that cluster. The strength of a cluster is sum total of strength of cells belonging to it (fractional energy deposited if the cell belongs to more than one cluster). The output of the above clustering procedure are : X position, Y position, η, ϕ, number of cells in a cluster, and the energy deposition (ADC) of the clusters.

3.5.5 Discrimination of Photon from Hadron Clusters

The PMD has two planes, veto plane and preshower plane. Photon does not give signal on the veto plane but produce signal on the preshower plane after producing the electromagnetic shower with lead converter. Hadrons on the other hand, mostly give signals on single cell on both veto and preshower planes. There is also finite probability that few hadrons can also generate shower giving signal on preshower plane because of hadronic interaction cross section of lead. After detailed simulation to keep optimum value of efficiency and purity we use the threshold of 3×MIP ADC and number of cells greater than 1. These conditions are used to discriminate hadron and photon clusters. Figures 3.13 and 3.14 show the uncorrected multiplicity distribution of photon-like clusters for $Au + Au$ and $Cu + Cu$ collisions at $\sqrt{s_{NN}}$ =200 GeV in forward rapidity.

3.5.6 Event Generators

It is expected that hard or semihard parton scatterings with transverse momentum of a few GeV are expected to dominate high energy heavy ion collisions. HIJING (Heavy Ion Jet INteraction Generator) [11] Monte Carlo model was developed by M. Gyulassy and X.-N. Wang with special emphasis on the role of minijets in $p + p$, $p + A$ and

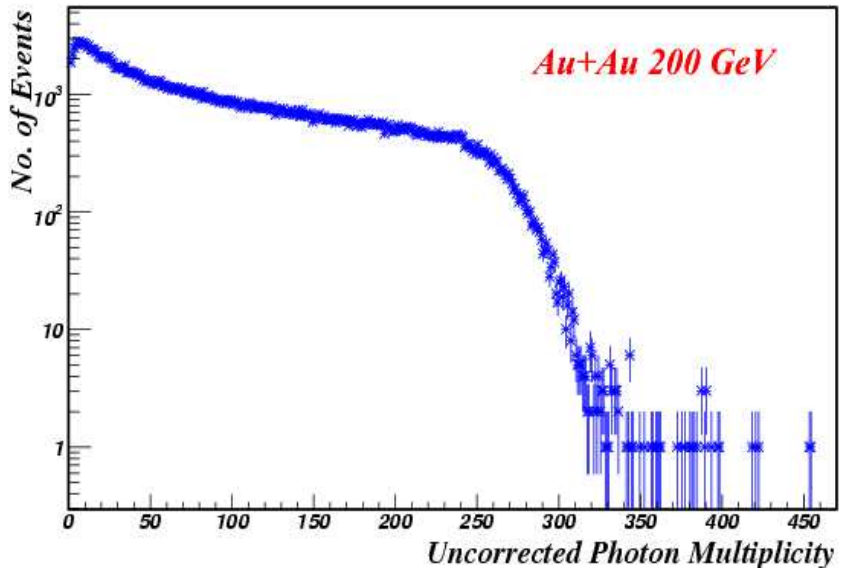

Figure 3.13: *Uncorrected minimum bias photon like ($N_{\gamma like}$) multiplicity distribution for Au+Au collisions $\sqrt{s_{NN}}$ =200 GeV in forward rapidity.*

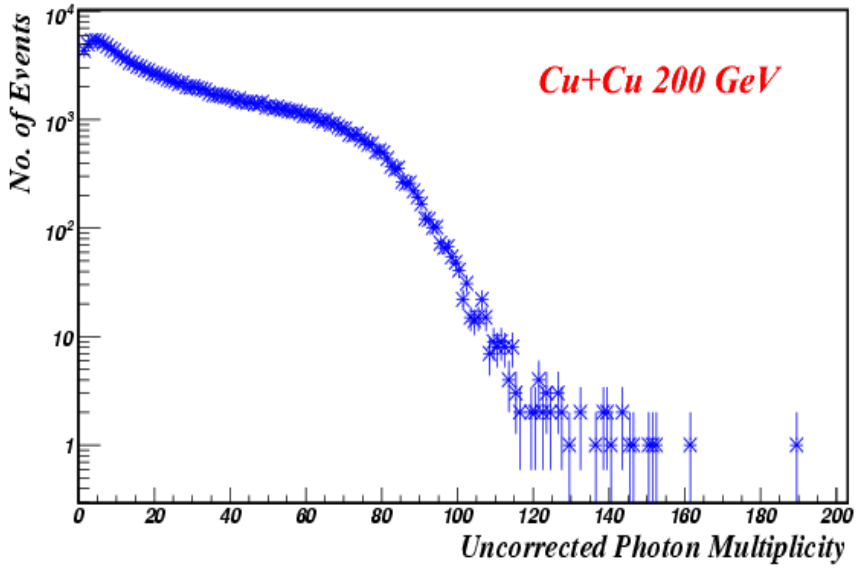

Figure 3.14: *Uncorrected minimum bias photon like ($N_{\gamma like}$) multiplicity distribution for Cu+Cu collisions $\sqrt{s_{NN}}$ =200 GeV in forward rapidity.*

$A + A$ reactions at collider energies. HIJING is the most widely used event generator for heavy ion collisions at RHIC energies. The HIJING model is a microscopic model that combines perturbative QCD inspired models for multiple jet production with phenomenological string models for soft particle production. Glauber geometry for multiple collisions is used to describe the impact parameter dependence of the number of inelastic processes. Baryon transport is performed via the diquark conserving and the diquark breaking mechanism. Jet quenching is introduced by energy loss in the dense medium created in the collision. The HIJING event generator was developed to extrapolate hadron-hadron multi-particle soft plus hard phenomenology as encoded in the LUND JETSET/PYTHIA model [12] of nuclear collisions. One important feature of HIJING is that it can account for the pion quenching component of the baryon anomaly.

3.6 Simulation Results

We try to understand the behavior of the detector by rigorous evaluation techniques used in heavy ion collisions which can be met by simulating the detector and its physical effects. While simulation is necessary, it is not sufficient. We, therefore, present an outline of an evaluation methodology that is being used in simulation in STAR experiment with an emphasis on PMD simulation.

3.6.1 PMD Geometry in GEANT

GSTAR is a framework to run STAR detector simulation using GEANT3 simulation package. The GSTAR package consists of a set of modules, which provides the description of the geometry for different subsystems of the STAR experiment. The PMD geometry has been implemented in the GSTAR framework. To simplify the implementation of the SM designs in STAR, the total number of modules on each plane is 17 compared to actual 12. This is shown in the Figure 3.15

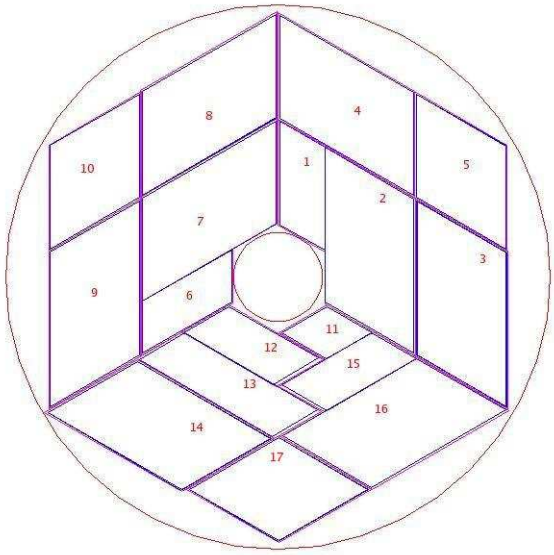

Figure 3.15: *Geometry of PMD in GSTAR with pseudorapidity* $-3.7 < \eta < -2.3$ *and full azimuthal coverage*

PMD Geometry is divided into three sectors with sector 1 and 2 divided into 5 volumes each and sector 3 divided into 7 volumes. Each volume is filled with air and an aluminum (Al) frame is placed inside each volume which corresponds to the outer frame of the SMs. For each SM, a PCB board of 1.7mm thickness is placed at the first layer of the PCB chamber. The next layer of the material corresponds to active volume made of gas filled array of detectors. The material in each SM is broken up into rows of strips in air which are then filled with hexagonal cells of Cu. The volume is then filled with a mixture of Ar and CO_2 in the ratio of 70 : 30 respectively. Another layer of of PCB material is placed. After we place the Pb plane, we place a Stainless Steel (SS) plane on top of it. We then we put the the Al frame. The preshower plane is included in the similar way as is done for CPV plane but here the FEE plane is placed at the end.

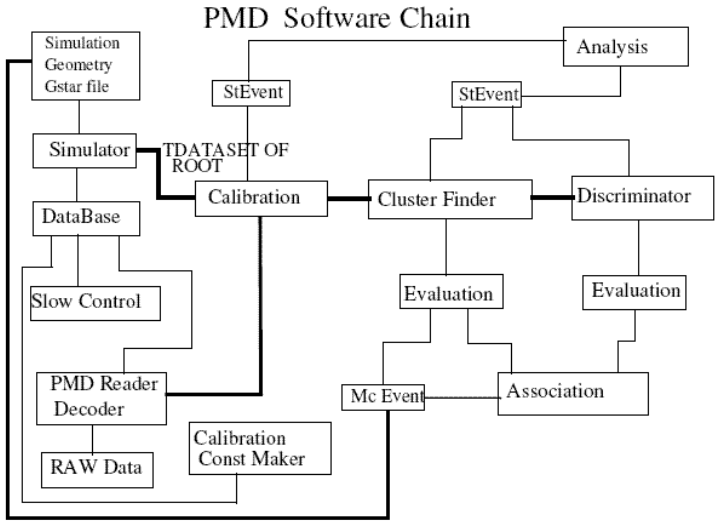

Figure 3.16: *Flow-chart for reconstruction of PMD data from simulation as well as from raw data.*

3.6.2 Generation of Simulated Data

The various steps starting from the event generation to the reconstruction along with the GEANT simulation are shown in the flow chart given in the Figure 3.16. This flow chart include the GEANT simulation and the chain used for reconstruction, which is called a Big Full Chain (BFC). Events generated from the HIJING event generator are passed through the GSTAR. These events are then reconstructed using the BFC. At various levels of reconstruction, the data sets are stored in accordance with STAR event model (StEvent). For PMD we store hits and cluster information in StEvent.

3.6.3 Photon Conversion Efficiency

As mentioned earlier, photon produces the electromagnetic shower after passing through the lead converter and deposits energy in cluster of PMD cells. For low energy incident photon, all its energy is lost in the converter with out giving signal on the sensitive

medium and if the energy is high enough, the photons get converted into shower and give signals on the preshower plane. The photon conversion efficiency is thus defined as the ratio of the number of photons getting converted into shower giving signal on the preshower plane to the number of incident photons. As shown in the Figure 3.17, the conversion efficiency for photons with energy 200 MeV has value about 70% and increase upto 90% for photons with energy $>$ 1 GeV and above 1 GeV, the conversion efficiency becomes independent of the incident energy.

3.6.4 Material Effect on Photon Counting

Due to the upstream materials the photon undergo a conversion and scattering because of the large deflection. This affects the photon counting efficiency and purity of photon sample. The upstream material is described in terms of change in the occupancy, multihit probability, deviations of incoming particles. The distribution of $\delta\eta$ ($\eta_{clus} - \eta_{orig}$) and $\delta\phi$ ($\phi_{clus} - \phi_{orig}$) for the PMD only and for PMD in presence of all detectors in STAR experiment are shown in the Figure 3.18.

3.6.5 Percentage of Clusters on PMD

There is a definite probability that charged hadrons can also give the signal on the preshower plane of PMD and the conversion of upstream material will generate background to the detected photons. There is also a fraction of the photon like cluster generated due to the splitting of the clusters of photon (The details of which is discussed in section 3.5.4). Figure 3.19 shows the percentage of the clusters on the preshower plane as function of the centrality.

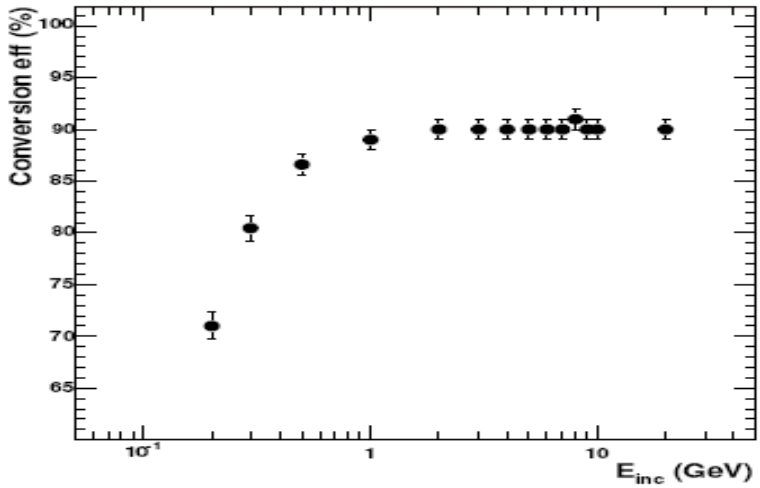

Figure 3.17: *Conversion efficiency as a function of energy of incident photon.*

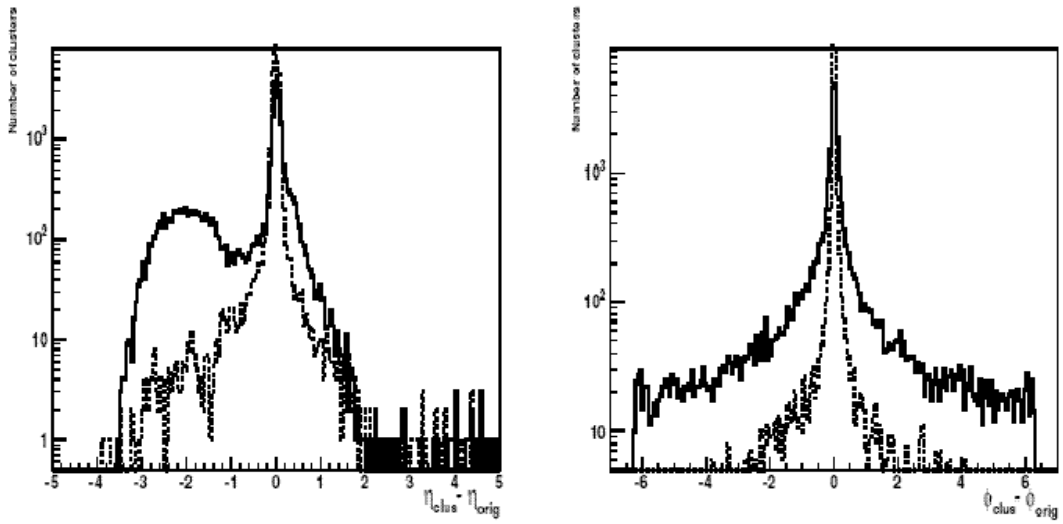

Figure 3.18: *$\delta\eta$ ($\eta_{clus} - \eta_{orig}$) and $\delta\phi$ ($\phi_{clus} - \phi_{orig}$) for PMD only (dotted line) and PMD in presence of all detectors (solid line).*

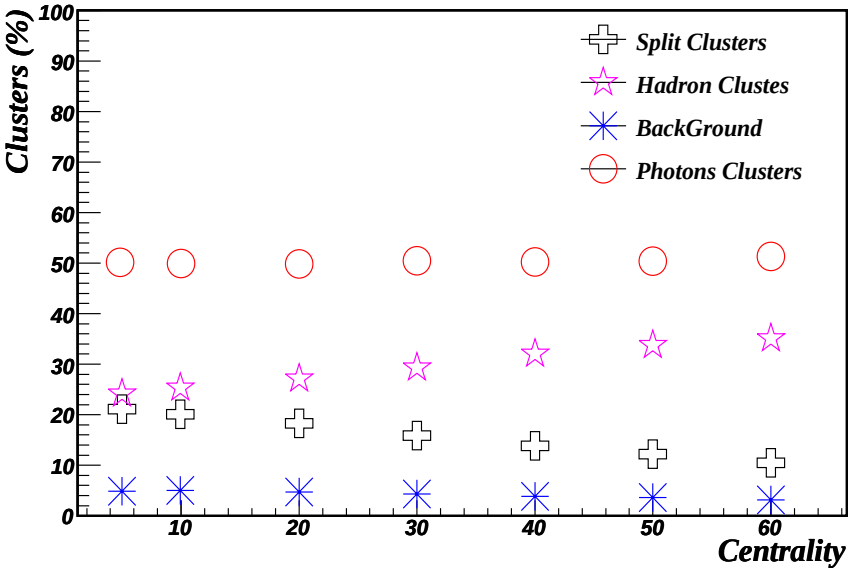

Figure 3.19: *Percentage of γ_{like}, background, split and hadron clusters as function of centrality.*

3.6.6 Efficiency and Purity of Photon Counting

Photons are counted by clustering the hits in the experimental data. The estimation of efficiency and purity of photon counting is made using simulated data. On average, there is a 90% probability for photons to shower in the lead converter and produce large signals. Compared to this, hadrons give a signal mostly corresponding to minimum ionizing particles (MIP). The majority of the hadrons are rejected by applying a suitable threshold on cluster signal. A fraction of hadrons undergoing interaction in the lead converter produce signals larger than the threshold and appear as contaminants in the photon sample. The number of clusters remaining above the hadron rejection threshold is termed as γ-like. The photon counting efficiency is defined as the number of photons detected above certain threshold (energy deposited and/or number of cells) to the number of photons incident from the vertex in our detector coverage and purity of the photon sample is defined as the number of photons detected above certain threshold

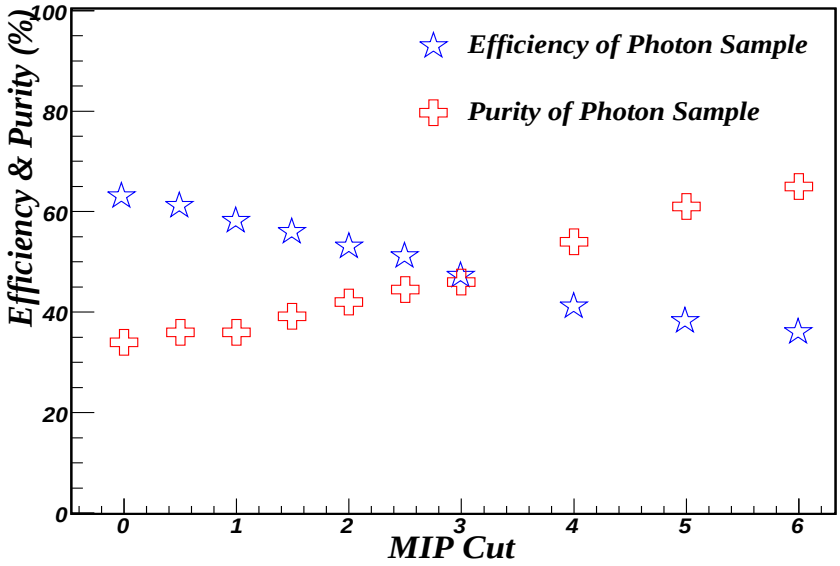

Figure 3.20: *MIP optimization*

(energy deposited and/or number of cells) to the number of clusters detected in the detector above the same threshold.

$$\epsilon_\gamma = N_{cls}^{\gamma,th}/N_{inc}^{\gamma} \tag{3.1}$$

$$f_p = N_{cls}^{\gamma,th}/N_{\gamma-like} \tag{3.2}$$

where ϵ_γ is the photon counting efficiency and f_p is the fractional purity of the photon sample. N_{inc}^{γ} is the number of incident photons on the PMD and $N_{cls}^{\gamma,th}$ is the number of photon clusters above the threshold. Both ϵ_γ and f_p are determined by a detailed Monte Carlo simulation using the HIJING event generator. Figure 3.20 shows the photon counting efficiency and the purity as a function of hadron rejection threshold (in MIP units). The photon counting efficiency decreases with increasing threshold but purity improves significantly with increasing threshold only up to $3 \times MIPs$ and then rather slowly at higher thresholds for minimum bias events.

From the experimental data one determines $N_\gamma - like$, the number of clusters above the hadron rejection threshold. Using the estimated values of ϵ_γ and f_p one obtains the

number of photons incident on the detector in the event from the relation:

$$N_{\gamma} = N_{\gamma-like} * \epsilon_{\gamma}/f_p \tag{3.3}$$

$N_{\gamma-like}$ is obtained from the data by applying an optimal value of the threshold on the energy cut on the clusters. The threshold value is determined in terms of MIP energy units and is discussed in section 3.5.3. Figures 3.21, 3.22, 3.23 and 3.24 shows the ϵ_{γ} and f_p values as a function of pseudorapidity (η) and centrality for the $Au + Au$ and $Cu + Cu$ collisions at $\sqrt{s_{_{NN}}}$ =200 GeV using the 3 MIP and number of cells in a photon like cluster is greater than 1 for photon -hadron discrimination cut. The efficiency values are found to be smaller at lower η values, away from the beam pipe and there is only a little dependence on centrality of the collisions while the purity is almost constant in η region and is similar for all centralities.

3.6.7 Acceptance Correction

The PMD covers a pseudorapidity range of $-3.7 \leq \eta \leq -2.3$ with full azimuthal coverage at a distance of 540 cm from the interaction point. The distribution of X-Y of PMD is shown in the Figure 3.25 with all supermodules boundaries. Due to the non-functionality of a few supermodules, PMD coverage is less than 100%. The loss of acceptance comes from the following:

1. Dead area in SM boundaries;
2. Inactive cells;
3. Missing readout boards;
4. Hot channels which are taken out during cleanup.

A gain table is made from the cell-to-cell gain corrections. This table gives the identification of cells which are active. Each cell is identified with supermodule, row and

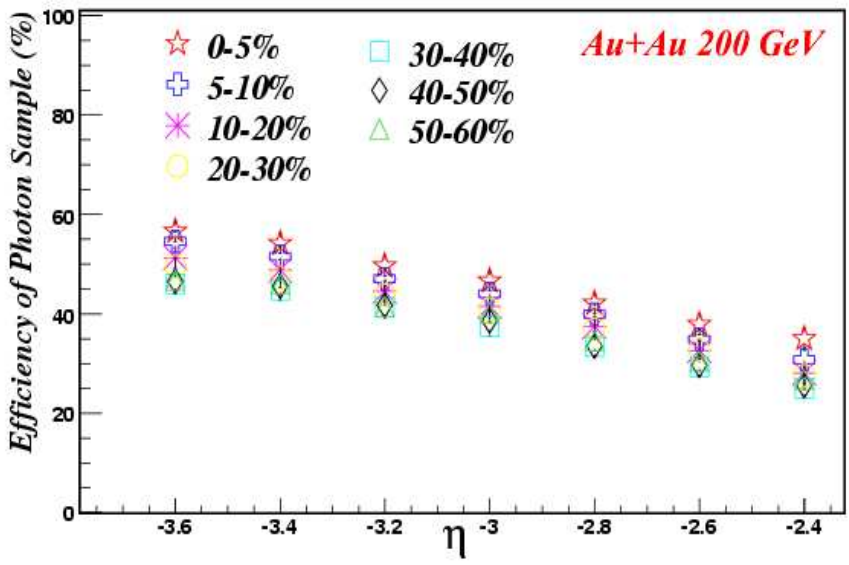

Figure 3.21: *Photon counting Efficiency (ϵ_γ) for PMD as a function of pseudorapidity (η) and centrality from top central to peripheral events in Au+Au collisions at $\sqrt{s_{NN}}$ = 200 GeV*

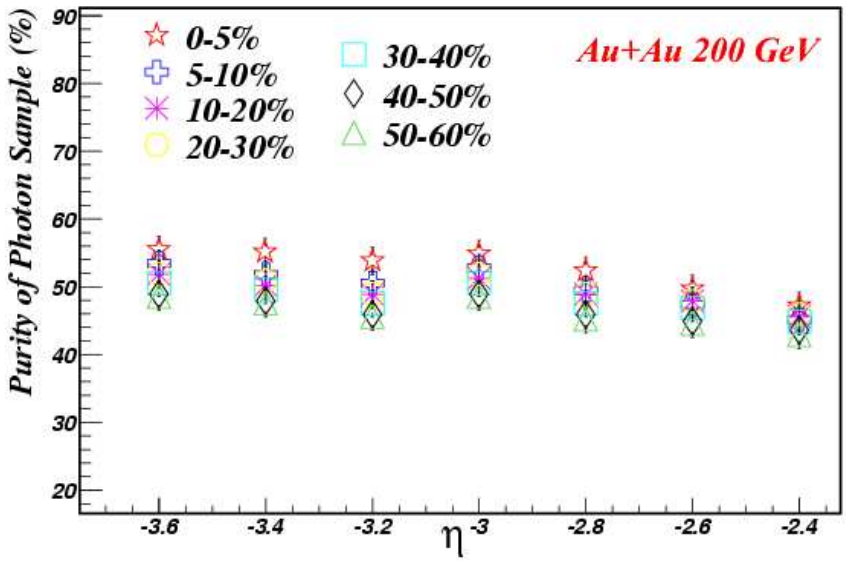

Figure 3.22: *Purity (f_p) of photon sample for PMD as a function of pseudorapidity (η) and centrality from top central to peripheral events in Au+Au collisions at $\sqrt{s_{NN}}$ = 200 GeV*

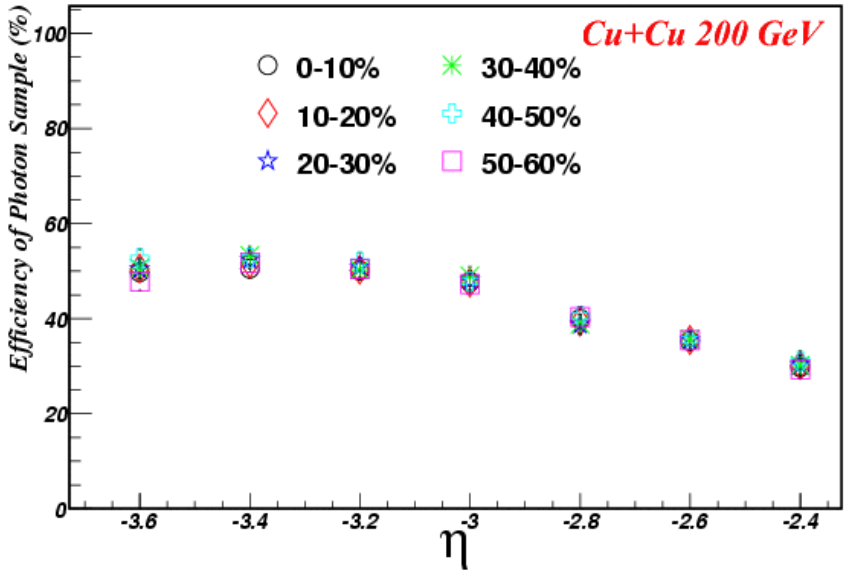

Figure 3.23: *Photon counting Efficiency (ϵ_γ) for PMD as a function of pseudorapidity (η) and centrality from top central to peripheral events in Cu+Cu collisions at $\sqrt{s_{NN}}$ = 200 GeV*

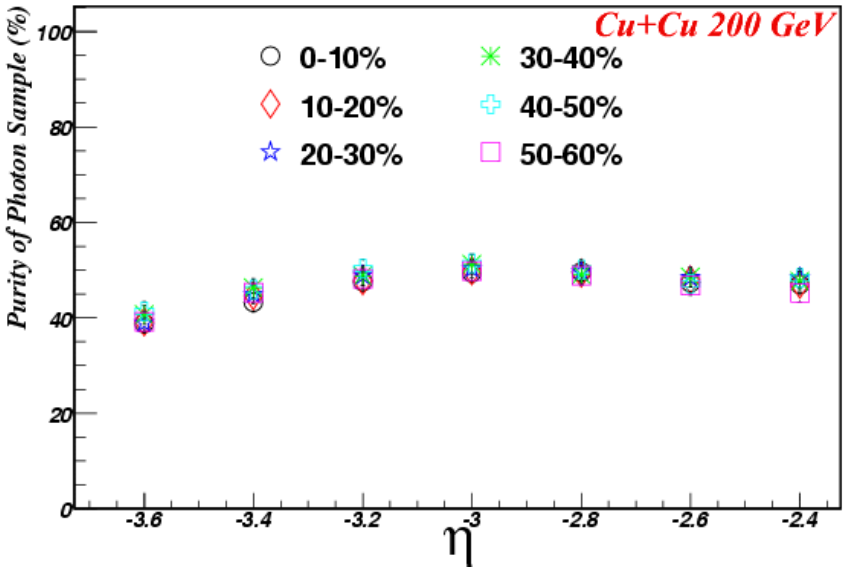

Figure 3.24: *Purity (f_p) of photon sample for PMD as a function of pseudorapidity (η) and centrality from top central to peripheral events in Cu+Cu collisions at $\sqrt{s_{NN}}$ = 200 GeV*

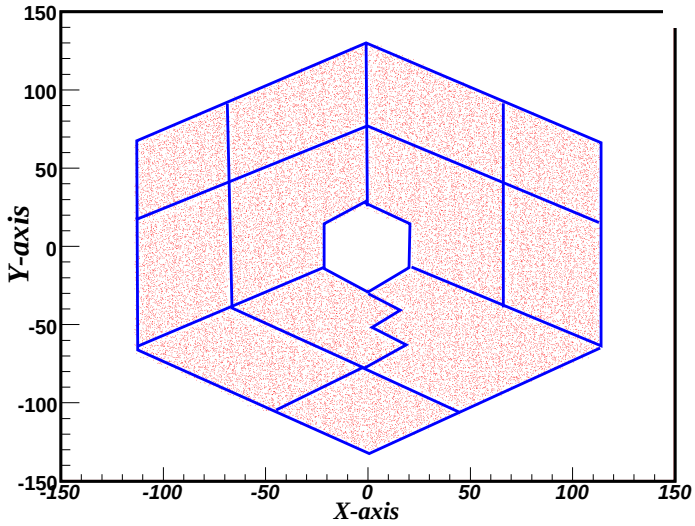

Figure 3.25: *X-Y display of PMD is shown with the boundaries of the each supermodule with blue lines.*

column. Thus the gain table has the list of LIVE or ACTIVE cells. Using the gain table and corresponding mapping information, one can get η values of the active cells and from there find out if the cell falls within the η ring. Knowing the number of cells falling within the η ring and the area of each cell one gets the area of the active cells within the eta ring. Active area within the cell = (number of cells within the ring $\times$ area of each cell) / (area of the ring). The acceptance correction factor is inverse of the above number and is shown in the Figures 3.26 and 3.27 for $Au + Au$ and $Cu + Cu$ collisions respectively.

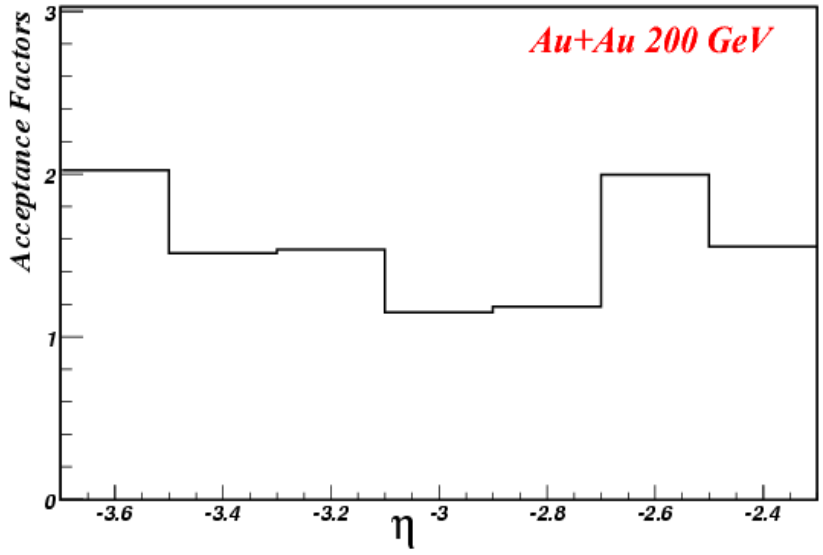

Figure 3.26: *Variation of acceptance factors as function of pseudorapidity for Au+Au collisions at* $\sqrt{s_{NN}}$ *=200 GeV*

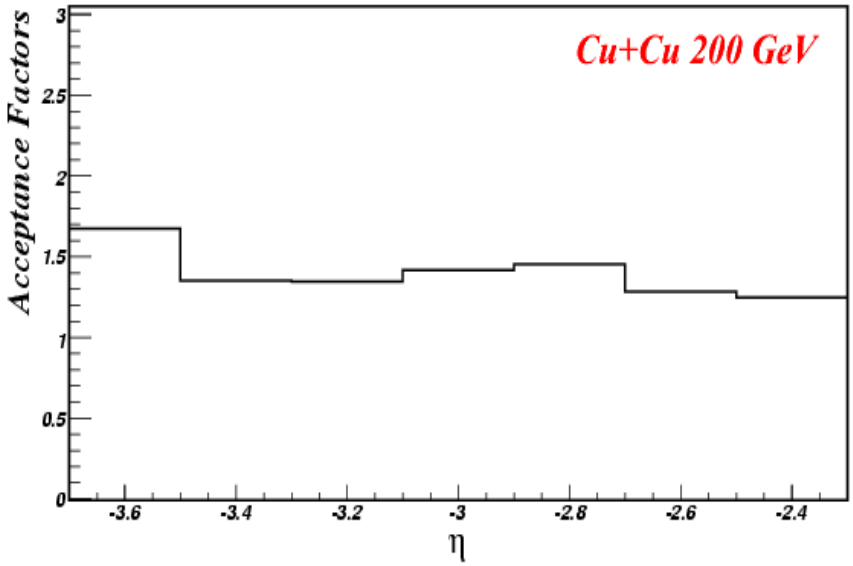

Figure 3.27: *Variation of acceptance factors as function of pseudorapidity for Cu+Cu collisions at* $\sqrt{s_{NN}}$ *=200 GeV*

3.7 Charged Particle Multiplicity

The analysis of data from the Forward Time Projection Chambers involves the following steps:

1. **Event Selection** The Events are selected with the collision vertex less than 30 cm from the center of the time projection chamber (TPC) along the beam axis.

2. **Pad-to-Pad Calibration** The calibration of the FTPC is done using the LASER calibration system [13]. This system helps to calibrate the drift velocity in the non uniform radial drift field and also provides information for corrections to spatial distortions caused by mechanical or drift field imperfections. The localization of dead pads is done by the pulser and by analysis of the data to identify electronically noisy pads [14]. Each cell, for all events, is then calibrated by this factor to have a uniform response throughout the SM.

3. **Reconstruction of Charged Tracks and Track Quality Cuts** The reconstruction of the charged tracks is done by finding the track points from the charge distribution detected by the pads details of which are discussed in section 2.3. A track is considered as valid if it consists of at least 5 found clusters which ensures small contribution of split tracks and if its distance of closest approach (DCA) is less than 3cm. The background contamination primarily from γ conversion is reduced when we use tracks with $0.1 < p_T < 3.0$ GeV/c. Figures 3.28 and 3.29 shows the minimum bias distribution of the charged particle multiplicity for $Au+Au$ and $Cu+Cu$ collisions at $\sqrt{s_{NN}}$ =200 GeV respectively.

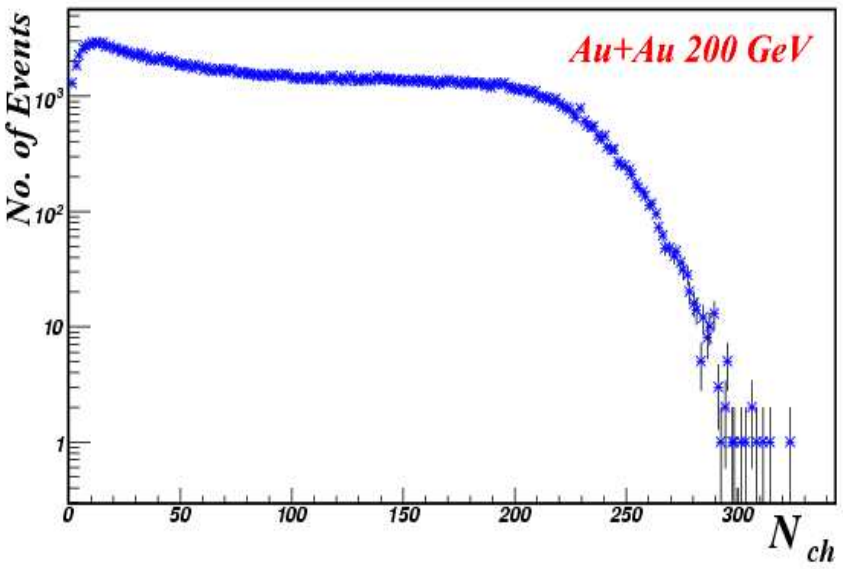

Figure 3.28: *Minimum biased charged particle multiplicity distribution at forward rapidity for Au+Au collisions at* $\sqrt{s_{NN}}$ *=200 GeV*

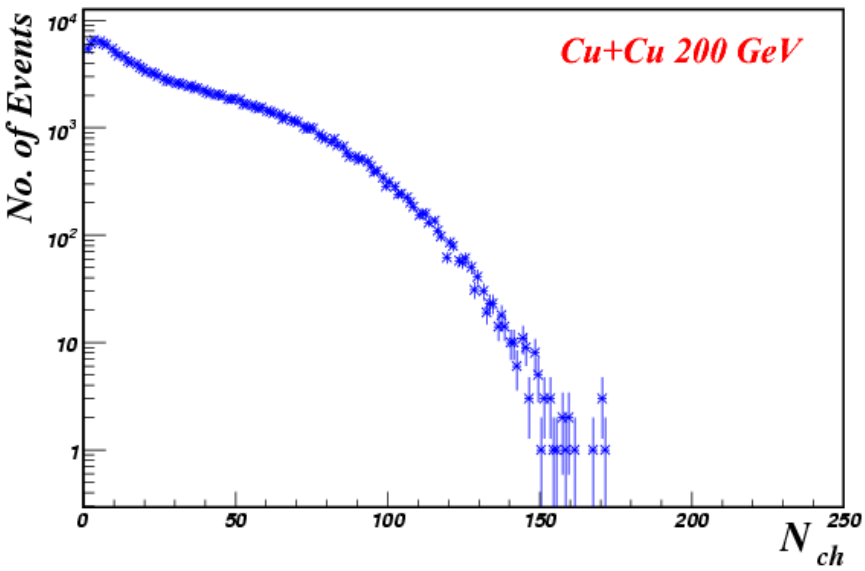

Figure 3.29: *Minimum biased charged particle multiplicity distribution at forward rapidity for Cu+Cu collisions at* $\sqrt{s_{NN}}$ *=200 GeV*

3.8 N_γ Correlations with other Detectors

Multiplicity of photons is expected to be correlated or anti-correlated with information from other detectors in STAR. The correlation of photon multiplicity and the charged particle at forward rapidity with the reference multiplicity i.e, the uncorrected charged particle multiplicity at midrapidity is shown in the Figures 3.30 and 3.31. The correlations show that the photon multiplicity and the charged particle multiplicity at forward rapidity increases with the increase in the charged particle multiplicity at midrapidity. Figures 3.32 and 3.33 show the correlations for the charged particle multiplicity with photon multiplicity at forward rapidity for different centralities for $Cu+Cu$ and $Au+Au$ collisions respectively at $\sqrt{s_{NN}}$ =200 GeV. At all centralities the photon multiplicity increases with the increase in the charged particle multiplicity.

The correlations of the photon multiplicity with the trigger detectors i.e, with CTB and ZDC are shown in the Figures 3.34 and 3.35 respectively for $Au + Au$ collisions at $\sqrt{s_{NN}}$ =200 GeV. The CTB measures the charged particles in the midrapidity and is correlated with photon multiplicity. The correspondence with ZDC shows the multiplicity of photon decreases as the collision centrality increases, indicating an anti-correlation.

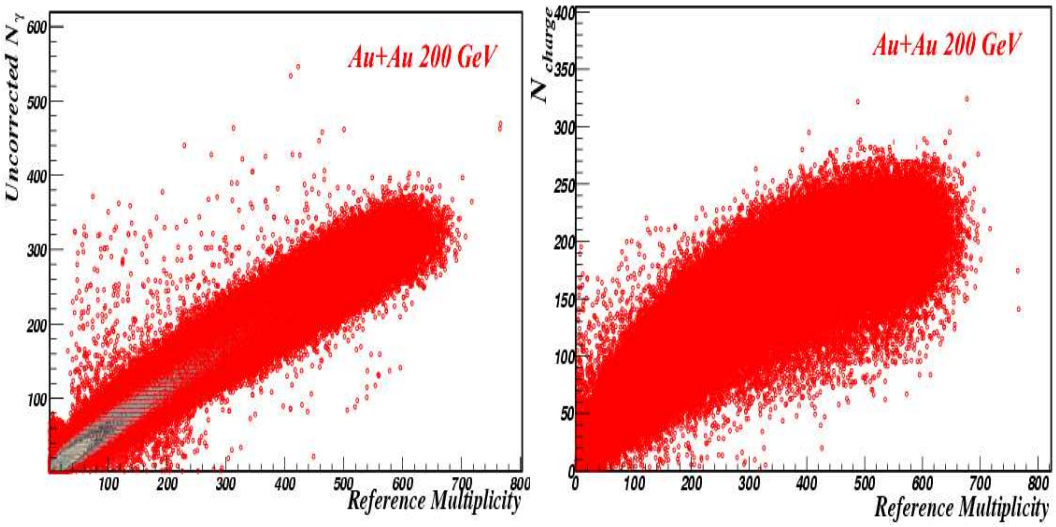

Figure 3.30: *Correlation of uncorrected N_{gamma} and N_{Charge} for Au+Au collisions at $\sqrt{s_{NN}}$ = 200 GeV in the forward rapidity with Reference Multiplicity.*

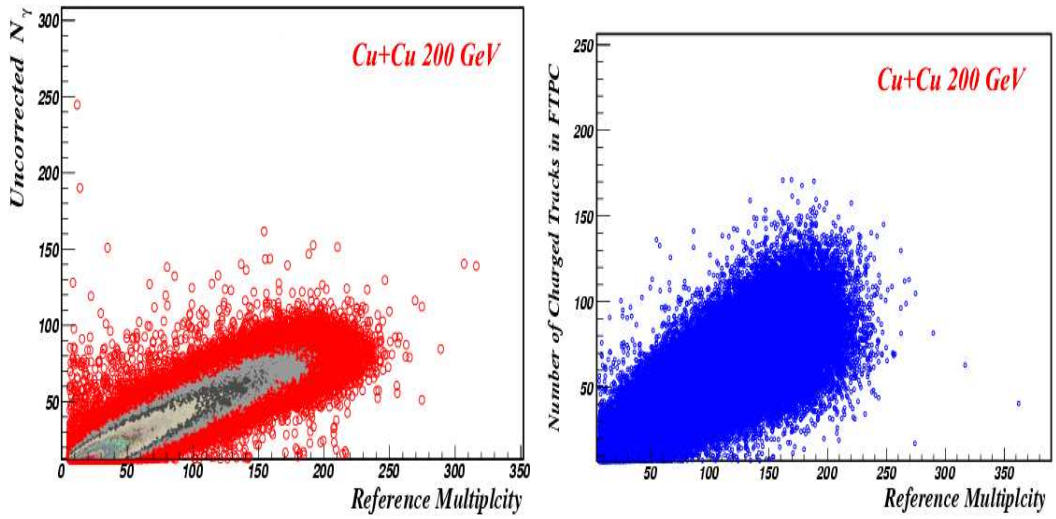

Figure 3.31: *Correlation of uncorrected N_{gamma} and N_{Charge} for Cu+Cu collisions at $\sqrt{s_{NN}}$ = 200 GeV in the forward rapidity with Reference Multiplicity.*

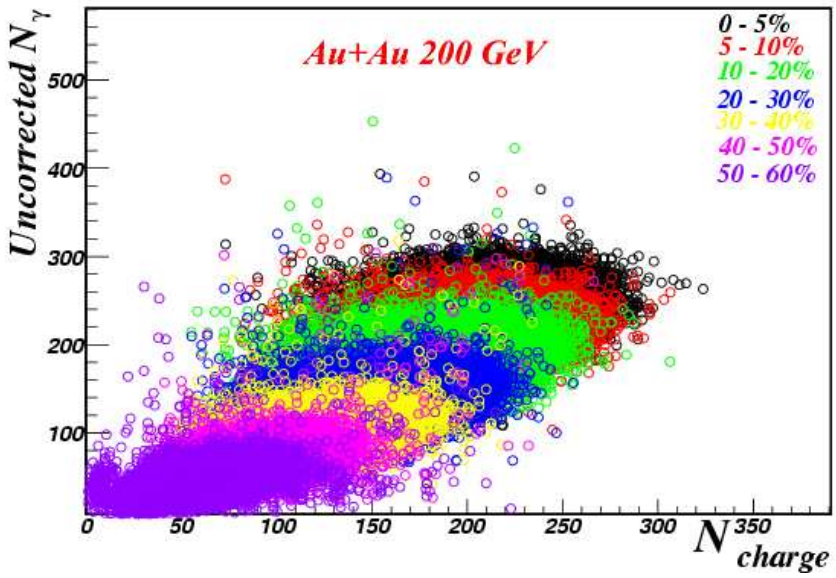

Figure 3.32: *Correlation of uncorrected N_{gamma} with N_{Charge} for Au+Au collisions at $\sqrt{s_{NN}}$ = 200 GeV in the forward rapidity. The different colors shown are for different centrality bins.*

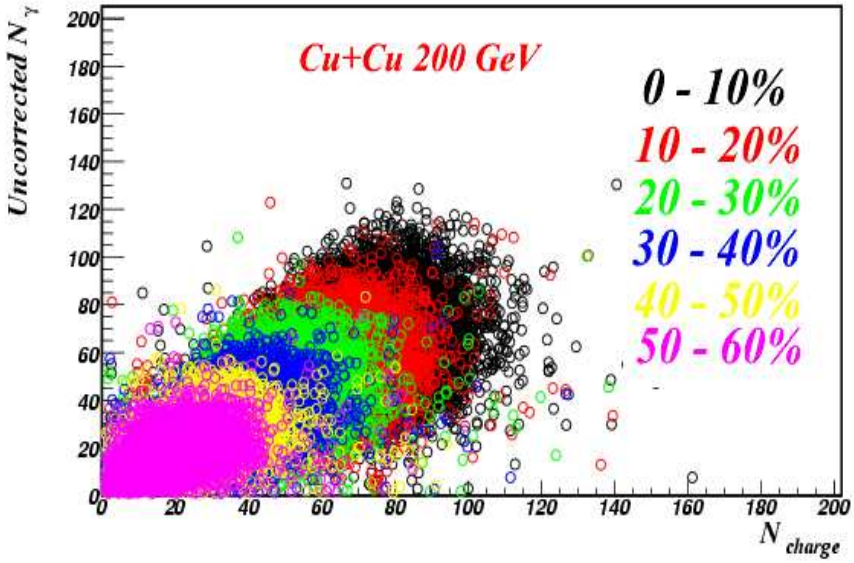

Figure 3.33: *Correlation of uncorrected N_{gamma} with N_{Charge} for Cu+Cu collisions at $\sqrt{s_{NN}}$ = 200 GeV in the forward rapidity. The different colors shown are for different centrality bins.*

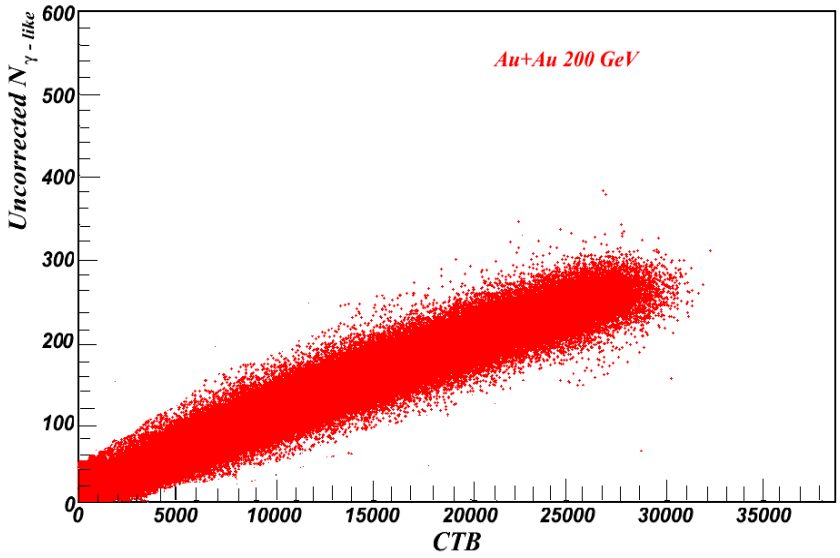

Figure 3.34: *Correlation of uncorrected $N_{\gamma-like}$ with CTB in Au+Au Collisions at $\sqrt{s_{NN}}$ = at 200 GeV.*

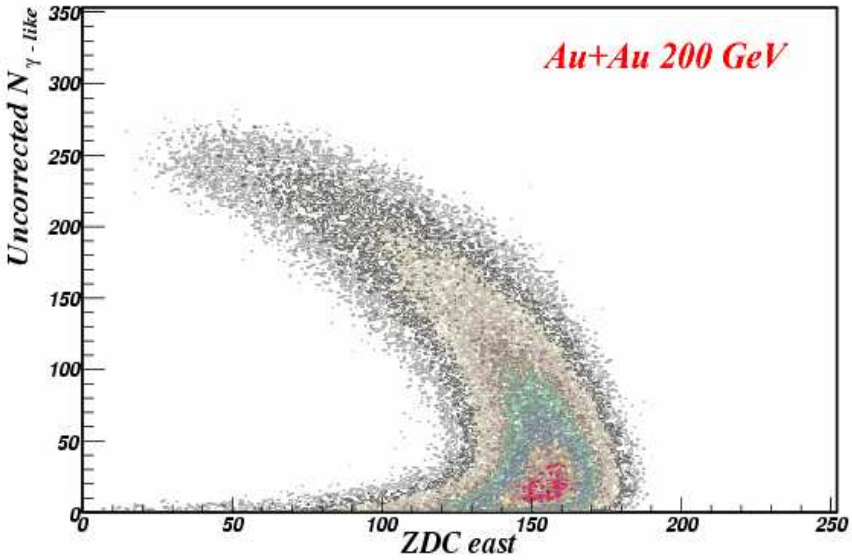

Figure 3.35: *Correlation of uncorrected $N_{\gamma-like}$ with ZDC east in Au+Au Collisions at $\sqrt{s_{NN}}$ = at 200 GeV.*

Bibliography

[1] M.M. Aggarwal, Nucl. Instrum. Methid. A499 751 (2003).

[2] D.P. Mahapatra, et al., A preshower PMD STAR Coll. Note 310, (1997).

[3] M.M. Aggarwal et al.. Nucl. Instrum. Meth. A 372 143 (1996).

[4] M.M. Aggarwal et al.. Nucl. Instrum. Meth. A 421 558 (1999).

[5] Technical Design Report for PMD, ALICE Coll. CERN/LHCC 99-32, (1999).

[6] M.M. Aggarwal et al.. Nucl. Instrum. Meth. A 488 131 (2002)

[7] ALICE HMPID Technical Design Report, CERN/LHCC 98-19, (1998).

[8] F.S. Bieser et al., Nucl. Instrum. Meth. A 499, 766 (2003).

[9] M.M. Aggarwal et al Phys. Rev.C 65, 054912 (2002).

[10] J. Adams et al., STAR Coll. nucl-ex/0311017.

[11] M. Gyulassy and X.N. Wang, Computer Physics Communications, 83 307 (1994).

[12] X. N. Wang, Phys. Rep. 280, 287 (1997); X. N. Wang, Nucl. Phys. A661, 609c (1999).

[13] K.H. Ackermann et al., Nucl. Instr. Meth. A 499, 713 (2003).

[14] J. Putschke, Ph.D Thesis, Max-Planck-Institut fur Physik, Munich (2004); F. Simon, Ph.D Thesis, Max-Planck-Institut fur Physik, Munich (2004)

Chapter 4

Multiplicity and Pseudorapidity Distributions of Photons

4.1 Introduction

The special feature which distinguishes the nucleus-nucleus collisions from the hadron-hadron and the hadron-nucleus collisions is that in the former case, a large amount of energy is released due to numerous nucleon-nucleon interactions and multiple scattering of the constituents within the nuclear dimensions [1]. In very central collisions the nuclei were found to disintegrate completely into light particles. The multiplicities of the particles produced in heavy ion-collisions is a global variable that is essential for their characterization, because it quantifies to which extent the incoming beam energy is released to produce the new particles. It also helps to quantify the relative importance of soft versus hard processes in the particle production mechanisms at different energies. The systematic study of the global observables like transverse energy, multiplicity and momentum spectra of the produced particles may serve as probes for the state of hot hadronic matter. For example, the change in fluctuations due to the formation of the QGP phase may lead to a change in shape of the pseudorapidity distributions of the

produced particles. The particle production mechanism could be different at different regions of pseudorapidity. At mid rapidity a significant increase of charged particle multiplicities normalized to the number of participating nucleons has been observed from peripheral to central $Au + Au$ collisions [2]. This is attributed to the onset of hard scattering processes, which scale with the number of binary collisions. In the framework of the color glass condensate picture of particle production [3, 4, 5], the centrality dependence of the particle production at midrapidity reflects the increase of gluon density due to the decrease in the effective strong coupling constant.

The measurements of the photon multiplicity is complimentary to the measurements of charged particles produced in heavy ion collisions. The inclusive photons provide the picture of the system at freeze out since the majority of the photons are emitted from the decay of the produced particles like π^0, η and only a small fraction is emitted directly during the initial stage of the collisions. The photon multiplicity measurements have also become increasingly important because of the interest in simultaneous measurements of the multiplicity of photons and charged particles in the search for Disoriented Chiral Condensates (DCC) [6]. The measurements of photons can also be used to study flow and intermittency behavior of events accompanying a possible phase transition [7]. In this chapter the multiplicity and the pseudorapidity distributions of photons at forward rapidity in $Au+Au$ and $Cu+Cu$ collisions at RHIC at $\sqrt{s_{_{NN}}} = 200$ GeV measured with the Photon Multiplicity Detector (PMD) of STAR experiment has been studied. The scaling of the production of photons per participant pair and the limiting fragmentation are also presented.

4.2 Multiplicity Distributions

The multiplicity of particles emitted in a heavy-ion collision constitutes an important observable, which reflects the properties and the reaction mechanisms of the system formed

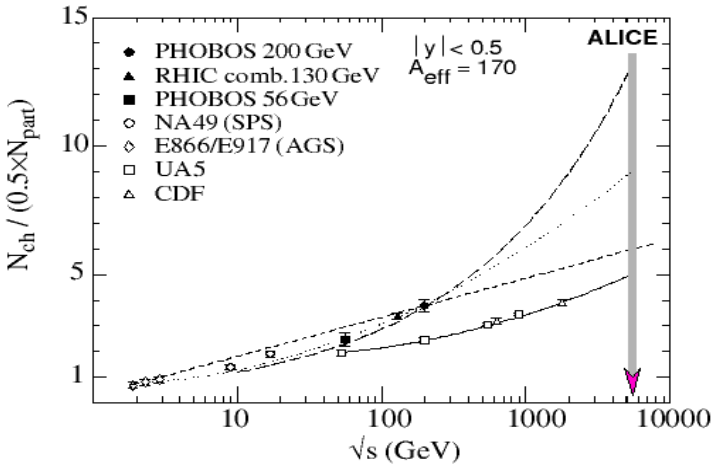

Figure 4.1: *The charged particle multiplicities per participant pair as a function of the centre of mass energy for AA and pp collisions. The solid, dashed and dotted curves show fits to the data of empirical functions. The long-dashed curve shows an extrapolation to LHC energies based on the saturation model.*

in the overlap region between the two colliding nuclei. In addition to the expected soft processes seen at lower energies, hard processes, nuclear shadowing, and hadronic rescattering all play a role. Even without more detailed and differentiated measurements of the emitted particles one can obtain important information about the collision from the measurements of the total multiplicity of the produced particles (charged and neutral), its distribution in pseudorapidity and its dependence on collision centrality and energy. Data at AGS, SPS and RHIC energies show that multiplicities are enhanced by 30% in central collisions between heavy nuclei. The charged-particle multiplicity shows a steady rise from peripheral to central collisions and increases with energy with an approximate logarithmic law [8]. Figure 4.1 shows a compilation of the multiplicities of the charged particles per participant pair at midrapidity at different energies. The extrapolations of RHIC data from $\sqrt{s_{NN}}$ = 200 GeV to 5500 GeV is also shown in the Figure 4.1.

In this section, event-by-event multiplicties of photons and charged particles at for-

ward rapidities are presented. The charged particle multiplicity distribution in elementary and heavy ion collisions are well described by the negative binomial distributions (NBD) [9, 10] defined by

$$P(m) = \frac{(m+k-1)!}{m!(k-1)!}\frac{(\mu/k)^m}{(1+\mu/k)^{m+k}} \tag{4.1}$$

Where P(m) is normalised for $0 \leq m \leq \infty, \mu =< m >$. The NBD becomes a Poisson distribution in the limit $k \longrightarrow$ infinity. The variance and the mean of the NBD is related to k by $1/k = (\sigma^2/\mu^2) - 1/\mu$, where μ is the mean and σ is the standard deviation of the distribution.

The multiplicities of the photons and the charged particles are obtained event-by-event in the PMD and the FTPC respectively in STAR. Figures 4.2, 4.3, 4.4 and 4.5 show the minimum bias distributions of inclusive photons (N_γ) and of charged particles (N_{ch}) for $Au + Au$ and $Cu + Cu$ collisions at $\sqrt{s_{NN}} = 200$ GeV in the forward rapidity. The distributions have characteristic shape with a steep rise corresponding to the most peripheral events. The plateau in the multiplicity distributions corresponds to mid-central events and the fall-off to the most central events. The event-by-event charged particle and photon multiplicity distributions for $0 - 5\%$ for $Au + Au$ and $0 - 10\%$ for $Cu+Cu$ central collisions fitted with Gaussian are also shown in the figures. The photon multiplicity distributions are corrected for efficiency, purity and acceptance defined in chapter 3 where the raw particle multiplicity distributions were presented. The charged particle multiplicities are not corrected for efficiency, purity and acceptance as the earlier studies of $Au + Au$ collisions at $\sqrt{s_{NN}} = 62.4$ GeV shows that the correction factors for FTPC have no strong centrality and η- dependence. It is therefore expected that the scale of N_{ch} will change after correction but the N_{ch} distribution and the correlations with photon multiplicity measurements will remain unaffected.

The correlation between the average number of charged particles and the photons in common pseudorapidity coverage of FTPC and PMD is shown in the Figures 4.6 and 4.7

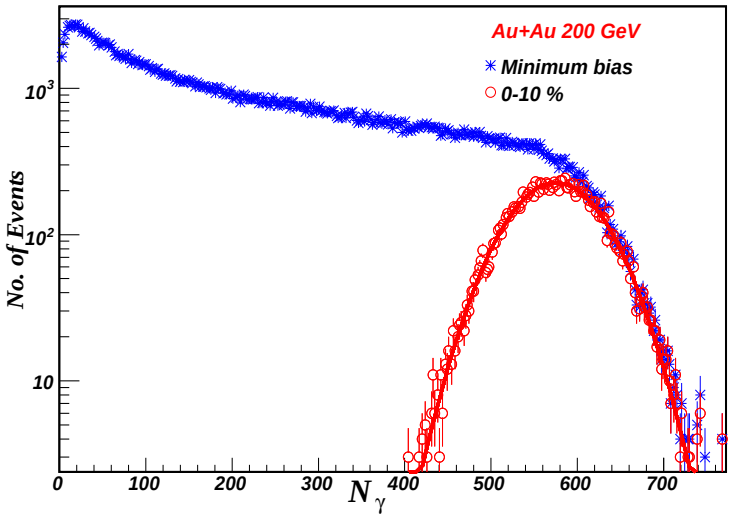

Figure 4.2: *Color(Blue) symbol (astrick) shows the minimum bias distribution for Photons (N_γ) for $Au + Au$ collisions at $\sqrt{s_{NN}}$ =200 GeV. The multiplicity distribution for top 5% central collisions for N_γ are shown with open circle and the solid curve is the Gaussian fit to the data points.*

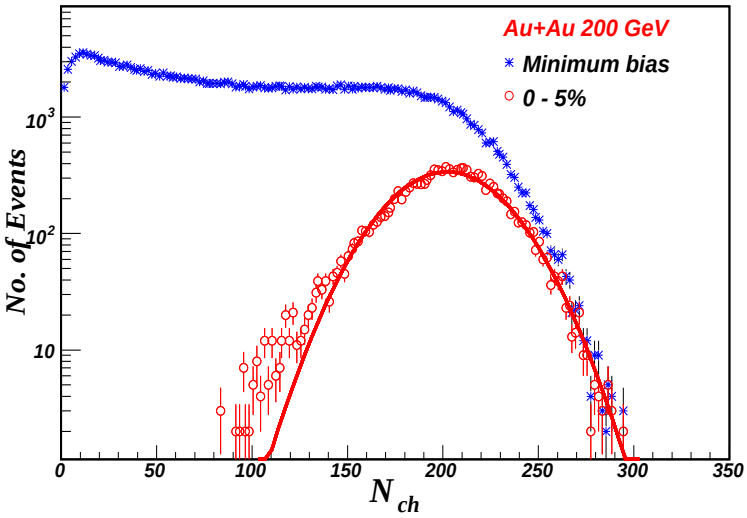

Figure 4.3: *Color(Blue) symbol (astrick) shows the minimum bias distribution for charged particles (N_{ch}) for $Au + Au$ collisions at $\sqrt{s_{NN}}$ =200 GeV. The multiplicity distribution for top 5% central collisions for N_{ch} are shown with open circle and the solid curve is the Gaussian fit to the data points.*

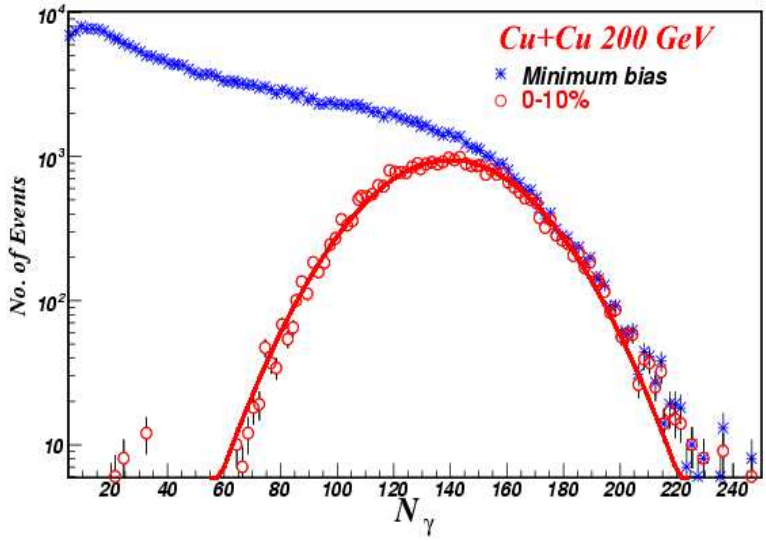

Figure 4.4: *Color(Blue) symbol (astrick) shows the minimum bias distribution for Photons (N_γ) for $Cu + Cu$ collisions at $\sqrt{s_{NN}}$ =200 GeV. The multiplicity distribution for top* 10% *central collisions for N_γ are shown with open circle and the solid curve is the Gaussian fit to the data points.*

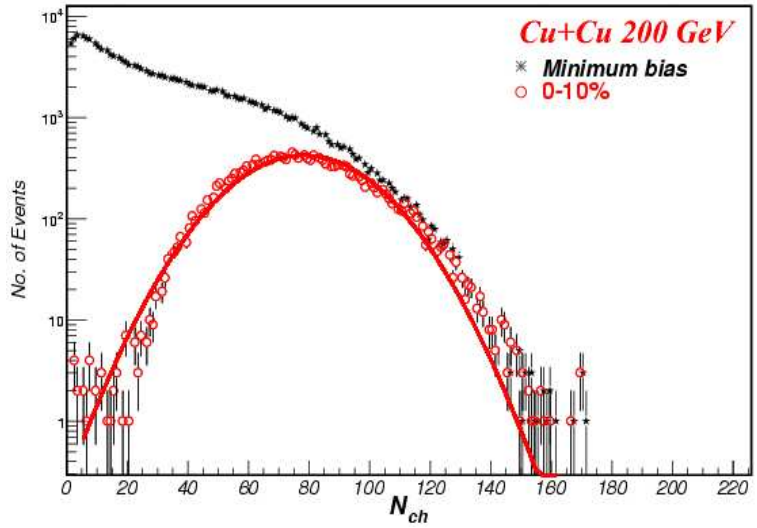

Figure 4.5: *Color(Black) symbol (astrick) shows the minimum bias distribution for charged particles (N_{ch}) for $Cu + Cu$ collisions at $\sqrt{s_{NN}}$ =200 GeV. The multiplicity distribution for top* 10% *central collisions for N_{ch} are shown with open circle and the solid curve is the Gaussian fit to the data points.*

for $Au + Au$ and $Cu + Cu$ collisions respectively at $\sqrt{s_{_{NN}}} = 200\ GeV$. The correlation reflects the variation of $\langle N_\gamma \rangle$ and $\langle N_{ch} \rangle$ with collision centrality. As expected, the $\langle N_\gamma \rangle$ and $\langle N_{ch} \rangle$ are linearly correlated except at higher centrality bins for $Au + Au$ collisions. This must be due to saturation of N_{ch} with centrality. This correlation, therefore shows that the $\langle N_\gamma \rangle$ measured here are mostly from decay products of hadrons and the reaction mechanism applicable to the charged particles can be tested with measured photon multiplicities as well.

4.2.1 Scaling of Photon and Charged Particle Multiplicities

The study of the scaling of particle multiplicity tests the applicability of various models for particle production. Also, the various experimental signatures require comparison of observables of different system sizes, hence a proper understanding of scaling is essential. The collision centrality is either expressed in terms of number of participating nucleons, N_{part} or number of binary collisions, N_{bin}, which provides the information of the contribution of soft and hard processes to the particle production at forward rapidity. The scaling with the number of collisions arises naturally in a picture of a superposition of nucleon-nucleon collisions, with possible modifications by the initial state effects, the participant scaling is more naturally related to a system with strong final state re-scattering, where the incoming particles lose their memory and every participant contributes a similar amount of energy. The scaling behavior can therefore carry important information on the reaction dynamics. It is therefore of interest to study the scaling properties with respect to the number of participants or the number of binary collisions. At mid-rapidity the particle production at $\sqrt{s_{_{NN}}}$= 130 GeV and 200 GeV have been shown to scale with a combination of (N_{part}) and (N_{coll}) [11]. An extension of the measurements of pseudorapidity distributions beyond midrapidity is shown here, where rescattering, stopping and the target fragmentation can influence the shape of the

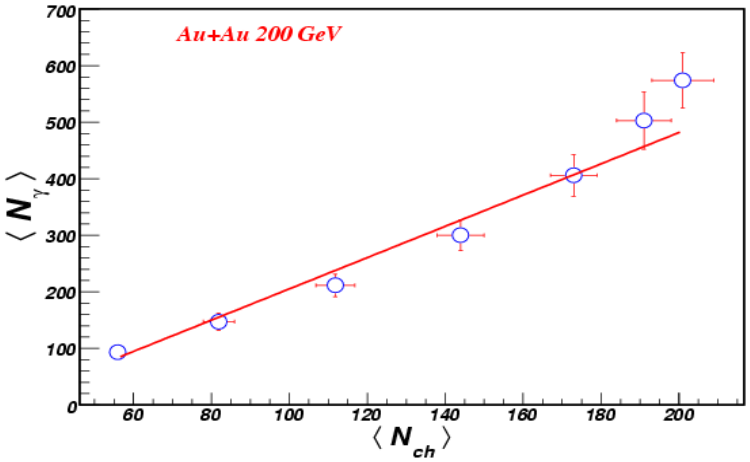

Figure 4.6: *Correlation between the average number of charged particles* $\langle N_{ch} \rangle$ *and the average number of photon* $\langle N_{\gamma} \rangle$ *within the common* η *coverage of PMD and FTPC for different collision centrality in* $Au + Au$ *collisions at* $\sqrt{s_{NN}}$ *=200 GeV and the solid line is polynomial fitted to data points. The photon multiplicity has been corrected for efficiency, purity and acceptance.*

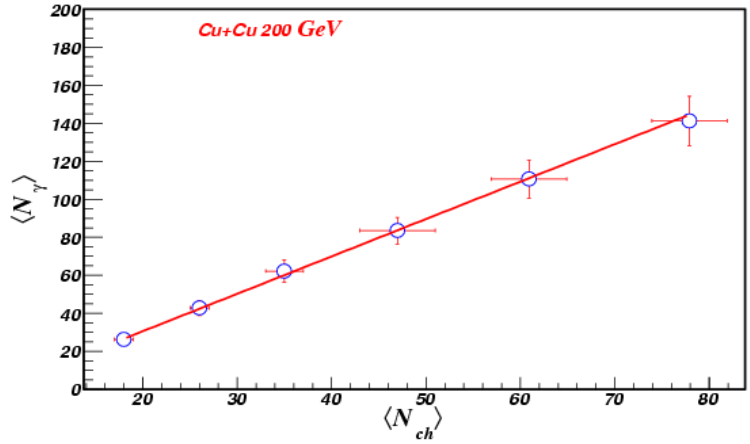

Figure 4.7: *Correlation between average number of charged particles* $\langle N_{ch} \rangle$ *and average number of photon* $\langle N_{\gamma} \rangle$ *within the common* η *coverage of PMD and FTPC for different collision centrality in* $Cu + Cu$ *collisions at* $\sqrt{s_{NN}}$ *=200 GeV and the solid line is polynomial fitted to data points. The photon multiplicity has been corrected for efficiency, purity and acceptance.*

distribution.

The results on the scaling of the photon and the charged particle multiplicity at forward rapidity for $Au + Au$ and $Cu + Cu$ collisions at $\sqrt{s_{_{NN}}}$= 200 GeV are presented in Figures 4.8 - 4.15. The total number of photons and charged particles normalized to the number of participant pair as a function of the number of participant is shown in the Figures 4.8, 4.9, 4.12 and 4.13. The photon and the charged particle production per participating nucleon pair are found to be approximately constant with the centrality in the forward η range studied, while in case of the midrapidity, the pseudorapidity density per participant has a rising trend, at forward rapidity this remains constant. This change might be due to lack of dependence of binary collisions at forward rapidity. At forward rapidity, it is expected that the particle composition will be softer due to large net-baryon content. The effect like shadowing, which will be more prominent at forward rapidity might add to the validity of N_{part} scaling at forward rapidity. In Figures 4.10, 4.11, 4.14 and 4,15, the photons and the charged particle multiplicities normalized with the number of binary collisions N_{bin} as function of N_{bin} is shown, both the photon and charged particle yields donot scale with N_{bin} at forward rapidity.

4.3 Pseudorapidity Distributions

The unique broad pseudorapidity coverage of the multiplicity detectors at RHIC experiments allowed measurement of the $dN_{ch}/d\eta$ distribution in the entire pseudorapidity (η) coverage at all the RHIC energies. The full pseudorapidity distribution of charged particles as shown in Figure 4.16 from PHOBOS experiment [12, 13] at RHIC for central collisions can be described by

$$dN/d\eta = \frac{C}{(1 + exp^{(\eta-\eta_0)/\delta})} \tag{4.2}$$

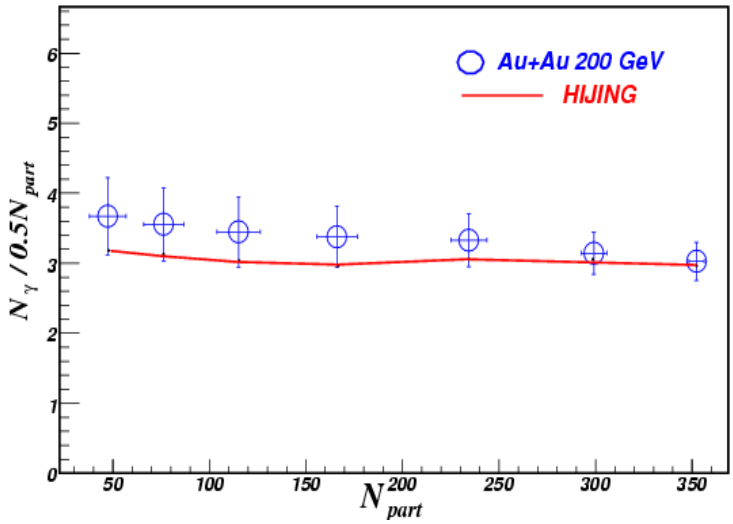

Figure 4.8: *Multiplicity of inclusive photons scaled with the number of participants as function of number of participants for* $Au + Au$ *collisions at* $\sqrt{s_{NN}}$ *=200 GeV. Approximate* N_{part} *scaling is observed.*

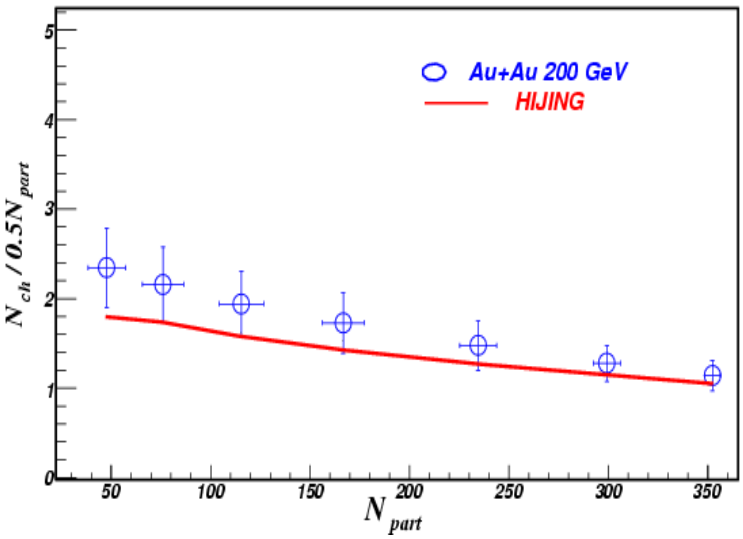

Figure 4.9: *Multiplicity of charged particles scaled with the number of participants as function of number of participants for* $Au + Au$ *collisions at* $\sqrt{s_{NN}}$ *=200 GeV. Approximate* N_{part} *scaling is observed.*

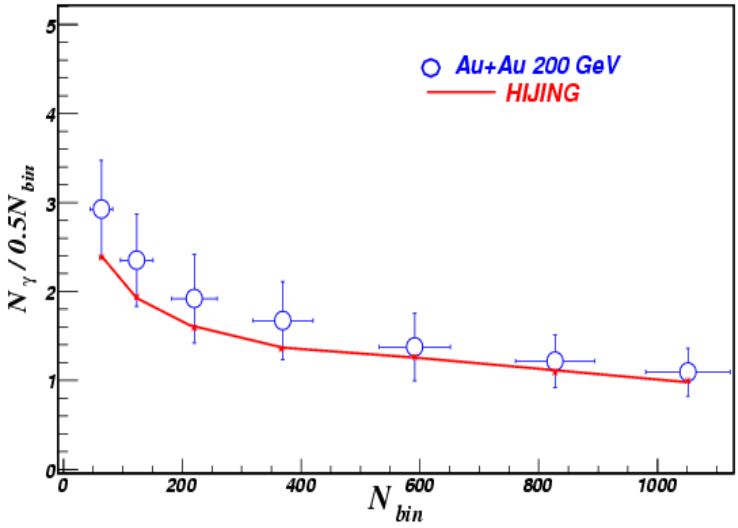

Figure 4.10: *Multiplicity of inclusive photons scaled with the number of binary collisions as function of number of binary collisions for Au + Au collisions at* $\sqrt{s_{NN}}$ *=200 GeV. Unlike* N_{part} *scaling no* N_{bin} *scaling is observed.*

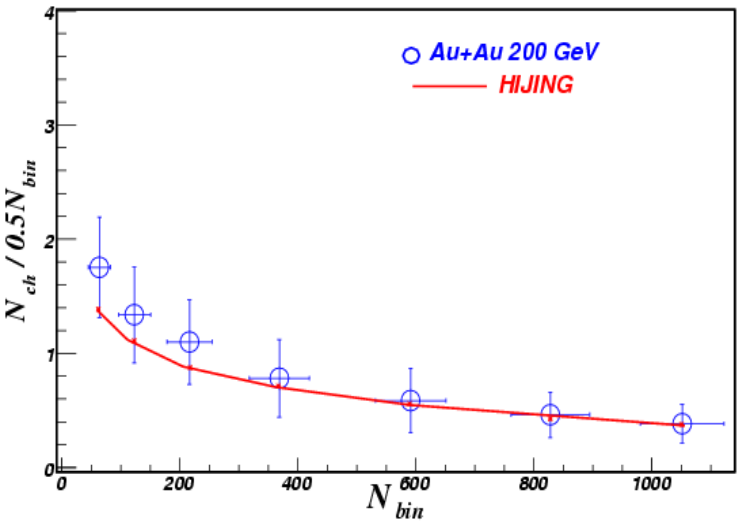

Figure 4.11: *Multiplicity of charged particles scaled with the number of binary collisions as function of number of binary collisions for Au + Au collisions at* $\sqrt{s_{NN}}$ *=200 GeV. Unlike* N_{part} *scaling, no* N_{bin} *scaling is observed.*

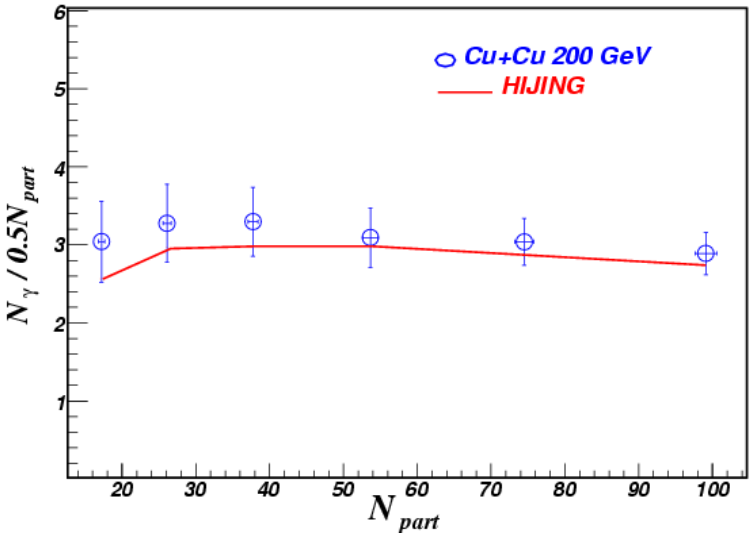

Figure 4.12: *Multiplicity of inclusive photons scaled with the number of participants as function of number of participants for* $Cu + Cu$ *collisions at* $\sqrt{s_{NN}}$ *=200 GeV. Approximate* N_{part} *scaling is observed.*

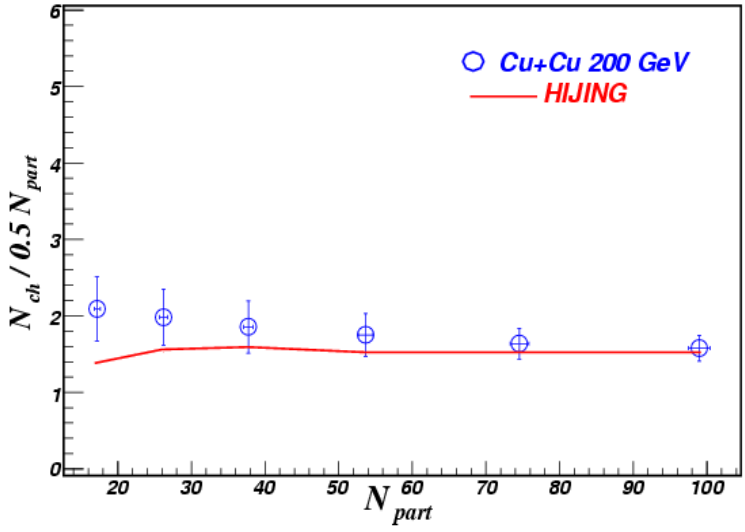

Figure 4.13: *Multiplicity of charged particles scaled with the number of participants as function of number of participants for* $Cu + Cu$ *collisions at* $\sqrt{s_{NN}}$ *=200 GeV. Approximate* N_{part} *scaling is observed.*

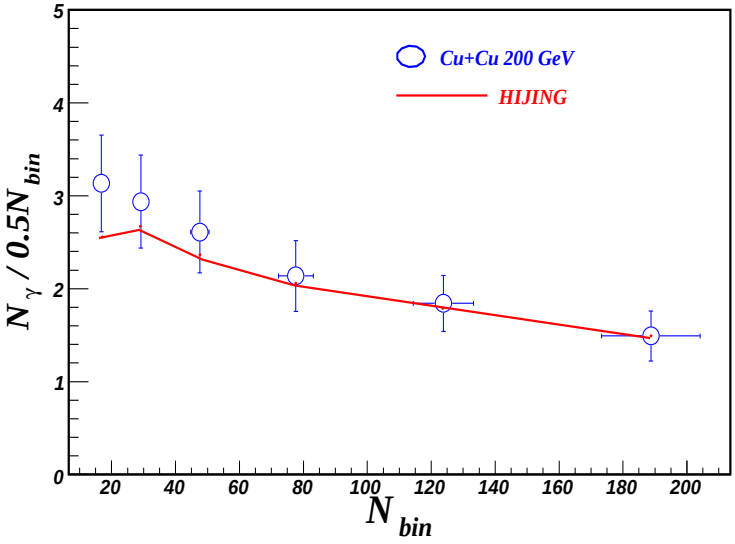

Figure 4.14: *Multiplicity of inclusive photons scaled with the number of binary collisions as function of number of binary collisions for $Cu + Cu$ collisions at $\sqrt{s_{NN}}$ =200 GeV. Unlike N_{part} scaling, no N_{bin} scaling is observed.*

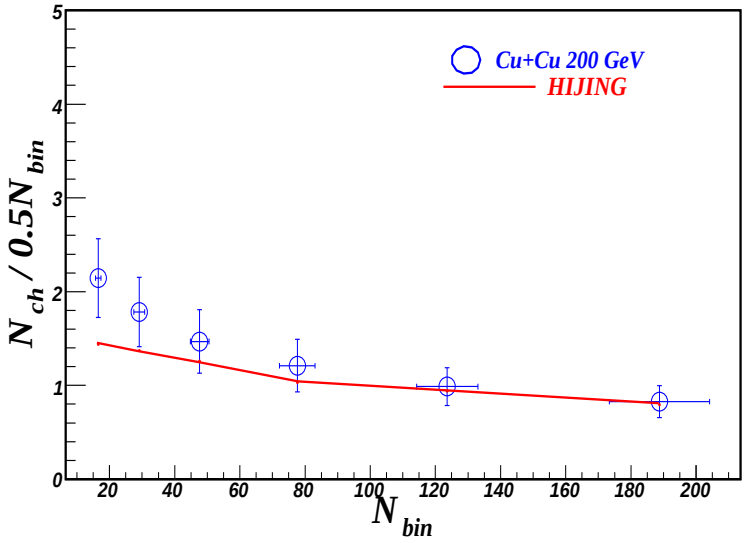

Figure 4.15: *Multiplicity of charged particles scaled with the number of binary collisions as function of number of binary collisions for $Cu + Cu$ collisions at $\sqrt{s_{NN}}$ =200 GeV. Unlike N_{part} scaling, no N_{bin} scaling is observed.*

This formula is chosen to describe the central plateau and the fall in the fragmentation region of the distribution by means of the parameters η_0 and δ.

In this section we have studied the pseudorapidity distributions of inclusive photons in the forward rapidity region $-3.7 \leq \eta \leq -2.3$. The results are compared to a model in order to understand the mechanism of particle production in heavy ion collisions at forward rapidity. Figures 4.17 and 4.18 show the pseudorapidity distributions of photons at $Au+Au$ and $Cu+Cu$ collisions measured at different centrality classes respectively. It is observed that the particle density increases with the decrease in η. The pseudorapidity distributions from data are compared with the corresponding results from HIJING model [14]. The HIJING model is based on the perturbative QCD process which lead to the multiple jet production and the jet interaction (jet quenching) in matter. In this case, the jet quenching has been switched off. HIJING seem to slightly under predict the measured photon multiplicity.

4.3.1 Scaling of Particle Density with Centrality

The scaling of the pseudorapidity density of particles as a function of centrality is an important test for models of particle production in heavy ion reactions because it allows to quantify the relative importance of soft ($\propto N_{part}$) and hard ($\propto N_{coll}$) components. SPS experiments typically performed N_{part}^{α} fits to the measured $dN/d\eta$ with α from 1 to 1.08 (WA98 [15]). This is usually understood as an indication that the hard scatterings do not play an appreciable role at such energies. A convenient variable to be used in such studies is the particle yield per participant pair at mid-rapidity, defined as $dN/d\eta/(N_{part}/2)$. At RHIC energies ($\sqrt{s}$ = 130, 200 GeV) a clear increase [16] is observed in the $dN/d\eta$ per participant pair with increasing centrality, as can be seen in Figure 4.19. Early theoretical explanations attributed this increase to the contribution of hard processes in particle production, which grows with increasing centrality. However, it is observed

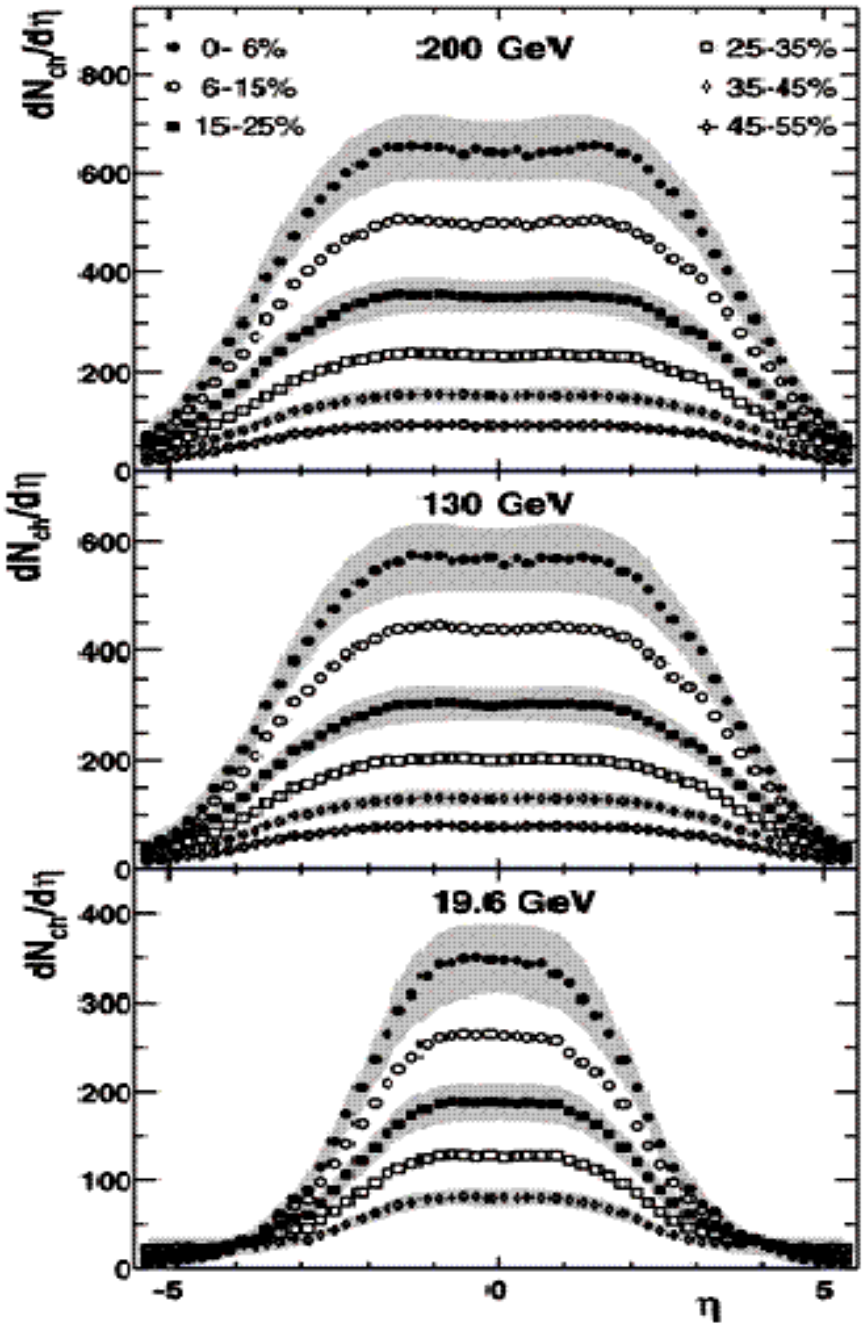

Figure 4.16: *Pseudorapidity distributions of charged particles for Au+Au at* $\sqrt{s_{NN}}$ = *19.6, 130, 200 GeV for different centrality bins at PHOBOS experiment at RHIC.*

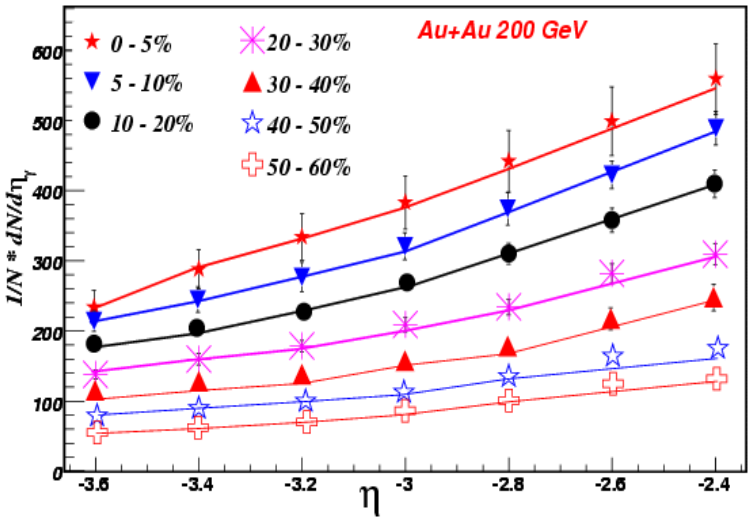

Figure 4.17: *Pseudorapidity distribution for inclusive photons for Au+Au collisions at* $\sqrt{s_{NN}}$*= 200 GeV. The pseudorapidity distributions for different centrality classes are shown and compared to the corresponding distributions from HIJING represented by the solid lines.*

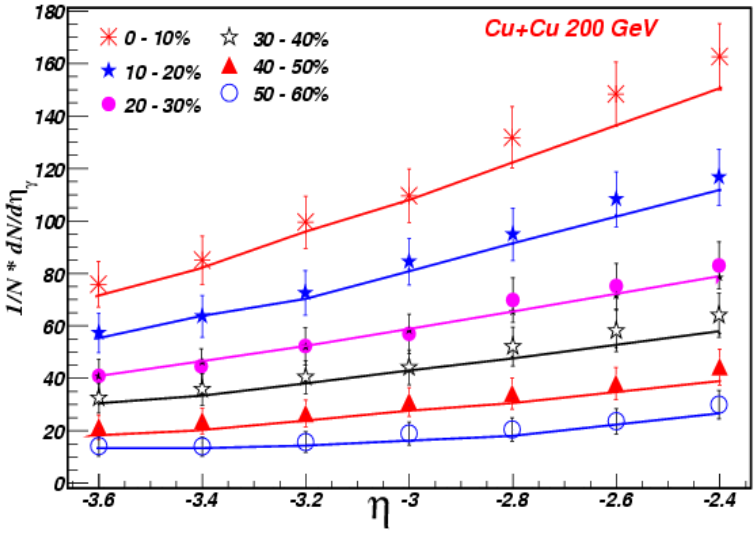

Figure 4.18: *Pseudorapidity distribution for inclusive photons for Cu+Cu collision at* $\sqrt{s_{NN}}$*= 200 GeV. The pseudorapidity distributions for different centrality classes are shown and compared to corresponding distributions from HIJING represented by the solid lines.*

that in the present case the ratio of the measured $dN/d\eta$ per participant pair at the two energies is almost independent of centrality. This is contrary to the prediction shown in Figure 4.19 where the contribution from the hard process should lead to the strong centrality dependence [17]. This consideration is also supported by the results of fits to the data points in Figure 4.19 with a simple two-component parametrization [18]:

$$\frac{dN_{ch}}{d\eta} = n_{pp}((1-x)\frac{\langle N_{part}\rangle}{2} + x\langle N_{coll}\rangle) \tag{4.3}$$

The parameter x, representing the fraction of hard process, is found to be consistent at both energies with a single value $x = 0.13 \pm 0.01 \pm 0.05$ [19]. The RHIC data about particle yields at mid-rapidity are described rather well by models based on parton saturation [20, 21], indicating that high density QCD effects probably play an important role in determining the global event features at RHIC energies. However, as pointed out in [22], different models to calculate N_{part} (which is not a direct experimental observable and affects both axes of Figure. 4.19) would lead to different slopes for the centrality dependence of the $dN/d\eta$ per participant pair, thus weakening the relevance of parton saturation and Color Glass Condensate [23] in the initial state of RHIC collisions.

4.3.2 Scaling of Particle Density with Energy

Important information can be extracted analyzing the pseudorapidity density of particles produced for central events as a function of the center-of-mass energy of the collision. The scaling of $dN/d\eta$ per participant pair as a function of energy ($\sqrt{s_{NN}}$) for central heavy-ion collisions from AGS to RHIC energies [24] is shown in Figure 4.20 The measured multiplicities appear to fall on a smooth curve from AGS to top RHIC energies and this result contrasts with some theoretical predictions made before RHIC startup, which were suggesting strong energy dependence accompanying the hadron to QGP phase transition. Figure 4.21 shows the scaling of the $dN_\gamma/d\eta$ per participant pair as function of energy at forward rapidity for photons. The data presented here is from the

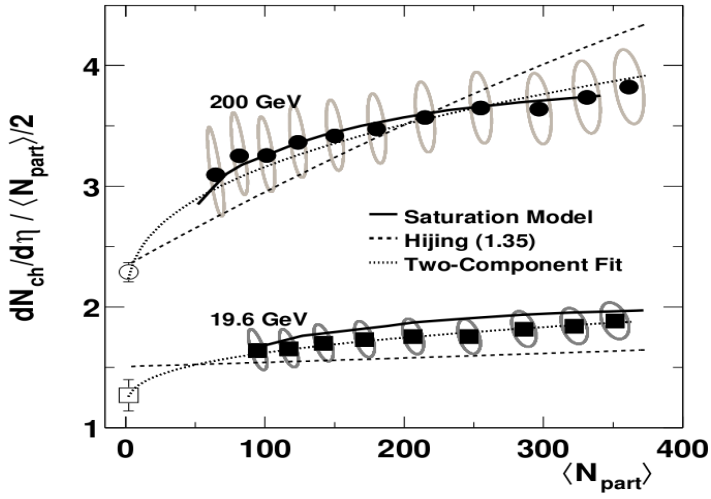

Figure 4.19: *Pseudorapidity density per participant pair at mid-rapidity as a function of centrality measured by PHOBOS experiment at* $\sqrt{s}$ *=19.6 and 200 GeV.*

STAR and the WA98 experiments. The WA98 data is slightly at midrapidity while the STAR data is from forward rapidity.

4.4 Limiting Fragmentation

The hypothesis of the limiting fragmentation in high energy hadron-hadron collisions was suggested nearly four decades ago [25]. This hypothesis states that the produced particles, in the rest frame of one of the colliding hadrons, will approach a limiting distribution. These universal distributions describe the momentum distributions of the fragments of the other hadron. Central to the original hypothesis of the limiting fragmentation in [26] was the assumption that the total hadronic cross sections would become constant at large center-of-mass energy. If this occurred, the excitation and the break-up of a hadron would be independent of the center-of-mass energy and distributions in the fragmentation region would approach a limiting curve. Even though the

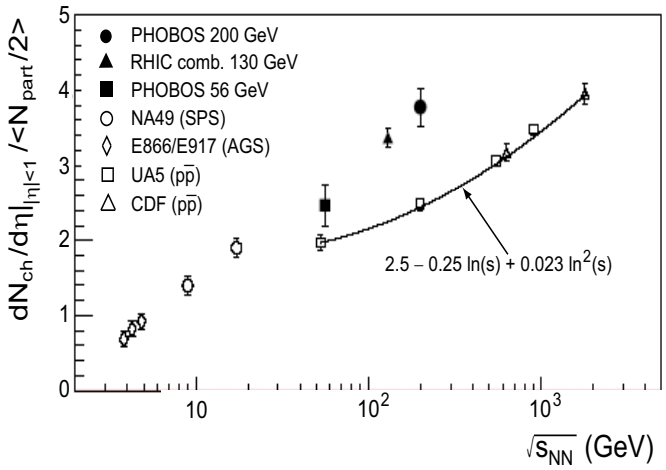

Figure 4.20: *Energy dependence of the pseudorapidity density of charged particles per participant pair for the most central ion-ion collisions from AGS to RHIC. The $pp(\bar{p}$ data are superimposed).*

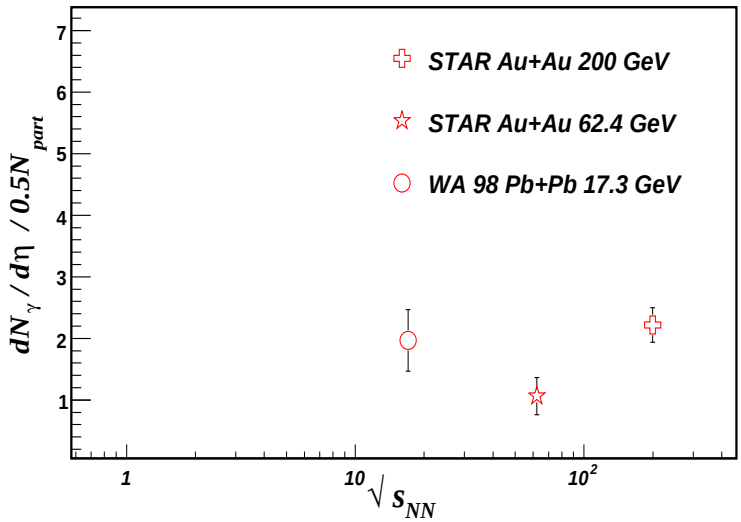

Figure 4.21: *Energy dependence of the pseudorapidity density of photon per participant pair as function of energy. Error shown is only statistical.*

cross-sections are not constant, limiting fragmentation appears to have a wide regime of validity. BRAHMS and PHOBOS experiments at RHIC have performed detailed studies of the pseudo-rapidity distribution of the produced charged particles $dN_{ch}/d\eta$ for a wide range ($-5.4 < \eta < 5.4$) of pseudo-rapidities, and for several center-of-mass energies ($\sqrt{s_{_{NN}}}$ = 19.6, 62.4, 130 and 200 GeV) in nucleus- nucleus (Au-Au and Cu-Cu) and deuteron-nucleus ($d - Au$) collisions [27]. In particular, they have performed detailed studies of the limiting fragmentation phenomenon. The pseudo-rapidity distribution $dN/d\eta'$ (where $\eta' = \eta$ - Y_{beam} is the pseudorapidity shifted by the beam rapidity which grows with energy, so higher energy collisions must be shifted further given by $y_{beam} = ln\frac{\sqrt{s}}{m_p}$ is observed to become independent of the center-of-mass energy ($\sqrt{s_{_{NN}}}$) in the region around $\eta' \sim 0$ [28]. In this section, the limiting fragmentation for photons at various centralities is presented and is compared with the different system size and energies.

4.4.1 Centrality Dependence of Limiting Fragmentation for Photons

The amount of matter available in a given collision is usually related to the number of participating nucleons N_{part}. The particles produced in heavy ion collisions increase from peripheral to central collisions as one can see in all the 3 panels in Figure 4.16. Figure 4.22 shows photons pseudorapidity distributions scaled by the number of participant pairs, measured for two centrality classes: $0-5\%$ and $10-20\%$ for $Au+Au$ and $0-10\%$ and $10-20\%$ for $Cu+Cu$ collisions at $\sqrt{s_{_{NN}}} = 200$ GeV. The photon yield normalized to the number of participating nucleons as a function of $\eta - y_{beam}$ is found to be independent of the centrality for both the systems. The independence of the longitudinal scaling of photons on the centrality has been attributed to mesons being the dominant source of photon production.

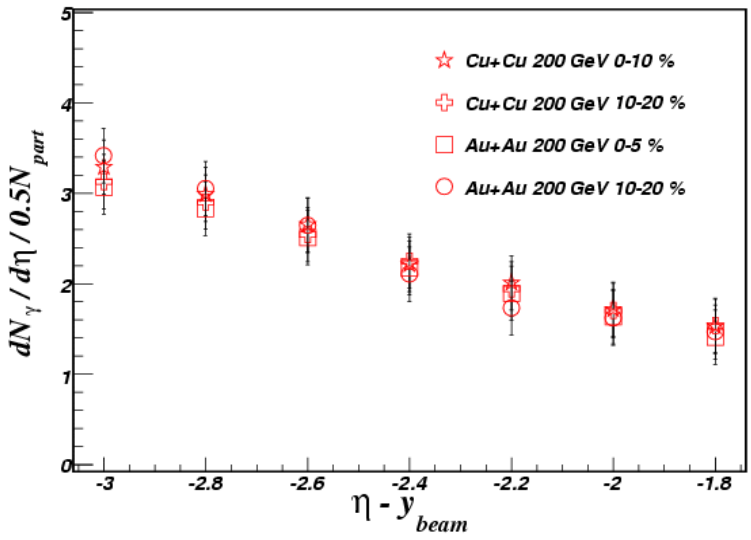

Figure 4.22: *Centrality dependence of longitudinal scaling for inclusive photons at* $\sqrt{s_{NN}}$ *= 200 GeV for Au+Au and Cu+Cu collisions. The inclusive photons follow centrality independent longitudinal scaling.*

4.4.2 System Size and Energy Dependence of Limiting Fragmentation

It has been observed that the number of charged particle produced per participant pair as a function of $\eta - Y_{beam}$, is independent of beam energy [29, 30]. Figure 4.23 shows the system size and the energy dependence of the limiting fragmentation for photons at forward rapidity for various systems from $p + \bar{p}$, $Cu + Cu$, $Au + Au$ and $Pb + Pb$. We have compared the photon pseudorapidity distribution per participant pair for $Au + Au$ and $Cu + Cu$ central events at $\sqrt{s_{NN}}$ = 200 GeV as function of $\eta - y_{beam}$. We have also compared the photon pseudorapidity distribution per participant pair with central $(0 - 5\%)$ photon data for $Pb + Pb$ collisions at 17.3 GeV from the WA98 experiment [31] at SPS and the data from UA5 experiment [32] for $p + \bar{p}$ at $\sqrt{s_{NN}}$ = 540 GeV. We observe that the photons follow universal limiting pseudorapidity distribution away from mid rapidity which is independent of energy, centrality and system size.

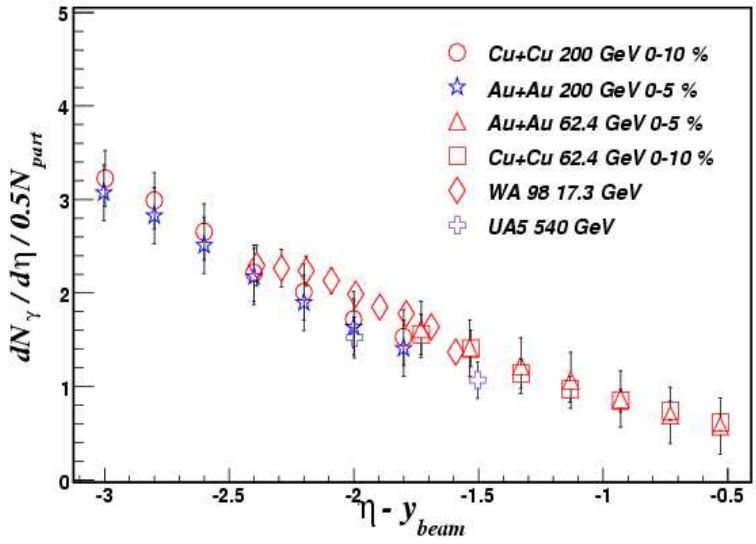

Figure 4.23: *Energy and system size dependence of longitudinal scaling for inclusive photons for* $Au+Au, Cu+Cu, Pb+Pb$ *and* $p+\bar{p}$*. The inclusive photons follow centrality independent longitudinal scaling.*

Bibliography

[1] G. Singh, K. Sengupta and P.L. Jain, Phys. Rev. Lett., 61, 1073 (1988).

[2] K. Adcox et. al,. PHENIX Coll. Phys. Rev. Lett. 96, 3500 (2001).

[3] L. McLerran and R. Venugopalan, Phys. Rev. D 49, 2233 (1994).

[4] L. McLerran and R. Venugopalan, Phys. Rev. D 50, 2225 (1994).

[5] Y.V. Kovchegov, Phys. Rev. D 54, 5463 (1996).

[6] M. M. Aggarwal et, al., WA98 Coll. Phys.Rev.C64:011901, (2001).

[7] M. M. Aggarwal et. at., WA98 Coll. Phys. Lett. B403 390 (1997)

[9] G. Alner et. al., UA5 Coll. Phys. Rep. 154 247 (1987).

[10] T. Abbott et. al., E-802 Coll. Phys. Rev. C 52 2663 (1995).

[11] K. Adcox et. al., E-802 Coll. Phys. Rev. C 52 2603 (1995).

[12] K. Adox et al., PHENIX Coll. Phys. Rev. Lett. 86, 3500 (2001).

[13] B. B. Back et. al., PHOBOS Coll. Phys. Rev. Lett. 87 102303 (2001),

[14] B. B. Back et. al., PHOBOS Coll. Phys. Rev. Lett. 91 052303 (2001),

[15] X. N. Wang and Miklos Gyulassy Phys. Rev. D 44, 3501 (1991)

[16] M. M. Aggarwal et al. WA98 Coll. Eur.Phys.J.C18:651-663, (2001).

[17] I. Arsenej et. al., BRAHMS Coll. Nucl. Phys. A 757, 1-2 (2005).

[18] X. N. Wang and M. Gyulassy Phys. Rev. D44 3501 (1991).

[19] X. N. Wang Phys. Rep. 280 287 (1997)

[20] B. B. Back et al. PHOBOS Coll. Phys.Rev. Lett. 85, 3100 (2000).

[21] K. Adcox et. al., PHENIX Coll. Phys. Rev. Lett. 86, 3500 (2001).

[22] A. Adil, H. J. Drescher, A. Dumitru, A. Hayashigaki and Y. Nara, Phys. Rev. C 74, 044905 (2006).

[23] A. Krasnitz and R. Venugopalan, Phys. Rev. Lett. 84, 4309 (2001).

[24] B. B. Back et al. PHOBOS Coll. Phys. Rev. C 65, 061901 (2002).

[25] J. Benecke, T. T. Chou, C.N. Yang and E. Yen, Phys. Rev. 188 2159 (1969).

[26] B. B. Back et. al., PHOBOS Coll. Nucl Phys. A757, 28 (2005); G.I. Veres, nucl-ex/0511037 (2005).

[27] B. B. Back, et. al., PHOBOS Coll. Phys. Rev. C 72, 031901 (2005).

[28] B. B. Back, et. al., PHOBOS Coll. Phys. Rev. C 70, 021902 (2004).

[29] B. B. Back, et. al., PHOBOS Coll. Phys. Rev. Lett. 93, 082301 (2004).

[30] I. G. Bearden, et., al. BRAHMS Coll. Phys. Rev. Lett. 88, 202301 (2002).

[31] I. G. Bearden, et. al., BRAHMS Coll. Phys. Lett. B 523, 227 (2001).

[32] G. Alner et. al., UA5 Coll. Phys. Lett., B138 304 (1984); Phys. Lett., B167 476 (1986).

Chapter 5

Correlations and Fluctuations between Photons and Charged Particles

5.1 Introduction

Any physical quantity measured in an experiment is subject to fluctuations. In general, these fluctuations depend on the properties of the system under study (in the case at hand, on the properties of a fireball created in a heavy ion collision) and may contain important information about the system. The fluctuations and correlations are methods used widely to characterize a physical system. One can distinguish between several classes of fluctuations. On the most fundamental level there are quantum fluctuations, which arise if the specific observable does not commute with Hamiltonian of the system under consideration. Secondly, there are 'dynamical' fluctuations reflecting the dynamics and the response of the system. Finally, there are 'trivial' fluctuations induced by the measurement process itself, such as finite number statistics etc. The quantum fluctuations are less important in heavy ion collisions while trivial fluctua-

tions need to be understood, controlled and subtracted in order to access the dynamical fluctuations which tell us about the proporties of the system. The original motivation for event-by-event (E-by-E) studies in ultra relativistic heavy ion collisions has been to find indications for distinct event classes. In particular it was expected that one would find events which would carry the signature of the Quark Gluon Plasma. First pioneering experiment in this direction has been carried out by the NA49 collaboration [1, 2]. They analysed the E-by-E fluctuations of the mean transverse momentum as well as the fluctuation of ratio of Kaon to Pion multiplicities. The correlations measured between produced particles reveal several important aspects of the particle production. Based on the study of correlations (e.g η, ϕ correlation, $\eta - \phi$ correlation, p_T correlation), one can reveal information about the collective properties of the system (flow, production of jets/minijets). Correlated production of the photons and the charged particles reveal exotic phenomenon like DCC.

5.2 Event-by-Event Fluctuations

The study of correlations and fluctuations in relativistic nuclear collisions addresses fundamental aspects of Quantum Chromo Dynamics (QCD) and the properties of strongly-interacting matter at extreme density and temperature. The correlations and fluctuations reveal the nature of QCD, first through the structure of elementary collisions and then through the properties and dynamics of the colored medium produced in heavy ion (HI) collisions. The large number of particles produced in the relativistic heavy-ion collisions at relativistic heavy-ion collider (RHIC) provide an opportunity to analyze and study, on an event-by-event basis, fluctuations in physical observables, such as particle multiplicities, transverse momenta. The fluctuations of thermodynamical quantities provide a unique framework for studying the nature of QGP phase transition and provide direct insight into the properties of the system created in the high energy collisions.

Apart from the statistical fluctuations due to the geometrical properties of the collisions [3, 4, 5], event-by-event fluctuations may be related to the thermodynamics of the system (such as the temperature) [6, 7], to fluctuations of conserved quantities (such as the netcharge) [8], to jets and minijets [9], and also to more exotic phenomenon (such as Disoriented Chiral Condensate formation [10]).

So far, most of the event-by-event analysis have concentrated on the fluctuations of particle multiplicity, their ratio [11], transverse momentum [12], the netcharge [13] and Kaon-to-pion (K/π) ratio [14]. The enhanced fluctuations of energy density points to a first order phase transition whereas a second order phase transition may result into the divergence of specific heat. The study of the event-by-event fluctuations in $\langle p_T \rangle$ [15] could be used to look for the nature and order of the phase transition. Another aspect of these studies is to search for the existence and location of the critical point in the quark-hadron phase diagram as it is believed to observe large fluctuations of thermodynamic quantities in the vicinity of the critical point. Here we will review the various experimental searches that have been performed so far and will apply a new method to study the DCC formation.

5.3 Fluctuations in the Ratio of Photon and Charged Particle Multiplicities: A Signal for DCC

In very high-energy hadronic and /or nuclear collisions highly excited states are produced and subsequently decay via the incoherent multi-particle emission. This may results in the formation of domains of unconventionally oriented vacuum configurations of low momentum pions as allowed by the chiral symmetry called the Disoriented Chiral Condensates (DCC). Due to the semi-classical nature of the corresponding emission processes, this may lead to specific signatures, such as anomalously large event-by-event

fluctuations of the charge-to-neutral ratio of produced pions. If the space-time region where the domain is large enough the phenomenon might be experimentally observable, thereby providing an interesting opportunity to study the chiral structure of QCD. The DCC pions are expected to be mostly concentrated at low momentum in the DCC rest frame and the DCC emission should, therefore, be characterized by a cluster of pions with low relative momenta. In the present section we describe various signatures which have been discussed in the literature and the tools used in DCC searches.

By DCC, we mean a piece of strong interaction vacuum with rotated value of its chiral order parameters. The formation of DCC domains have been proposed by Anselm [16], by Blaziod and Krzywicki [17] and by Brojken, Kowalski and Talyer [18] in the context of high energy hadronic collisions to explain the cosmic ray experiments [19] and later on by Rajagopal and wilczek [20] in context of heavy ion reactions. The QCD vacuum contains a boson condensate, like the Higgs sector of electroweak theory. This condensate arises as a consequence of the spontaneous breaking of chiral symmetry of QCD. The collective excitations of these condensate are pions and would be stricktly massless where chiral symmetry is exact. The condensate transforms as a 4-vector (σ, π) and in ordinary vacuum points in sigma direction. But in the interior of high energy collision fireball the orientations is different. If so, the piece of disoriented vacuum will decay into true vacuum and decay products will be a pulse of coherent semiclassical pion field carrying the quantum numbers of disoriented vacuum. In particular all decay pions in given event will have same isospin. This feature leads to the basic signature for DCC search, namely large fluctuations in the fractions of produced pions which are neutral.

In generic particle production mechanism, because of the isospin conservation in the strong interaction, the production of π^0, π^+ and π^- are equally probable. This mechanism leads to a binomial distribution of neutral pion fraction (f) peaking at 1/3. For a large number of events having high multiplicity of pions produced, as in the

case of heavy ion collisions, this distribution for normal events can be approximated as Gaussian with mean at 1/3. Due to the asymmetric nature of the pion production for DCC domains, it is expected that an event-by-event analysis will show fluctuations in the neutral-pion fraction.

In particular, the presence of the DCC pions would hardly be detectable in global observables such as the single-pion inclusive spectrum and in such conditions the, event-by-event analysis seems to be preferable and will be discussed in the following sections. If the orientation of the chiral order parameters is random, event by event probability distribution of the neutral pion fraction (f) for DCC is characterized by:

$$P(f) = \frac{1}{2\sqrt{f}} \tag{5.1}$$

where f is fraction of the produced pions and is given by:

$$f = \frac{N_{\pi^0}}{N_{\pi^0} + N_{\pi^+} + N_{\pi^-}} \tag{5.2}$$

$$\approx \frac{N_{\gamma/2}}{N_{\gamma/2} + N_{ch}} \tag{5.3}$$

N_γ and N_{ch} are multiplicities for photons and charged particles, respectively. This assumes all charged particles are pions and all photons come from π^0 decay. As already emphasized, the formation of DCC is expected to be a rare phenomenon and the main difficulty is to isolate any DCC signal from the enormous background of 'incoherent' pions, produced by standard mechanisms.

The event-by-event fluctuations of photon-to-charge particle ratio has been one of the predicted signals for the formation of the DCC formations and has been studied by the MiniMax experiment in *pp* collisions at the Tevatron energy [21] and by the NA49 experiment [22] at CERN SPS. From these experiments no conclusive evidence for DCC formation was observed. The WA98 experiment has also studied the correlated

neutral-to-charge particle fluctuations [23] and by the discrete wavelet technique (DWT) in Pb+Pb collisions at 158 GeV and upper limits on DCC formation have been reported. Different methods have been used to measure the photon-to-charged fluctuations and correlations.

5.3.1 Experimental Techniques Developed for DCC Search

Numerous experimental searches have been performed in parallel with the development of theoretical ideas. These include the analysis of various cosmic-ray experiments [24, 25], nucleon-nucleon collisions at CERN [26, 27] and at Fermilab [28], with the dedicated MiniMax experiment [29], as well as the nucleus-nucleus collisions at the CERN SPS [30, 31] and presently at RHIC [32, 33]. The search for DCC and other exotic events is a part of the heavy-ion physics program to be performed by the multi-purpose detector ALICE at the LHC [34]. These investigations have led to the development of powerful experimental tools to search for the non-statistical fluctuations and/or to detect non-trivial structures in high-multiplicity events. No clear positive signal has been reported so far and the upper bounds have been put on the likelihood of DCC formation, in particular, in heavy-ion collisions at SPS energies [35, 36, 37].

5.3.1.1 Multi−Resolution Discrete Wavelet Analysis

The multi-resolution discrete wavelet technique (DWT) has been used to look for bin-to-bin fluctuations in charged particle and photon multiplicity distributions in WA98 experiment at SPS. The DWT technique has the beauty of analyzing a distribution of particles at different length scales with the ability of finally picking up the right scale at which there is a fluctuation above background. This method is discussed in [38] and has been used in WA98 experiment to look for DCC type of events.

5.3.1.2 Sliding Window Method

The Sliding Window Method (SWM) [39] was used in WA98 experiment to look for the fluctuations in charged to neutral particle ratio by looking in $\eta - \phi$ windows in azimuthal plane. A window of size $\delta\phi$ is chosen in the common coverage of the two detectors in which the neutral pion fraction f is calculated. The entire azimuthal range of common coverage is scanned by continuously sliding the window, shifting each time by a small amount, say $\delta\phi$, to search for a patch having a neutral pion fraction several standard deviations away from the mean value. This method utilizes the full advantage of azimuthal resolution of the detectors and allows direct observation of patches having large (or small) $f-$ values. The value of $\delta\phi$ depends on the azimuthal resolution of the two detectors. The SWM provides a set of f-values in each event. The sensitivity of the SWM to extract DCC-like fluctuation is decided by the limit of the statistical background that can be obtained from mixed event sample. The SWM is a general method and can be utilized not only in azimuthal space but also in pseudorapidity space or even in any combined phase space with multi-dimensional windows and using any suitable physical observable which can be computed over the window.

5.3.1.3 Φ - Measure

The $\Phi-$ measure [40] for a system of particles is defined as :

$$\Phi = \sqrt{\frac{\langle Z^2 \rangle}{\langle N \rangle}} - \sqrt{\bar{z}^2} \tag{5.4}$$

where $z = x$ - $\bar{x}$, x is the value of a given single-particle observable in a given event and $\bar{x}$ is its average over all particles and all events. The event variable Z is a multi-particle analog of z defined as:

$$Z = \sum_{i=1}^{N} (x_i - \bar{x}) \tag{5.5}$$

where the summation runs over all particles from a given event. The $\Phi-$measure can be used to study the fluctuations in particle species. In the case, the single-particle variable x =1, if the particle is of a given sort (say a neutral pion) and x=0 otherwise (charged pion). This has been applied to study the fluctuations of the neutral pion fraction f from DCC in [41]. Denoting by $N_\pi = N_{\pi^0} + N_{ch}$, the total pion multiplicity in a given event, one can write $N_{\pi^0} = fN_\pi$ and $N_{\pi+-} = (1-f)N_\pi$, where f is the fraction of neutral pion in an event. Assuming that the relative fluctuations in N_π are small, that is $\langle \delta N_\pi^2 \rangle \ll \langle N_\pi \rangle^2$, one obtains:

$$\Phi \approx \sqrt{\langle N_\pi \langle \delta f^2 \rangle \rangle} - \sqrt{\langle f \rangle \langle 1-f \rangle} \tag{5.6}$$

Properties of $\Phi - measure$ to consider :

For non DCC case:

$$\Phi_{nonDCC,uncorr} = 0 \tag{5.7}$$

For non DCC, but N_{π^0} and N_{ch} have non-trivial correlations:

$$\Phi_{nonDCC,corr} = -\sqrt{\delta(1-\delta)} \tag{5.8}$$

For ideal DCC case :

$$\Phi_{DCC} = \sqrt{\frac{4\langle N_\pi \rangle}{45}} - \frac{2}{9} \tag{5.9}$$

It is positive for $\langle N_\pi \rangle > 5/2$. For a typical case where the total pion multiplicity $N_\pi \approx 300$, one finds $\Phi_{DCC} \approx 4.7$. It is worth emphasizing that this assumes that all the observed pions are of DCC origin.

5.4 Methods Used

In the present study two methods are used as measure of the fluctuations in correlated production of photons and charged particles to look for DCC signal.

5.4.1 $\sigma^2/mean$

$\sigma^2/mean$ measures the width of the distribution of the N_γ/N_{ch}, where N_γ and N_{ch} being the photon and the charged particle multiplicities respectively.

5.4.2 $\nu_{dynamics}$

Fluctuations in the ratio of two quantities measures the width of the two particle densities and therefore provides additional information than just the averages. The $\nu_{\alpha\beta dyn}$ can be expressed in terms of two particle integral correlation function as:

$$\nu_{\alpha\beta dyn} = R_{\alpha\alpha} + R_{\beta\beta} - 2R_{\alpha\beta} \tag{5.10}$$

where the terms $R_{\alpha\beta}$ are ratios of integrals of two and single particle densities defined as:

$$R_{\alpha\beta} = \frac{\int d\eta_\alpha d\eta_\beta \frac{dN}{d\eta_\alpha d\eta_\beta}}{\int d\eta_\alpha \frac{dN}{d\eta_\alpha} \int d\eta_\beta \frac{dN}{d\eta_\beta}} - 1 \tag{5.11}$$

Rather than measuring the event-by-event fluctuations of a ratio of the charged particle multiplicities and photon multiplicities in a given acceptance, one considers the second moment of the difference between the relative multiplicity $\frac{N_\gamma}{\langle N_\gamma \rangle}$ and $\frac{N_{ch}}{\langle N_{ch} \rangle}$ as follows

$$\nu_{\gamma ch} = \langle (\frac{N_\gamma}{\langle N_\gamma \rangle} - \frac{N_{ch}}{\langle N_{ch} \rangle})^2 \rangle \tag{5.12}$$

In the Poisson limit, the $\nu_{\gamma ch,stst}$ of this quantity is equal to

$$\nu_{\gamma ch,stat} = \frac{1}{\langle N_\gamma \rangle} + \frac{1}{\langle N_{ch} \rangle} \tag{5.13}$$

The 'non-statistical' or 'dynamical' fluctuations can thus be expressed as the difference between the above two quantities:

$$\nu_{\gamma ch,dyn} = \nu_{\gamma ch} - \nu_{\gamma ch,stat} \tag{5.14}$$

$$= \frac{\langle N_\gamma(N_\gamma - 1) \rangle}{\langle N_\gamma \rangle^2} + \frac{\langle N_{ch}(N_{ch} - 1) \rangle}{\langle N_{ch} \rangle^2} - 2\frac{\langle N_\gamma N_{ch} \rangle}{\langle N_\gamma \rangle \langle N_{ch} \rangle} \tag{5.15}$$

The $\nu_{\gamma ch,dyn}$ basically measures the relative correlation strength of $\gamma - \gamma$, $ch - ch$, and $\gamma - ch$ particle pairs. For Poissonian system, the $\nu_{\gamma ch,dyn}$ is zero. The definition of $\nu_{\gamma ch,dyn}$, its properties and relationships to other measures of event-by-event fluctuations are discussed in [42, 43]. The robustness of $\nu_{\gamma ch,dyn}$ as an experimental observable was also discussed on the basis of Monte Carlo toy model in [44], where the authors verified explicitly that $\nu_{\gamma ch,dyn}$ is less dependent on acceptance and efficiency of the detector.

5.4.3 Results

We present the $\sigma^2/mean$ and the $\nu_{\gamma ch,dyn}$ results as a function of the collision centrality which is defined as the number of participating nucleons in $Au + Au$ and $Cu + Cu$ collisions at $\sqrt{s_{NN}} = 200$ GeV. The details of the presented data and the quality cuts used are discussed in the chapter 3.

5.4.4 $\sigma^2/mean$

The $\sigma^2/mean$ shows the width of the distribution of the ratio of (N_γ/N_{ch}) and consists of the contributions from N_γ and N_{ch}. We obtain the width of the ratio, there by cancelling the volume fluctuation contributing from the impact parameters fluctuations affecting the terms. It should be noted that neither N_γ nor N_{ch} is corrected for efficiency, purity etc. on an event by event basis. For a Poissonian system, $\sigma^2/mean = 1$ for a particular component (*e.g* for N_γ or for N_{ch}). Here the $\sigma^2/mean$ of ratio of N_γ/N_{ch} shows the combination of contributions for each term and their correlation. The event-by-event N_γ/N_{ch} ratio is shown in the Figure 5.1. The ratio being greater than 1 shows $N_\gamma > N_{ch}$ as the N_γ contains background due to non photonic clusters. The $\sigma^2/mean$ of the ratio N_γ/N_{ch} for different centralities is shown in Figure 5.2, which follows the $A + 1/N_{part}$ dependence shown by the dotted lines, where A is constant. Even though $\sigma^2/mean$ represents the fluctuations of the ratio, but it does not remove all fluctuations due to

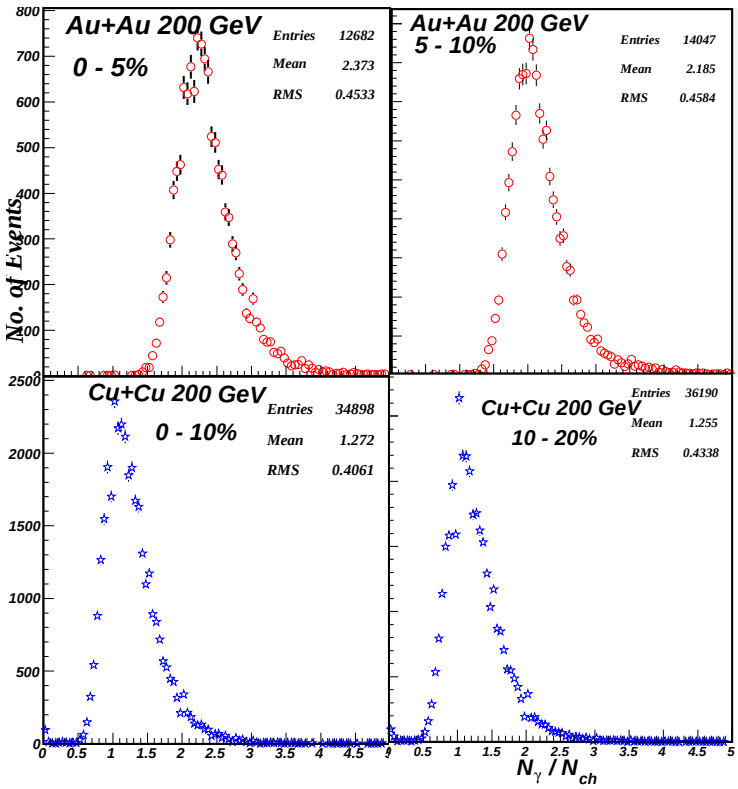

Figure 5.1: *Event-by-event ratio of* N_γ *and* N_{ch} *for Au+Au for* $0-5\%$, $5-10\%$ *and Cu+Cu for* $0-10\%$, $10-20\%$ *centralities respectively.*

other sources (e.g statistical), any physics interpretation therefore needs to take into account.

In order to understand the behavior for randomly generated photons and charged particle, we have generated N_γ and N_{ch} using Poisson distribution taking value $\langle N_\gamma \rangle$ and $\langle N_{ch} \rangle$ from data. σ^2/mean of the ratio are superimposed in data in Fig. 5.3. It is seen that data matches with the simulation reasonably well suggesting the amount of fluctuations present are small.

We have also studied the scaling behavior of the σ^2/mean of the ratio with the number of participating nucleons as a function of centrality. The scaled σ^2/mean of ratio with the number of participating nucleons is almost constant with number of

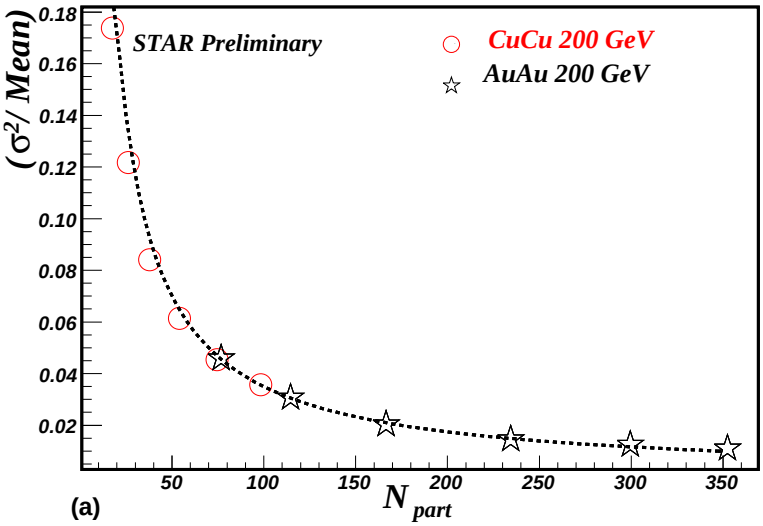

Figure 5.2: *$\sigma^2/mean$ as a function of centrality for Au+Au and Cu+Cu collisions at $\sqrt{s_{NN}}$ = 200 GeV and also fitted with a function $(A + 1/N_{part})$ shown by dotted lines.*

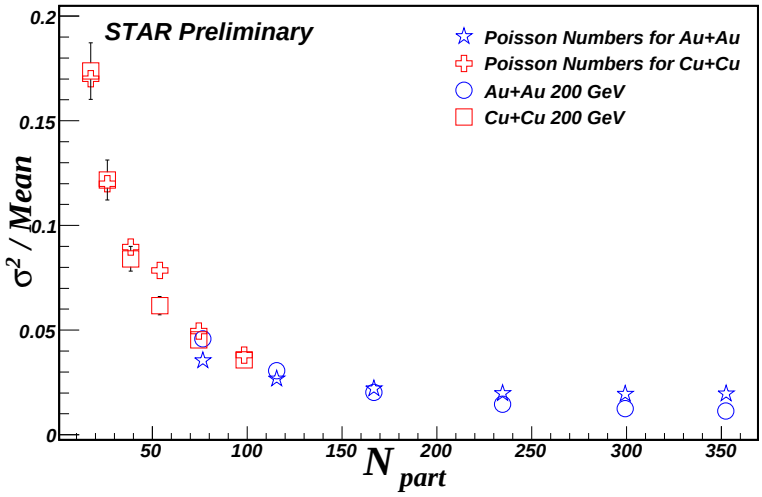

Figure 5.3: *$\sigma^2/mean$ as a function of centrality for Au+Au and Cu+Cu collisions at $\sqrt{s_{NN}}$ = 200 GeV compared with the $\sigma^2/mean$ of the ratio of the photons and charged particles generated according to Poisson distribution*

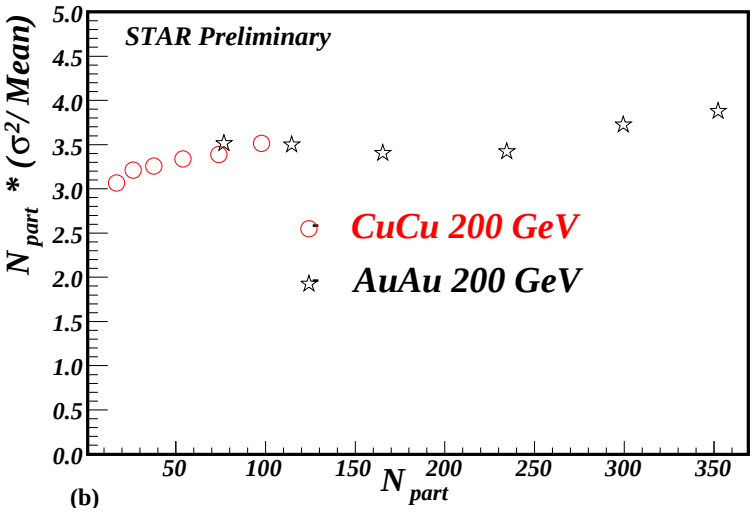

Figure 5.4: *σ^2/Mean scaled by N_{part} as a function of centrality for Au+Au and Cu+Cu collisions at $\sqrt{s_{NN}}$ = 200 GeV. σ^2/Mean shows approximate N_{part} scaling.*

participating nucleons which shows the $1/N_{part}$ scaling as shown in the Figure 5.4. An increase with the N_{part} reflects large particle density and higher correlation between produced particles. However, at larger particle multiplicity the statistical fluctuations also gets reduced.

5.4.5 Results on Photon-Charged Particle Fluctuations by $\nu_{\gamma ch,dyn}$

The $\nu_{\gamma ch,dyn}$ has three terms in equation 5.15, first term is photon fluctuation term, second term is charge fluctuation term and third term is correlated term. Figure 5.5 shows three terms as a function of centrality for $Au + Au$ and $Cu + Cu$ collisions at $\sqrt{s_{NN}} = 200$ GeV. Each individual term i.e, fluctuations in photon and charged terms are larger than the correlated term. Photon term is lower compared to the charged particle term possibly due to the large N_γ compared to N_{ch}, there by lowering the statistical fluctuation in lower centrality bins.

The $\nu_{\gamma ch,dyn}$ is non zero by taking all three terms together and positive showing the

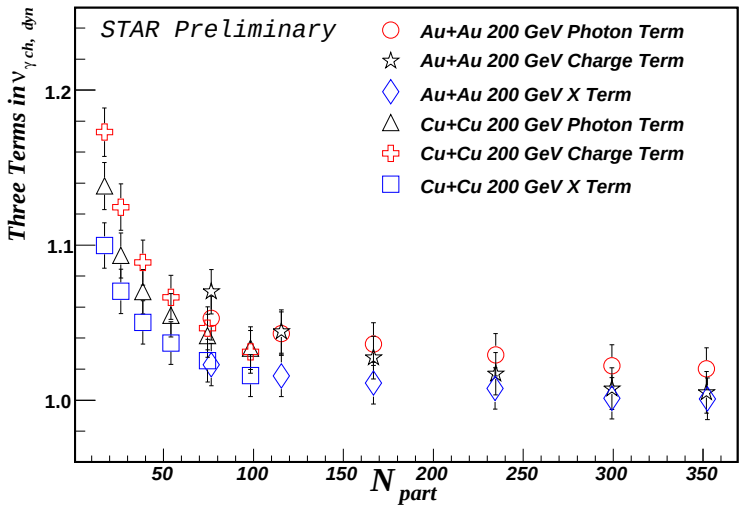

Figure 5.5: *Three terms (i) photon fluctuation term (ii) charged particle fluctuation term and (iii) correlated term as function of centrality for Au+Au and Cu+Cu collisions at* $\sqrt{s_{NN}}$ *= 200 GeV*

individual terms in the $\nu_{\gamma ch,dyn}$ are larger than the correlated term as reported earlier. We also have studied the effect of the variation of efficiency and purity of photon sample on $\nu_{\gamma ch,dyn}$. The threshold to obtain photons sample is chosen such that we have optimum purity of the photon sample. The variation of efficiency and purity of photon sample is studied by varying the threshold on the cluster strength for discrimination of photons from charged particles. Figure 5.6. shows the values of $\nu_{\gamma ch,dyn}$ as a function of centrality in terms N_{part} and with the variation of threshold in terms MIP value. We have studied the $\nu_{\gamma ch,dyn}$ for 3 MIP, 4 MIP, and 6 MIP cut on the threshold on photon sample.

The upstream material due to the Forward Time Projection Chamber ($FTPC$) support structure infront of PMD has $\eta-$dependence. Net material is large in the outer $\eta-$ region. In order to study the effect of this $\eta-$ dependence of material, we have divided the PMD coverage into two $\eta-$bins from $-3.8 \leq \eta \leq -3.2$ and $-3.2 \leq \eta \leq -2.8$. The $\nu_{\gamma ch,dyn}$ values are shown in the Figure 5.7 for both the systems $Au + Au$ and $Cu + Cu$

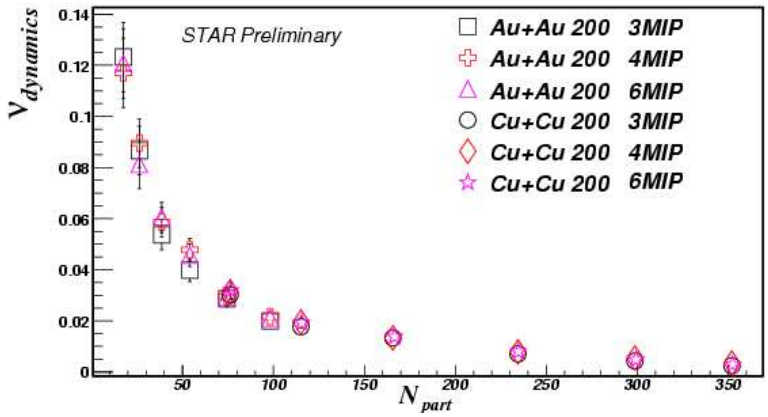

Figure 5.6: *Effect of $\nu_{\gamma ch,dyn}$ of purity of photon sample as function of centrality for Au+Au and Cu+Cu collisions at $\sqrt{s_{NN}}$ = 200 GeV*

studied at 200 GeV collision. Within the errors, the difference in the $\nu_{\gamma ch,dyn}$ measured for different $\eta-$ region is not large.

The general trend of $\nu_{dynamics}$ as shown in Fig. 5.7 is that it decreases with centrality with an approximate $1/N_{part}$ scaling. The $\nu_{\gamma ch,dyn}$ scaled with the number of participating nucleons in $Au+Au$ and $Cu+Cu$ collisions as function of centrality defined interms of number of participating nucleons is shown in the Figure 5.8. Scaled $\nu_{\gamma ch,dyn}$ with N_{part} is almost constant for lower N_{part} i:e for peripheral events and increases as the centrality increases.

5.4.6 p_T Dependence DCC Events

The chiral symmetry is a fundamental (approximate) feature of the strong interaction but it has a firm observational basis only near the normal vacuum. It is therefore of interest to seek experimental information over a wider range of environments. Since high-energy nuclear collisions produce very hot and dense systems, it is natural to investigate whether they can be utilized for this purpose. It has long been speculated that the rapid expansion of the collision zone in heavy ion collisions, after an approximate restoration of

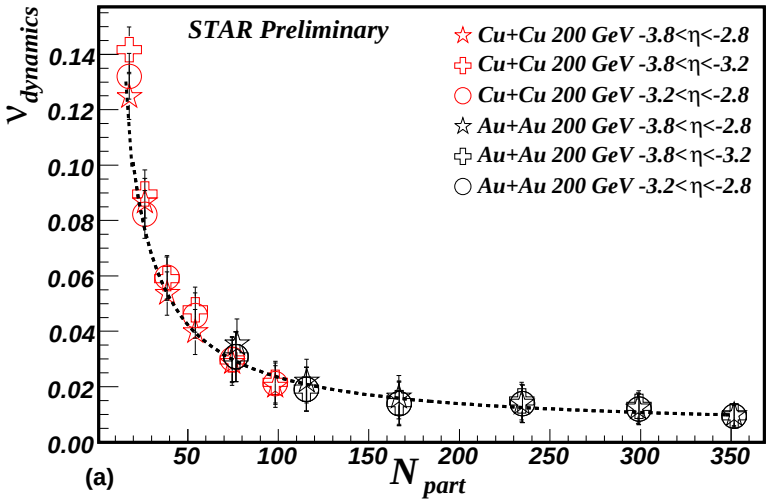

Figure 5.7: *$\nu_{\gamma ch,dyn}$ for two separate η region as a function of centrality for Au+Au and Cu+Cu collisions at $\sqrt{s_{NN}}$ = 200 GeV.*

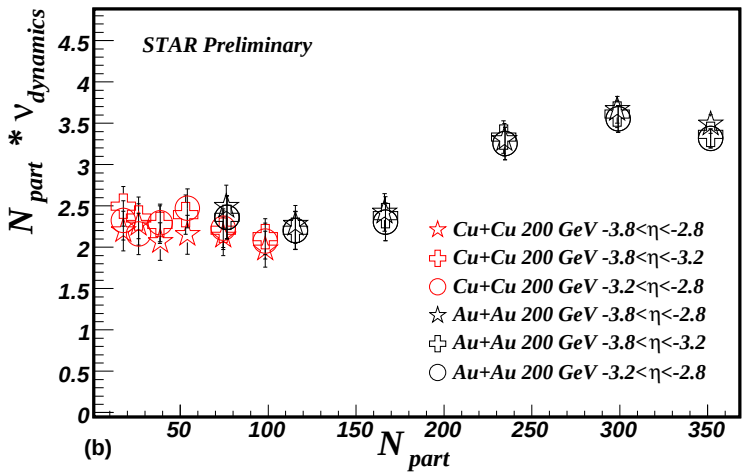

Figure 5.8: *Scaled $\nu_{\gamma ch,dyn}$ with N_{part} for two separate η region as a function of centrality for Au+Au and Cu+Cu collisions at $\sqrt{s_{NN}}$ = 200 GeV.*

chiral symmetry has occurred, may produce long-wavelength isospin-polarized agitations of the pionic field, commonly referred to as Disoriented Chiral Condensates (DCC), which in turn should lead to anomalies in the resulting pion multiplicity distribution [45, 46].

The initial experiments focus for DCC search was on the expected broadening in the distribution of the neutral pion fraction but as it has become increasingly clear that any signal would be carried primarily by the soft pions, this observable is deemed to be impractical (since the decay $\pi^0 \rightarrow \gamma\gamma$ precludes good kinematical information on the neutral pions) using normal calorimeter techniques. It has been studied that due to the softness for particle form DCC the signal should enhance at lower p_T. Earlier studies at WA98 experiment at SPS, it was not possible to study the p_T dependence of this fluctuations with p_T cuts. In [47], authors have shown that the signal for DCC increase with the number of events if we chose the soft photons and charged particles. They have also shown that even if we take low p_T particles for one species (either photon or charged particles), the signal for DCC events should increase. For the first time we have studied the p_T dependence of the $\nu_{\gamma ch,dyn}$ using the two different p_T regions of charged particles from FTPC and are compared with the inclusive sample. Figure 5.9 shows the $\nu_{\gamma ch,dyn}$ with two p_T intervals i.e, from 0.1 to 0.5 GeV/c and 0.5 to 1 GeV/c are compared with the inclusive sample of 0.1 to 3 GeV/c and no approximate p_T dependence has been observed.

The p_T dependence of $\nu_{\gamma ch,dyn}$ scaled with the number of participating nucleons in $Au + Au$ and $Cu + Cu$ collisions as function of centrality is shown in the Figure 5.10. The variation of the scaled $\nu_{\gamma ch,dyn}$ with N_{part} is almost constant for lower N_{part} i.e, for peripheral events and increases as the centrality increase as shown in Fig. 5.10. Observation of almost no p_T dependence in $\nu_{\gamma ch,dyn}$ suggest the presence of appreciably low DCC events, if at all.

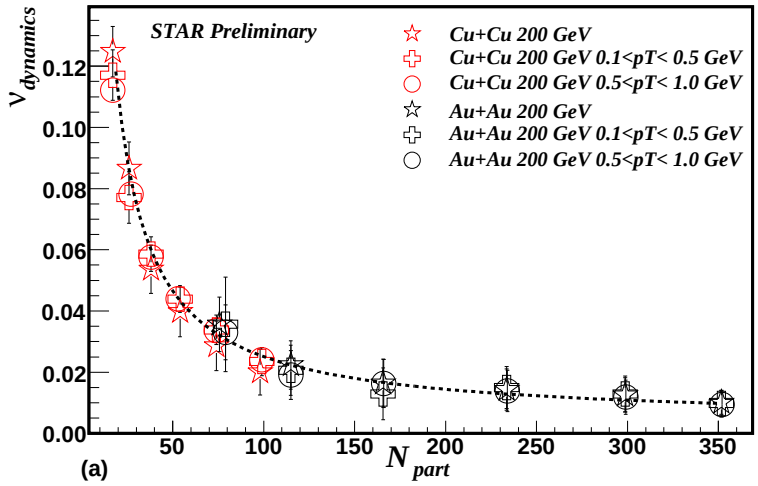

Figure 5.9: $\nu_{\gamma ch,dyn}$ *for two different* p_T *bins compared with the inclusive sample as function of centrality for Au+Au and Cu+Cu collisions at* $\sqrt{s_{NN}}$ *= 200 GeV.*

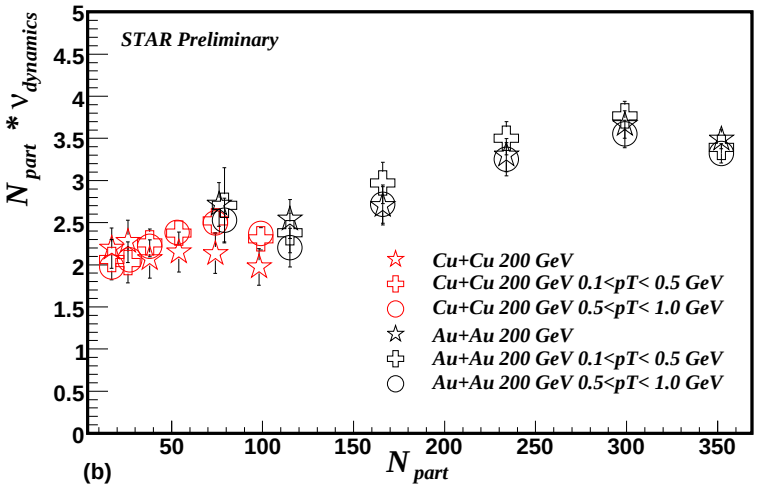

Figure 5.10: Scaled $\nu_{\gamma ch,dyn}$ *with* N_{part} *for two different* p_T *bins compared with the inclusive sample as function of centrality for Au+Au and Cu+Cu collisions at* $\sqrt{s_{NN}}$ *= 200 GeV.*

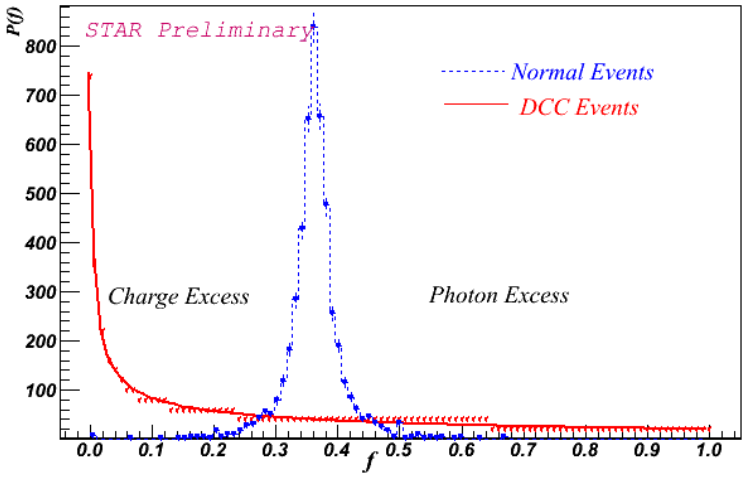

Figure 5.11: *Schematic diagram of the f distribution of DCC events (Red line) and the normal Gaussian distribution of generic events (Blue line) peaking at 1/3. Also shown the regions of photon excess and charge excess.*

5.4.7 Sensitivity of $\nu_{\gamma ch,dyn}$ on DCC : Study with HIJING

To understand the sensitivity of $\nu_{\gamma ch,dyn}$ to the presence of DCC events, a simulation study has been made. HIJING event generator has been used for the simulation of DCC type events at RHIC energy for $Au + Au$ and $Cu + Cu$ collisions. In this work, the charges of the pions are interchanged pairwise ($\pi^+\pi^-\pi^0\pi^0$), in a selected $\eta - \phi$ zone according to the DCC probability distribution as given by equation 5.1 event-by-event. The $\pi^{0\prime}s$ are allowed to decay. For the present study, DCC events have been simulated in a common coverage of PMD and FTPC. The generic events are also generated from HIJING event generator. As emphasized, the distribution for $\pi^{0\prime}s$ in normal events is approximately Gaussian with mean at $\frac{1}{3}$. Figure 5.11 shows the f distribution of pure DCC events and pure generic events using HIJING event generator as simulated in this work

In Fig.5.12, we have presented the $\nu_{\gamma ch,dyn}$ results for $Au+Au$ and $Cu+Cu$ collisions

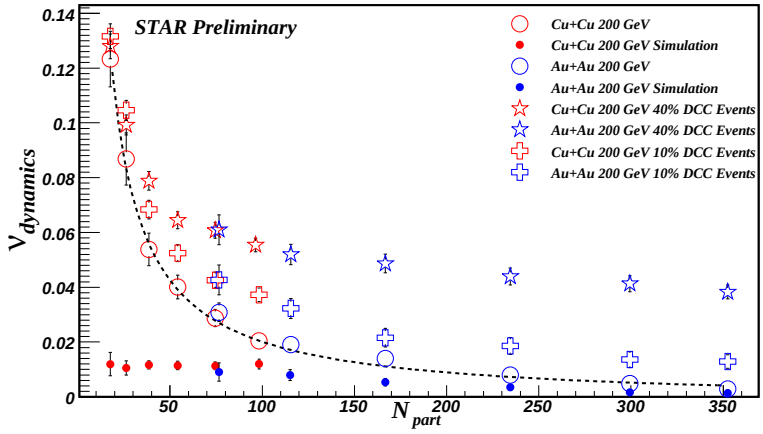

Figure 5.12: *The distribution of $\nu_{\gamma ch,dyn}$ for real data, HIJING events and simulated DCC events with varying DCC fractions.*

having different fractions of $DCC - type$ fluctuation ranging from 10% to 40% and is compared with generic events from HIJING and the real data. The results show a dependence of $\nu_{\gamma ch,dyn}$ with N_{part}. However, these results are very preliminary and further investigations need to be done to put the upper limit on DCC.

Bibliography

[1] H. Appelshauser, et al., NA49 Coll. Phys.Lett.B 459 679 (1999).

[2] S. V. Afanasev, et al., NA49 Coll. hep-ex/0009053.

[3] G. Bayn, Gearald Fridman and Ina Sarecevic, Phys. Lett. B 219, 205(1989).

[4] M. Gazdzicki and S. Mrowczynski, Z Phys. C 54, 127 (1992).

[5] S. Gavin, Nucl. Phys. A 590 163c (1995).

[6] V. Koch, A. Majumder, and J. Randrup nucl-th/0505052.

[7] E. V. Shuryak. Phys. Rev. Lett. 75 1044 (1995).

[8] K. Adcox et al., PHENIX Coll. Phys. Rev. Lett. 89, 082301 (2002).

[9] K. J. Eskola and K. Tuominen Phys. Lett. B 489 329-336 (2000).

[10] J. Bjorken, Phys. Rev. D 27 140 (1983).

[11] K. Adcox, et al., PHENIX Coll. Pyhs. Rev. Lett. 86 3500 (2001).

[12] K. Adcox, et al., PHENIX Coll. Phys. Rev. C 66, 024901 (2002).

[13] J. Adams, et al., STAR Coll. Phys. Rev. C 68 44905 (2003).

[14] C. Adler, et al., STAR Coll. Phys. Lett. B 595 143-150 (2004)

[15] J. Adams, et al., STAR Coll. Phys.Rev. C 71 064906 (2005).

[16] Proceedings of VIII International Symposium on Very High Energy Cosmic Ray Interactions, (Tokyo Japan) 24-30 July, (1994).

[17] J. D. Bjorken, Int. J. Mod. Phys. A7, 4189 (1992).

[18] J. P. Blaizot and A. Krzywcki, Phys. Rev. D 46, 246 (1992).

[19] A. A. Anslem, M. G. Ryskin, Phys. Lett. B 266 482 (1991).

[20] K. Rajagopal and F. Wilczek, Nucl. Phys. B 399, 395 (1993); B404 577 (1993).

[21] J. Bjorken et al., T864 MiniMax Coll. hep-ph/9610379

[22] H. Appelhauser et al., NA49 Coll. Nucl. Phys. A 638 91 (1998).

[23] M. M. Aggarwal et al WA98 Coll. Phys. Rev. C 67 044901 (2003)

[24] Pedro T.P. Viana, Eduardo S. Fraga, Joao R.T. de Mello Neto (Rio de Janeiro Federal U.) Int.J.Mod.Phys.E16:2872-2875,2007. .

[25] C.R.A. Augusto, S.L.C. Barroso, V. Kopenkin, M. Moriya, C.E. Navia, E.H. Shibuya (Niteroi, Fluminense U. Campinas State U., IMECC Moscow State U. Tokyo Inst. Tech.) Phys.Rev.D59:054001,(1999).

[26] G. Arinson et al., UA1 Coll. Phys. Lett. B122 189 (1983)

[27] K. Alpgard et al., UA5 Coll. Phys. Lett. B115 71 (1982).

[28] T. C. Brooks et al., MiniMax Coll. Phys.Rev. D 61 032003 (2000).

[29] T. C. Brooks et al., MiniMax Coll. Phys.Rev. D 55 5667-5680 (1997).

[30] M. M. Aggarwal et al WA98 Coll. Phys.Lett. B420 169-179 (1998).

[31] M. M. Aggarwal et al WA98 Coll. Phys. Rev. C 64 011901(R)(2001).

[32] B. Mohanty1, D. P. Mahapatra1, and T. K. Nayak Phys. Rev. C 66, 044901 (2002).

[33] A.K. Dubey et al., Photon multiplicity detector Technical proposal (For STAR Experiment) VECC/EQG/00-04, (2000).

[34] ALICE Coll. Photon Multiplicity Detector ALICE technical design report, G. Dellacasa et al., CERN/LHCC 99-32, ALICE TDR 6, 30 September (1999).

[35] Nandi, B. K.; Nayak, T. K.; Mohanty, B. et al Physics Letters B 461 142 (1999).

[36] M. M. Aggarwal et al., WA98 Coll. nucl/ex-0108029.

[37] M. M. Aggarwal et al., WA98 Coll. Phys. Lett. B458, 422 (1999).

[38] B. K. Nandi, G. C. Mishra, B. Mohanty, D. P. Mahapatra and T. K. Nayak Phys. Lett. B 449 109 (1999).

[39] M. M. Aggarwal, G. Sood and Y.P. Viyogi Physics Letters B 638 39-43 (2006).

[40] B. Mohanty Int. J. Mod. Phys. A 18 1067 (2003).

[41] S. Mrowczynski, Phys. Lett. B 459 12 (1999).

[42] J. Zrarnek, Phys. Rev. C. 66, 024905 (2002).

[43] C. Pruneau, S. Gavin, and S. Voloshin, Phys. Rev. C 66 044904 (2002).

[44] Nystrand et al., Phys. Rev. C 68, 034902 (2003).

[45] M. Asakawa, H. Minakata and B. Mller Phys. Rev. C 65, 057901 (2002).

[46] Z. Huang, M. Suzuki and X. N. Wang Phys. Rev. D 50:2277 (1994).

[47] B. Mohanty and Julien Serreau Phys. Rept. 414:263-358,(2005).

Chapter 6

Volume Fluctuations

6.1 Introduction

Fluctuations play an important role in phase transitions at extreme conditions of temperture and /*or* density. In the past, event-by-event fluctuations in high energy collisions in small systems (e^+e^-, ep) have been of interest and presently in large systems (heavy ion collisions) have gained significant importance. The past interest centered around dynamical theories which would produce the Negative Binomial (NB) regularities and associated large non-Poissonian fluctuations seen in experimental data. These NB regularities could be interpreted, in terms of fractal behavior and intermittency associated with a possible underlying cascade process. Recently, attention has been drawn towards the importance of fluctuations in the area of heavy ion collisions from the prediction of very large non-Poissonian fluctuations in the neutral pion component coming from a Disoriented Chiral Condensate (DCC) [1]. Attention has also been drawn to the possibility of the charge fluctuations of positive to negative charges and also the charge fluctuations associated with the quark charges (2/3e, 1/3e) present in the QuarkGluon phase [2,3,4,5].

The aim of the analysis presented in this chapter is to estimate the fluctuations due

to the contribution of the impact parameter fluctuations. In the study of fluctuations in high energy heavy ion collisions, measurements are made at different centralities. The peripheral collisions correspond to lower multiplicities whereas in central collisions the multiplicities are high. For a measure of fluctuations involving multiplicities, contributions from number statistics play a dominant role. In general, the fluctuations measured by the width of the distribution at lower multiplicties are higher compared to the ones measured at higher multiplicities because of the fact that in the central collisions the number of nucleon−nucleon scattering and scattering between the produced particles increases, while in the peripheral collisions because of the relatively low number of produced particles the probability of rescattering is low [6]. Various methods are proposed to eliminate the effect of their contribution due to statistical fluctuations, leading to proliferation of measure for statistical fluctuation [7].

Another effect which needs careful study before drawing any definite conclusion on the results of fluctuation is the effect due to the finite width of the centrality bin. The usual practice is to take the average multiplicity in the bin and statistical fluctuation is eliminated based on their mean multiplicity [8]. However, based on the width of the multiplicty bin, the effect of statistical fluctuations varies and net effect might be dominated by lower multiplicities. It is therefore essential to estimate the effect of finite centrality bin width known as "volume fluctuation".

This effect is expected to be more dominant for studying the fluctuations of quantities related to multiplicties, e.g, particle multiplicties(chagred particles and photons), total strangeness, total charm etc. The effect is expected to be reduced for case of studying the ratio or difference of the quantities related to multiplicities e.g, fluctuations of K/π, netcharge fluctuation etc. In this section, we develop a method to investigate and eliminate the effect of volume fluctuation.

6.1.1 Method for Eliminating Volume Fluctuations

The centrality bin is divided into bins of smaller width by dividing the whole range multiplicity (n) for determination of centrality into 2^n equal bins, where n is the step number. $D_i = \sigma^2/mean$ is measured for each smaller bin(i^{th} bin). Final D_i is then calculated as the mean of $D_i's$ in smaller bins.

$$\overline{D} = \frac{\sum_{i=1}^{n} D_i}{n} \tag{6.1}$$

where n is the number of bins in each step.

The variation of $\overline{D}$ is then studied with n and it is expected that for stable value of fluctuation in that centrality bin, D should reach a saturation value. The saturated value is desired fluctuation whose volume fluctuation is eliminated and can then be studied for different centralities.

6.1.2 Model Simulation

Simulation is performed using the random numbers following a Poisson distribution. The distribution in the bin width of multiplicities $N_1, N_2, N_2, ...N_n$ is simulated by the generation of Poissonian distribution of $\mu = N_i$ $(i = 1, 2, ...n)$. The convolution of these distributions gives the result for that particular centrality bin. The simulation based on the generation of a Poissonian random number is applied only for studying fluctuation in multiplicities. For other types of fluctuations e.g hypercharge fluctuations and netcharge fluctuations, we have used events generated with HIJING [9] and simulated the effect. Two correlated Poissonian distribution are generated, where one is used as trigger (e.g. reference multiplicity) and other other one is the observable for which the fluctuations is studied. For the present simulation, the Poissonian distribution is generated using a mean value = 200, which refers to the mean multiplicity of centrality $(0 - 20\%)$ for $Au + Au$ collisions at $\sqrt{s_{NN}}$ =200 GeV. The $\sigma^2/mean$ values are calculated for the

observable for a reference multiplicty bin and the method described in section 6.2.1 is applied to obtain the mean of smaller bins and large bin. Figure 6.1 shows the result for the simulation. The symbol astrick shows $\sigma^2/mean$ for multiplicity distribution obtained for the whole centrality bin and the other symbols represent $\sigma^2/mean$ values for different bins. Ideally for a Poissonian distribution, the $\sigma^2/mean$ value should be 1, which is the red dotted line shown in the Figure 6.1. It is observed that for the whole centrality bin taken together, the value is large, but for smaller bins, the value approaches to 1.

6.1.3 Multiplicity

The first order moment of the multiplicity distribution is defined by the average number of particles of all types or of a particular type. The phase space integral of the corresponding single particle density are interesting at their own and contain information on fluctuations and correlations, which relate to some of the proposed signatures of the plasma. The multiplicity distributions also contain information about the dynamic evolution of the collision and the characterizing hadronic final states and their evolution with increasing energy. We have applied our method to eliminate the volume fluctuations for the multiplicity distribution. Data obtained from HIJING simulation is analyzed for most central collisions i.e the $0-20\%$ centrality bin. In Figure 6.2, $N_{bins} = 1$ corresponds to whole centality bin and higher values of N_{bins} correspond to the values of $D's$ averaged over N_{bins} where N_{bins} is the number of bins in which the width of the centrality bin is divided. It is seen that the values of $D's$ tend to reach a saturation value which can be considered as the fluctaution after elimination of the volume fluctuations.

6.1.4 Netcharge

Theoretical investigations predict a drastic decrease in the event-by-event fluctuations of the net electric charge in local phase space regions in the presence of the QGP phase

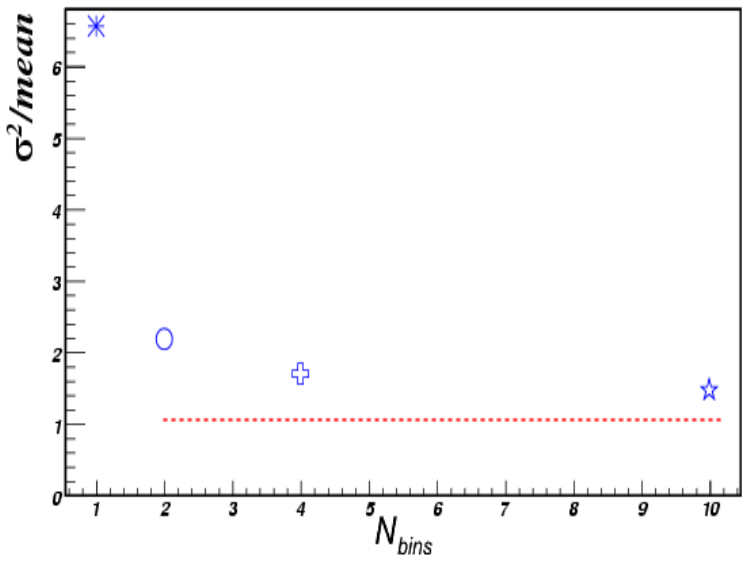

Figure 6.1: *σ^2/mean for central multiplicity bin (shown by astrick), after dividing the central bin into number of bins (shown by other symbols) and for Poissonian system (shown by dotted line).*

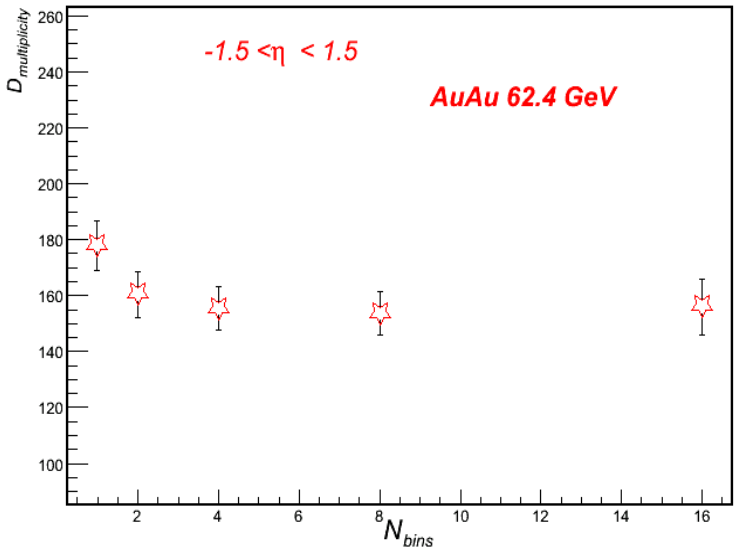

Figure 6.2: *Elimination of volume fluctuations for multiplicity distribution*

[10, 11]. These fluctuations are not related to the transition itself, but rather with the charge distribution in the primordial plasma state. The basic idea is that each of the charge carriers in the plasma carries less charge than the charge carriers in ordinary hadronic matter. The charge will thus be more evenly distributed in a plasma. The main concern of the theoretical discussions is if, how, and why the original charge distribution survives the transition back to ordinary matter [12,13]. Different measures of netcharge fluctuations have been proposed and used in the analysis of experimental data. The most straight forward measures are obtained by looking at the distribution of the net charge given by.

$$Q = N_+ - N_- \tag{6.2}$$

where N_+ is the multiplicity of positive particles within a chosen region and N_- is the corresponding multiplicity of negative particles.

Even though the difference of two multiplicities eliminate volume fluctuations, but we tried to estimate the remaining fluctuations using our method. Figure 6.3 shows the variation of D_Q for different N_{bins}. In case of netcharge as well, the value reduces from large value to a saturated value. This is similar to the observation for the multiplicity.

6.1.5 Hypercharge

The lattice calculations address the issues related to the nature of the transition, the temperature at which it occurs, the properties of the plasma, and the equation of state. The isospin, baryon number, and hypercharge susceptibilities are directly related to event by event fluctuations in heavy ion collisions and are crucial for the interpretation of ongoing heavy-ion experiments [14] and provide valuable information on the degrees of freedom in the hot phase of QCD. The hypercharge fluctuations probe the transitions from hadronic matter to a deconfined QGP. The hypercharge (represented by Y) is the sum of the baryon number (B) and the strangeness (S).

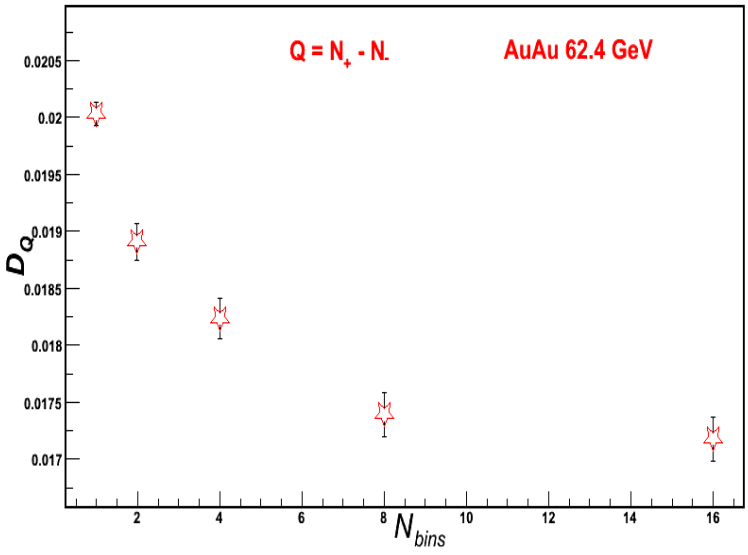

Figure 6.3: *Elimination of volume fluctuations for Net-charge fluctuations.*

$$Y = B + S \tag{6.3}$$

Since in the experiments, efficiency and purity of detector plays a big role in results, so we simulate effect of efficiency and purity on final results in our analysis. We assume efficiency and purity varies as Gaussian with a mean and sigma. These mean and sigma differ for positive and negative particles. Now we have taken the case shown in Table 6.1 and calculated values of $D's$. Figure 6.4 shows the value of $D's$ for different values of n and also the effect of efficiency and purity on the hypercharge values. The hypercharge value reduces from large value to a saturated value as seen in all the cases studied.

S.No.	Set	Mean of Strangeness	Mean for Baryon	Mean of S and B
1	HIJING			
2	First	0.13	0.10	0.1
3	Second	0.13	0.10	0.05
4	Third	0.13	0.10	0.02

Table 6.1: *Table showing the the various values of the mean and sigma of Gaussian for impurity.*

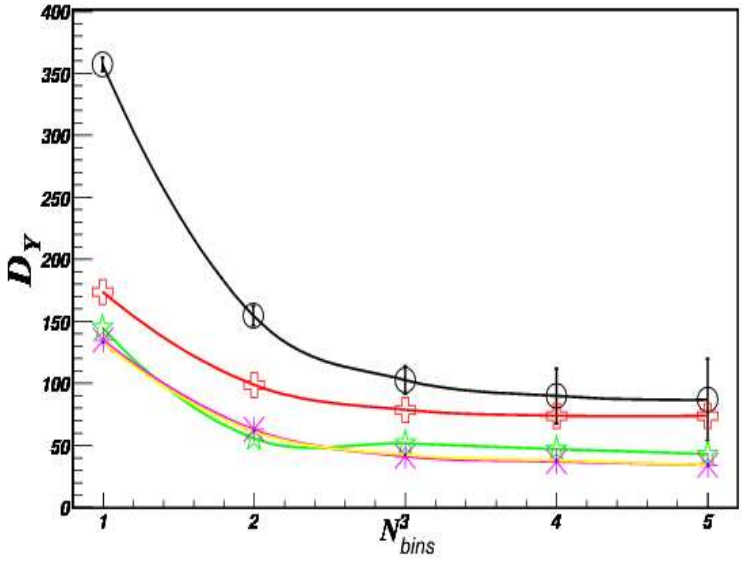

Figure 6.4: *Elimination of volume fluctuations for Hypercharge fluctuations and the effect of the efficiency and purity on hypercharge values.*

Bibliography

[1] K. Rajagopal, F. Wilczek, Nucl. Phys. B 404 (1993) 557.

[2] S. Jeon, V. Koch, Phys. Rev. Lett. 83 (1999) 5435;

[3] S. Jeon, V. Koch, Phys. Rev. Lett. 85 (2000) 2076;

[4] S. Jeon, V. Koch, in: R.C. Hwa, X.-N. Wang (Eds.), QuarkGluon Plasma 3, World Scientific, Singapore, 2004, pp. 430490, hep-ph/0304012.

[5] M. Asakawa, U. Heinz, B. Muller, Phys. Rev. Lett. 85 2072.

[6] R. Stock, Proceedings of Hot Hadronic Matter: Theory and Experiment Divonne France (1994).

[7] Xin-Nian Wang and Miklos Gyulassy Phys. Rev. D 44, 3501 - 3516 (1991)

[8] S. Jeon and V. Koch, Phys. Rev. Lett. 85, 2076 (2000).

[9] M. Asakawa, U. Heinz, and B. Muller, Phys. Rev. Lett. 85, 2072 (2000).

[10] S. Jeon and V. Koch, Phys. Rev. Lett. 85, 2076 (200).

[11] H. Heiselberg and A.D. Jackson, Phys. Rev. C 63, 064904 (2001).

[12] E.V. Shuryak and M.A. Stephanov, Phys. Rev. C 63, 064903 (2001).

[13] K. Loaskowski and R.Wit, Europhys. Lett. 55 (2), 184 (2001).

[14] R. Gavai and S. Gupta Phys. Rev. D 73, 014004 (2006)

Chapter 7

Conclusion and Discussion

Over the last three decades, considerable progress has been made in understanding the mechansim of production of particles in high energy heavy ion collisions. Series of dedicated experiments are performed at AGS, SPS and recently at RHIC. With the time, rarer probes like multistrange hadron, vector mesons are measured. A range of energy from $\sqrt{s_{NN}} = 4$ GeV to 200 GeV has been explored.

All these efforts are motivated by the predictions from Lattice QCD calculations that a deconfined phase transition is likely to occur in high energy heavy ion collisions at very high energy. Based on the energy two distinct scenarios might appear, at very high energy. The baryons will pass each other leaving a baryon free mid rapidity zone resembling with the early universe after a few micro seconds and the other extreme is the case when baryons penetrate each other in a very small volume thereby creating a situation like neutron star.

Both the scenarios should lead to the phase transition from hadronic matter. Considering the similartity of their color-neutral deconfined state of matter with plasma, this state is called the Quark Gluon Plasma (QGP).

The state of of QGP is expected to be in thermal and chemical equilibrium after considerable rescattering. This requires the collision of two heavy nuclei as superposition

of $p-p$ collisions. However for understanding the system created in nucleus-nucleus collision one studies $p-p$ collisions as reference.

Over the years there have been a proliferation of proposed signatures of the formation of QGP. All these signatures are proposed based on the different aspects of the expected system. The collective properties are studied via the measurements of flow, the deconfined state is expected to be revealed by the dissocation of J/ψ and other higher states. The phase transistion is expected to be revealed by sudden change in the fluctuations of one or many variable.

As we have a series of proposed signals, so were the series of results from various experiments at different energies. Unfortunately conflicting explanation of the observed signals make the subject more challenging.

It has therefore become more and more essential to understand the system based on the observables appearing at the different time after the collision. Signals like direct photon, heavy flavor carry the information of the initial conditions, at later stages, production of other hadrons are dominating. It is therfore a challenge to isolate signals which are not affected by the expansions of the system with time and reaching the detectors at the end. All these challenges lead to the design and building of large detector system capable of measureing all possible particles snd study all the details of their production. Putting together the informations gathered by these large experiments with utmost precision gives us a picture which might reveal exclusive signatures of the QGP.

At RHIC, with energy considerable higher compared to earlier experiments at SPS and AGS, new frontiers are opened for particle production and the picture of heavy ion collisions has more probes to reveal. In this thesis one such probe i.e photons at forward rapidity is explored extensively in order to reveal finer details of the system

This work is based on the data taken by several sub-detectors in the STAR experi-

ment, one of the large experiments at RHIC. Two main detectors used in this work are the Forward Time Projection Chamber (FTPC) and the Photon Multiplicity Detector (PMD) for the measurement of charged particles and photons simultaneously at forward rapidity. The bulk of the measurements at RHIC is carried out at the mid rapidity which reveal an almost baryon free region. At forward rapidity, on the other hand baryon density is expected to be higher and the particle production mechanism is expected to be dominated by large density as opposite to large temperature. In this thesis therefore an usually unexplored area has been visited.

The measurement of photons at large rapidity is associated with higher particle density and overlap of showers so, use of conventional calorimeter setup for photon measurements is not possible at forward rapidity. A novel technique is therefore emphasized where 3 radiation length lead converter is used to convert photons to electromagnetic shower particles which are detected by the sensitive medium. High granularity hexagonal gas proportional cells are used as sensitive media. Two planes of sensitive layers are used one for charged particle veto and other placed after the converter used as preshower plane.

The signals obtained from preshower plane are processed to obtain the clusters which could be connected to produced from single incident particle. This procedure needs to deal with overlapping clusters and the clusters split while sharing the signals among more than one cluster. The photon candidates are then selected from this group of clusters after applying proper threshold on the cluster signal and the number of cells forming the cluster. These discrimination thresholds filter photon clusters from likely interacting charged hadronic clusters and split clusters. Final estimation of efficiency and purity in detection of photon samples are obtained from detailed simulation with GEANT with HIJING as an event generator. Average efficiency and purity in $Au + Au$ and $Cu + Cu$ collisions are found to be $\sim 65\%$ and $\sim 70\%$ respectively respectively.

Tracks are reconstructed from FTPC using track following algorithm and have been found to work well upto p_T of 3 GeV. Two detectors, Central Trigger Barrel (CTB) and Zero Degree Calorimeter (ZDC) are used for obtaining the trigger for centrality selection.

In this thesis data obtained with $Au + Au$ collisions and $Cu + Cu$ collisions at $\sqrt{s_{NN}} = 200$ GeV are analyzed. Detailed selection criteria are used for the selection of events, tracks, clusters. For PMD a scheme based on ADC distribution of isolated cells which are comparable to MIP are used for cell to cell gain calibration of the detector. After necessary cleanup and fluctuation signals from different subdetector are tested to be (anti) correlated for further analysis. The photon multiplicities (N_γ obtained from PMD are correlated with reference multiplicity from TPC and the charged particle multiplicities from FTPC. They are found to be anti-correlated for the energy obtained from ZDC.

Results

The approach adopted in this work for systematic understanding of the signal obtained from various detectors is to study in detail the integral and differential variable with varying centrality. These are compared with existing models to understand the mechanism involved. The observables studied are:

1. The photon and charged particle multiplicities, their variation with centrality and scaling properties with number of participating nucleons and number of binary collisions.

2. Pseudorapidity distribution of photons at forward rapidity, their scaling with energy and centrality.

3. The correlation between photon and charged particle multiplicities to investigate the formation of events with large asymmetry in photon to charge particle multiplicities due to the formation of Disoriented Chiral Condensate (DCC). The do-

mains of DCC are expected to be the results of chiral phase transition resulting from high energy heavy ion collisions.

The multiplicity distributions of photons and charged particles at forward rapidity region follow a usual pattern of large number of events at lower multiplicity (peripheral events) with a plateau at the mid central and a fall off at central collisions with tail dominated by fluctuations. The multiplicities of photon and charged particles are well correlated showing similar structure. This characteristic shape of multiplicities is governed mostly by geometry of the collision which could be explained by cross section based on impact parameter of the collision.

In nucleus nucleus collisions, particle production is said to be governed by two main approaches i.e. scaling with N_{part} (number of participating nucleons pairs) and /*or* with N_{bin} (number of binary collisions). Later approach is expected to be dominated at higher incident energy. At RHIC energy, from the data obtained at mid rapidity, efforts are made to explain the multiplicity using two component approach, as multiplicity per participant pair is found to rise with N_{part}. At forward rapidity, however N_{γ} and N_{ch} are found to scale reasonably well with N_{part} thereby suggesting lack of binary component at forward rapidity. The fact that charged particle multiplicity is well correlated with photon multiplicity, we can conclude that most of the photons detected by PMD are the decay products from π^0.

The pseudorapidity distribution of particles can reveal details of production mechanism. The pseudorapidity density can be studied with centrality and scaling with N_{part} or N_{bin} can be studied. The shape and the parameters of the distribution will reveal the distribution of momenta among produced particles. The characteristic shape of flat top at mid rapidity and fall off at higher rapidities are said to be the result of more particle production due to energy transfer at midrapidity.

It is revealed here that forward rapidity region behaves differently. It shows that the

distribution of $\eta - y_{beam}$ shows a limiting behavior, where the particle production does not increase above a certain boundary. This behavior is independent of beam energy and of centrality for photons. For charged particles, due to presence of protons in the sample centrality independence is not strictly maintained. The study of $Au + Au$ and $Cu + Cu$ collisions suggests that limiting fragmentation is independent of colliding systems.

The difference observed in centrality dependence of scaling behavior between photons and charged particles is explained by taking only identified meson e.g. π^0 for photons and π^+, π^- for charged particles. It is seen that excluding baryons and taking mesons only show centrality independent scaling behavior.

A model (HIJING) based on jet and minijet formation is used extensively to explain RHIC data. At midrapidity centrality dependence of rapidity density per participant increase towards central collisions. The general trend of the increase in rapidity density with N_{part} is explained by HIJING to the extent that it rises with centrality but rise in HIJING is faster compared to data. This can be explained by the presence of large hard component in HIJING.

At forward rapidity the centrality dependence of the rapidity density shows different behavior. The rapidity density per participant is nearly constant with centrality. This trend is in difference with the trend at midrapidity and requires different mechanism of particle production at forward rapidity compared to mid rapidity. Possible explanation for such nature are:

– reduction of hard component at forward rapidity

– at higher rapidity effect of gluon saturation might play prominent role and saturation will reduce particle production at higher centrality.

Another topic which has been addressed in this thesis is the study of fluctuation for the ratio of photon to charged particle multiplicities. The topic of fluctuation is an important topic in high energy heavy ion collisions. One of the most prominent

signature of studying fluctuations is expected abrupt change in fluctuation in phase transition. The observed fluctuation is sensitive to the order of phase transition. In fact abrupt change in fluctuation might be the most prominent signal for phase transition in thermalized system.

A change in fluctuation is expected to be observed in N_γ/N_{ch} in case of the formation of domains where chiral phase transition takes place and vacuum orients itself in a particular direction. This phenomena is know as the formation of the domain due to Disoriented Chiral Condensate (DCC). If observed, such domains will provide direct information about the chiral phase transition. In normal collision where no DCC is formed, neutral pion fraction defined by $f = \frac{N_{\pi^0}}{N_\pi}$ peaks at 1/3 with a narrow distribution. In case of DCC domains we expect this distribution to be of the form $1/\sqrt{2}f$.

Several experiments at WA93, WA98 at SPS or MINIMAX at Fermilab have explored the domains of the signal for DCC. It is clear now that very large domains in large number of events are unlikely to happen. Current efforts are therefore centered around in finding the abnormal fluctuation in event-by-event measurements of N_γ/N_{ch}. These studies can be done in localized $\eta - \phi$ space. In studies of fluctuation, various trivial forms of fluctuations i.e., statistical fluctuations, fluctuation due to impact parameter variation (Volume fluctuations) are to be removed. We have described a method to eliminate the volume fluctuation.

We have explored the formation of DCC by measuring the fluctuation associated with N_γ to N_{ch} ratio. We have used two measures to obtain the amount of fluctuations i.e, $\sigma^2/mean$ and $\nu_{dynamics}$. The $\sigma^2/mean$ measures the width of the distribution of ratio and can directly be compared with system generating particle randomly. The study shows that the width ($\sigma^2/mean$) when taken for the ratio of two quantities follows almost Poissonian behavior suggesting the extra fluctuation if present to be very small.

$\nu_{dynamics}$ on the other hand gives us the value of correlation measure of two particles.

The absolute value $\nu_{dynamics}$ should represent how well N_γ and N_{ch} are correlated. Our results shows $\nu_{dynamics}$ to be finite and has approximate $1/N_{part}$ dependence suggesting dilution of correlation for central collisions. A model study based on HIJING where DCC like domains are created shows the existence of DCC domains to be very small. With more detailed study, we can put an upper limit on DCC formation at RHIC.

A List of Publications

- **Forward Lambda production and nuclear stopping power in d + Au collisions at s(NN)**(1/2) = 200-GeV**. B. I. Abelev……**. S.M.Dogra** et. Al. STAR Collaboration **Phys.Rev.C76:064904,2007**.
- **Measurement of transverse single-spin asymmetries for di-jet production in proton-proton collisions at s**(1/2) = 200-GeV.** B. I. Abelev……**. S.M.Dogra** et. Al. STAR Collaboration **Phys.Rev.Lett.99:142003,2007**.
- **Global polarization measurement in Au+Au collisions.** B. I. Abelev……**. S.M.Dogra** et. Al. STAR Collaboration. **Phys.Rev.C76:024915,2007**.
- **Energy dependence of pi+-, p and anti-p transverse momentum spectra for Au+Au collisions at s(NN)**(1/2) = 62.4 and 200-GeV.** B. I. Abelev……**. S.M.Dogra** et. Al. STAR Collaboration. **Phys.Lett.B655:104-113,2007**.
- **Partonic flow and phi-meson production in Au + Au collisions at s(NN)**(1/2) = 200-GeV.** B. I. Abelev……**. S.M.Dogra** et. Al. STAR Collaboration. **Phys.Rev.Lett.99:112301,2007**
- **Mass, quark-number, and sqrt s(NN) dependence of the second and fourth flow harmonics in ultra-relativistic nucleus-nucleus collisions.** B. I. Abelev……**. S.M.Dogra** et. Al. STAR Collaboration. **Phys.Rev.C75:054906,2007**.
- **Rapidity and species dependence of particle production at large transverse momentum for d+Au collisions at s(NN)**(1/2) = 200-GeV.** B. I. Abelev……**. S.M.Dogra** et. Al. STAR Collaboration. **Phys.Rev.C76:054903,2007**
- **Longitudinal double-spin asymmetry and cross section for inclusive jet production in polarized proton collisions at s**(1/2) = 200-GeV.** B. I. Abelev……**. S.M.Dogra** et. Al. STAR Collaboration. **Phys.Rev.Lett.97:252001,2006**.
- **Neutral kaon interferometry in Au+Au collisions at s(NN)**(1/2) = 200-GeV.** B. I. Abelev……**. S.M.Dogra** et. Al. STAR Collaboration. **Phys.Rev.C74:054902,2006**.
- **Strange particle production in p+p collisions at s**(1/2) = 200-GeV.** B. I. Abelev……**. S.M.Dogra** et. Al. STAR Collaboration. **Phys.Rev.C75:064901,2007**.
- **Transverse momentum and centrality dependence of high-p(T) non-photonic electron suppression in Au+Au collisions at s(NN)**(1/2) = 200-GeV.** B. I. Abelev……**. S.M.Dogra** et. Al. STAR Collaboration. **Phys.Rev.Lett.98:192301,2007**.
- **Delta phi Delta eta Correlations in Central Au+Au Collisions at s(NN)**(1/2) = 200-Gev .** J. Adams……**. S.M.Dogra** et. Al. STAR Collaboration. **Phys.Rev.C75:034901,2007**.
- **The Multiplicity dependence of inclusive p(t) spectra from p-p collisions at s**(1/2) = 200-GeV.** J. Adams……**. S.M.Dogra** et. Al. STAR Collaboration. **Phys.Rev.D74:032006,2006**.

- **Scaling Properties of Hyperon Production in Au+Au Collisions at s**(1/2) = 200-GeV.** J. Adams……**. S.M.Dogra** et. Al. STAR Collaboration. **Phys.Rev.Lett.98:062301,2007**.
- **Identified baryon and meson distributions at large transverse momenta from Au+Au collisions at s(NN)**(1/2) = 200-GeV.** J. Adams……**. S.M.Dogra** et. Al. STAR Collaboration. **Phys.Rev.Lett.97:152301,2006**.
- **The Energy dependence of p(t) angular correlations inferred from mean-p(t) fluctuation scale dependence in heavy ion collisions at the SPS and RHIC.** J. Adams……**. S.M.Dogra** et. Al. STAR Collaboration. **J.Phys.G33:451-466,2007**.
- **Strange baryon resonance production in s(NN)**(1/2) = 200-GeV p+p and Au+Au collisions.** J. Adams……**. S.M.Dogra** et. Al. STAR Collaboration. **Phys.Rev.Lett.97:132301,2006**.
- **Direct observation of dijets in central Au+Au collisions at s(NN)**(1/2) = 200-GeV.** J. Adams……**. S.M.Dogra** et. Al. STAR Collaboration. **Phys.Rev.Lett.97:132301,2006**. **Phys.Rev.Lett.97:162301,2006.**
- **Forward neutral pion production in p+p and d+Au collisions at s(NN)**(1/2) = 200-GeV.** J. Adams……**. S.M.Dogra** et. Al. STAR Collaboration. **Phys.Rev.Lett.97:152302,2006**.
- **Identified hadron spectra at large transverse momentum in p+p and d+Au collisions at s(NN)**(1/2) = 200-GeV.** J. Adams……**. S.M.Dogra** et. Al. STAR Collaboration. **Phys.Lett.B637:161-169,2006**.
- **Strangelet search at RHIC.** B. I. Abelev……**. S.M.Dogra** et. Al. STAR Collaboration. **Phys.Rev.C76:011901,2007**.
- **Multiplicity and pseudorapidity distributions of charged particles and photons at forward pseudorapidity in Au + Au collisions at s(NN)**(1/2) = 62.4-GeV.** J. Adams……**. S.M.Dogra** et. Al. STAR Collaboration. **Phys.Rev.C73:034906,2006**.
- **Proton - lambda correlations in central Au+Au collisions at S(NN)**(1/2) = 200-GeV.** J. Adams……**. S.M.Dogra** et. Al. STAR Collaboration. **Phys.Rev.C74:064906,2006**.
- **Directed flow in Au+Au collisions at s(NN)**(1/2) = 62-GeV.** J. Adams……**. S.M.Dogra** et. Al. STAR Collaboration. **Phys.Rev.C73:034903,2006**.
- **Transverse-momentum p(t) correlations on (eta, phi) from mean-p(t) fluctuations in Au-Au collisions at s(NN)**1/2 = 200-GeV.** J. Adams……**. S.M.Dogra** et. Al. STAR Collaboration. **J.Phys.G32:L37-L48,2006**.
- **Incident energy dependence of pt correlations at RHIC.** J. Adams……**. S.M.Dogra** et. Al. STAR Collaboration. **Phys.Rev.C72:044902,2005**.
- **Multi-strange baryon elliptic flow in Au + Au collisions at s(NN)**(1/2) = 200-GeV.** J. Adams……**. S.M.Dogra** et. Al. STAR Collaboration. **Phys.Rev.Lett.95:122301,2005**.
- **Multiplicity and pseudorapidity distributions of photons in Au + Au collisions at s(NN)**(1/2) = 62.4 GeV.** J. Adams……**. S.M.Dogra** et. Al. STAR Collaboration. **Phys.Rev.Lett.95:062301,2005**.

- **K(892)* resonance production in Au+Au and p+p collisions at s(NN)**(1/2) = 200-GeV at STAR.** J. Adams……**. S.M.Dogra** et. Al. STAR Collaboration. **Phys.Rev.C71:064902,2005**.
- **Pion interferometry in Au+Au collisions at S(NN)**(1/2) = 200 GeV.** J. Adams……**. S.M.Dogra** et. Al. STAR Collaboration. **Phys.Rev.C71:044906,2005**.
- **Minijet deformation and charge-independent angular correlations on momentum subspace (eta, phi) in Au-Au collisions at s(NN)**(1/2) = 130 GeV.** J. Adams……**. S.M.Dogra** et. Al. STAR Collaboration. **Phys.Rev.C73:064907,2006**.
- **Pseudorapidity asymmetry and centrality dependence of charged hadron spectra in d + Au collisions at S(NN)**(1/2) = 200-GeV.** J. Adams……**. S.M.Dogra** et. Al. STAR Collaboration. **Phys.Rev.C70:064907,2004**.
- **Pion, kaon, proton and anti-proton transverse momentum distributions from p + p and d + Au collisions at s(NN)**1/2 = 200-GeV.** J. Adams……**. S.M.Dogra** et. Al. STAR Collaboration. **Phys.Lett.B616:8-16,2005**.

Publications in Conferences and Symposia:

- **Energy and system size dependence of photon production at forward rapidities at RHIC.** Monika Sharma (Panjab U.), **Sunil Dogra,** Neeraj Gupta (Jammu U.) **Int. J. Mod. Phys. E16 :1845-1851, (2007)**.
- **Photon and Charge correlations and fluctuations at forward rapidity in STAR experiment. S. M. Dogra** *for* STAR Collaboration**. J. Phys. G: Nucl. Part. Phys. 35, 104094 (2008) .**